

# A Fokker-Planck Acceleration Technique For Multiphysics Problems with Highly Forward-Peaked Scattering

Dissertation

Presented in Partial Fulfillment of the Requirements for the Degree Doctor  
of Philosophy in the Graduate School of The Ohio State University

By

John Joseph Kuczek, B.S. Physics/Astrophysics

Graduate Program in Nuclear Engineering

The Ohio State University

2021

Dissertation Committee:

Richard Vasques, Advisor

Tunc Aldemir

Barry Ganapol

John Horack

© Copyright by  
John Joseph Kuczek  
2021

## **Abstract**

This work characterizes a new acceleration technique for multiphysics problems with highly forward-peaked scattering. The Fokker-Planck equation, which is an asymptotic limit of the transport equation in highly forward-peaked settings, is modified and used to accelerate the transport equation in a high-order/low-order acceleration scheme. The modified Fokker-Planck equation preserves the angular flux and flux moments of the transport equation and can be coupled to multiphysics solves. Coupling the modified Fokker-Planck equation with multiphysics isolates expensive transport sweeps. We observe up to two times speed up in wall-clock time when using this new technique compared to multiphysics coupling using the standard Fokker-Planck Synthetic Acceleration technique.

*This work is dedicated to my parents and siblings who have always believed in me and were  
there for me when I needed it most.*

## **Acknowledgments**

I would like to thank my family for having unending love and support for me throughout my graduate program. I would like to thank all of my friends that helped me live life outside of classes and my thesis project. I give thanks to the following long list of names of friends (in no particular order) that will probably never read this: Andrew, Courtney, Adam, Chris, Drew, Kevin, Dan, Steffen, Matt, Bryce, Rachel, Logan, Marc, Drexler, and Emily. In the first year of my graduate program, I got a puppy named Azula. Little did I know she would become such an anchor in my life. She has helped me mature in so many ways and I look forward to the future adventures we'll share together.

I would like to thank my advisor, Dr. Richard Vasques, for his continued guidance and support over the years. He has helped shape me into the researcher and person I am today. I would also like to thank the members of my committee, Dr. Tunc Aldemir, Dr. John Horack, and Dr. Barry Ganapol, for their input and support, and I wish to thank Dr. Andre Palmer, the Graduate Faculty Representative, for his assistance. Additionally, I would like to acknowledge the help and guidance of Dr. Japan Patel.

I acknowledge support under award number NRC-HQ-84-15-G-0024 from the Nuclear Regulatory Commission. I also acknowledge funding support from the NRC graduate student fellowship program. The statements, findings, conclusions, and recommendations are those of the authors and do not necessarily reflect the view of the U.S. Nuclear Regulatory Commission.

## **Vita**

December 2016 ..... B.S. in Physics and Astrophysics, The  
Ohio State University  
August 2017 to present ..... Graduate Research Associate,  
The Ohio State University

## **Publications**

### **Research Publications**

J. J. Kuczek, J. K. Patel, R. Vasques, "Modified Fokker-Planck Acceleration for Forward-Peaked Transport Problems in Slab Geometry", Journal of Computational and Theoretical Transport, DOI: 10.1080/23324309.2021.1894174

J. K. Patel, J. J. Kuczek, R. Vasques, "One-Way Coupled Tumor Response Model for Combined-Hyperthermia-Radiotherapy Treatment with Anisotropic Scattering", ANS Winter Meeting and Expo, 2019

R. B. Adams et al. , "The Pulsed Fission-Fusion (PuFF) Engine: Development Status", AIAA ASCEND, 2020

E. Colvin et al. , "Optimization of Plutonium-238 Production in the Advanced Test Reactor for Radioisotope Thermoelectric Generators in Deep Space Exploration Applications", Nuclear and Emerging Technologies for Space, 2019

## **Fields of Study**

Major Field: Nuclear Engineering

## Table of Contents

	Page
Abstract . . . . .	ii
Dedication . . . . .	iii
Acknowledgments . . . . .	iv
Vita . . . . .	v
List of Tables . . . . .	ix
List of Figures . . . . .	xi
List of Symbols . . . . .	xiv
1. Introduction . . . . .	1
1.1 Background and Motivation . . . . .	1
1.2 Dissertation Layout . . . . .	6
2. The Transport Equation . . . . .	8
2.1 Deriving the Transport Equation . . . . .	8
2.1.1 Variables . . . . .	9
2.1.2 Definitions . . . . .	11
2.1.3 Derivation . . . . .	14
2.2 Mono-Energetic Transport in Slab Geometry . . . . .	16
2.3 Mono-Energetic, Steady State Transport in Slab Geometry . . . . .	18

3.	Solving the Transport Equation . . . . .	19
3.1	Approximations to the Transport Equation . . . . .	19
3.1.1	The Diffusion Approximation . . . . .	20
3.1.2	The Fokker-Planck Approximation . . . . .	23
3.1.3	The Discrete Ordinates Approximation . . . . .	26
3.2	Linear Solver Methods . . . . .	27
3.2.1	Source Iteration . . . . .	28
3.2.2	Synthetic Acceleration . . . . .	29
3.2.3	Preconditioning . . . . .	30
3.3	Nonlinear Solver Methods . . . . .	31
3.3.1	Picard Iteration . . . . .	32
3.3.2	Newton's Method . . . . .	33
4.	A New Fokker-Planck Acceleration Technique . . . . .	35
4.1	Fokker-Planck Synthetic Acceleration . . . . .	35
4.2	Modified Fokker-Planck Acceleration . . . . .	37
4.2.1	MFPA using a Linear Consistency Term . . . . .	37
4.2.2	MFPA using Nonlinear Consistency Terms . . . . .	41
4.3	Equivalency between MFPA and FPSA . . . . .	43
5.	Discretization . . . . .	45
5.1	Fokker-Planck Operator . . . . .	45
5.2	Finite Element Method . . . . .	46
6.	Numerical and Experimental Validation . . . . .	51
6.1	Scattering Kernels . . . . .	52
6.1.1	Screened Rutherford Kernel . . . . .	52
6.1.2	Exponential Kernel . . . . .	53
6.1.3	Henyey-Greenstein Kernel . . . . .	54
6.2	Convergence Criterion . . . . .	55
6.3	Choice of Consistency Term . . . . .	56
6.4	Angularly Discrete Fourier Analysis . . . . .	60
6.4.1	Theory . . . . .	60
6.4.2	Spectral Radii Evaluations . . . . .	63
6.5	Homogeneous Slab Results . . . . .	64
6.5.1	Problem Set 1 . . . . .	64
6.5.2	Problem Set 2 . . . . .	72
6.6	Heterogeneous Slab Results . . . . .	79



6.6.1	Problem Set 1 . . . . .	79
6.6.2	Problem Set 2 . . . . .	80
7.	Radiative Transfer Multiphysics Test Problem . . . . .	87
7.1	Coupling Transport . . . . .	87
7.2	Coupling FPSA . . . . .	90
7.3	Coupling MFPA . . . . .	92
7.4	Radiative Transfer Results . . . . .	95
7.4.1	Exponential Kernel . . . . .	96
7.4.2	Henye-Greenstein Kernel . . . . .	101
7.4.3	Screened Rutherford Kernel . . . . .	107
8.	Discussion of Future Work . . . . .	113

## List of Tables

Table	Page
6.1 Problem Parameters . . . . .	51
6.2 SRK cross-section Moments . . . . .	53
6.3 EK cross-section Moments . . . . .	54
6.4 HGK cross-section Moments . . . . .	55
6.5 Runtime and Iteration Counts for Problem 1 with SRK using MFPA with Different Consistency Terms . . . . .	58
6.6 Runtime and Iteration Counts for Problem 2 with SRK using MFPA with Different Consistency Terms . . . . .	58
6.7 Theoretical Spectral Radius Results for MFPA . . . . .	63
6.8 Runtime and Iteration Counts for Problem 1 with SRK . . . . .	66
6.9 Runtime and Iteration Counts for GMRES Problem 1 with SRK . . . . .	67
6.10 Runtime and Iteration Counts for Problem 1 with EK . . . . .	68
6.11 Runtime and Iteration Counts for GMRES Problem 1 with EK . . . . .	69
6.12 Runtime and Iteration Counts for Problem 1 with HGK . . . . .	71
6.13 Runtime and Iteration Counts for GMRES Problem 1 with HGK . . . . .	72
6.14 Runtime and Iteration Counts for Problem 2 with SRK . . . . .	73

6.15	Runtime and Iteration Counts for GMRES Problem 2 with SRK . . . . .	74
6.16	Runtime and Iteration Counts for Problem 2 with EK . . . . .	75
6.17	Runtime and Iteration Counts for GMRES Problem 2 with EK . . . . .	76
6.18	Runtime and Iteration Counts for Problem 2 with HGK . . . . .	78
6.19	Runtime and Iteration Counts for GMRES Problem 2 with HGK . . . . .	78
7.1	Exponential cross-section Moments for $\Delta = 10^{-7}$ . . . . .	98
7.2	Runtime, Transport and Thermal Sweeps for Radiative Transfer Problem using non accelerated transport, FPSA coupling, and MFPA coupling with EK	101
7.3	Error(Eq. (7.10)) between angular flux moments found from MFPA coupling versus FPSA coupling using EK . . . . .	101
7.4	Henyey-Greenstein cross-section Moments for $g = 0.99$ . . . . .	104
7.5	Runtime, Transport and Thermal Sweeps for Radiative Transfer Problem using non accelerated transport, FPSA coupling, and MFPA coupling with HGK . . . . .	107
7.6	Error(Eq. (7.10)) between angular flux moments found from MFPA coupling versus FPSA coupling using HGK . . . . .	107
7.7	Runtime, Transport and Thermal Sweeps for Radiative Transfer Problem using non accelerated transport, FPSA coupling, and MFPA coupling with SRK . . . . .	112
7.8	Error(Eq. (7.10)) between angular flux moments found from MFPA coupling versus FPSA coupling using SRK . . . . .	112

## List of Figures

Figure	Page
1.1 Solvers for Linear and Nonlinear Systems of Equations . . . . .	4
2.1 The Spatial ( $\mathbf{x}$ ), Direction-of-Flight ( $\mathbf{\Omega}$ ), and Energy ( $E$ ) Variables [51] . . .	9
2.2 The Polar Angle $\theta$ and Azimuthal Angle $\omega$ [51] . . . . .	10
2.3 $dVd\Omega dE$ about $(\mathbf{x}, \mathbf{\Omega}, E)$ [51] . . . . .	12
4.1 MFPA algorithm . . . . .	37
4.2 MFPA algorithm . . . . .	40
5.1 Spatial dependence of angular flux for $\mu > 0$ . The flux at a cell interface is defined by the solution from the previous cell. . . . .	48
5.2 Spatial dependence of angular flux for $\mu < 0$ . Similar to Fig. 5.1, the flux at a cell interface is defined by the solution from the previous cell. . . . .	48
6.1 Problem 1 Results for SRK with $\eta = 10^{-7}$ using Different Consistency Terms	57
6.2 Problem 2 Results for SRK with $\eta = 10^{-7}$ using MFPA with Different Consistency Terms . . . . .	59
6.3 Results of $\rho_{th}$ for SRK, EK, and HGK . . . . .	64
6.4 Problem 1 Results for SRK with $\eta = 10^{-7}$ . . . . .	65
6.5 Problem 1 Results for EK with $\Delta = 10^{-7}$ . . . . .	68
6.6 Problem 1 Results for HGK with $g = 0.99$ . . . . .	70

6.7	Problem 2 Results for SRK with $\eta = 10^{-7}$ . . . . .	73
6.8	Problem 2 Results for EK with $\Delta = 10^{-7}$ . . . . .	75
6.9	Problem 2 Results for HGK with $g = 0.99$ . . . . .	77
6.10	Results for Heterogeneous Problem 1 using SRK with $\varepsilon = \pm 0.4, \pm 0.8$ . . .	81
6.11	Results for Heterogeneous Problem 1 using EK with $\varepsilon = \pm 0.4, \pm 0.8$ . . .	82
6.12	Results for Heterogeneous Problem 1 using HGK with $\varepsilon = \pm 0.4, \pm 0.8$ . .	83
6.13	Results for Heterogeneous Problem 2 using SRK with $\varepsilon = \pm 0.4, \pm 0.8$ . . .	84
6.14	Results for Heterogeneous Problem 2 using EK with $\varepsilon = \pm 0.4, \pm 0.8$ . . .	85
6.15	Results for Heterogeneous Problem 2 using HGK with $\varepsilon = \pm 0.4, \pm 0.8$ . .	86
7.1	Transport-Thermal Coupling Algorithm . . . . .	89
7.2	FPSA-Thermal Coupling Algorithm . . . . .	91
7.3	MFPA-Thermal Coupling Algorithm . . . . .	94
7.4	Radiative results for $N = 16$ and $L = 15$ using EK with $\Delta = 10^{-7}$ . . . . .	97
7.5	Radiative results for $N = 32$ and $L = 31$ using EK with $\Delta = 10^{-7}$ . . . . .	99
7.6	Radiative results for $N = 64$ and $L = 63$ using EK with $\Delta = 10^{-7}$ . . . . .	100
7.7	Radiative results for $N = 16$ and $L = 15$ using HGK with $g = 0.99$ . . . . .	103
7.8	Radiative results for $N = 32$ and $L = 31$ using HGK with $g = 0.99$ . . . . .	105
7.9	Radiative results for $N = 64$ and $L = 63$ using HGK with $g = 0.99$ . . . . .	106
7.10	Radiative results for $N = 16$ and $L = 15$ using SRK with $\eta = 10^{-5}$ . . . . .	109
7.11	Radiative results for $N = 16$ and $L = 15$ using SRK with $\eta = 10^{-6}$ . . . . .	110

7.12	Radiative results for $N = 16$ and $L = 15$ using SRK with $\eta = 10^{-7}$	. . . . . 111
------	---	---------------

## List of Symbols

$\mathbf{x}$	Position Vector
$\boldsymbol{\Omega}$	Direction of Flight
$E$	Kinetic Energy
$t$	Time
$\mathbf{i}, \mathbf{j}, \mathbf{k}$	Orthogonal Unit Vectors
$x, y, z$	Cartesian Coordinate Axes
$\theta$	Polar Angle
$\omega$	Azimuthal Angle
$\mu$	Cosine of Polar Angle
$v$	Nonrelativistic Speed
$m$	Mass
$\mathcal{N}$	Particle Density Distribution
$\psi$	Angular Flux
$\phi$	Scalar Flux
$\Sigma_t$	Macroscopic Total Cross-Section
$\Sigma_a$	Macroscopic Absorption Cross-Section
$\Sigma_s$	Macroscopic Scattering Cross-Section
$Q$	Source
$\bar{\mu}_0$	Mean Scattering Cosine Angle

$\Sigma_{s,l}$ .....	Scattering Cross-Section Moments
$1...n...N$ .....	Distinct Angles
$w_n$ .....	Quadrature Weights
$\ell$ .....	Iteration Index
$\eta$ .....	Screening Parameter
$\Delta$ .....	Exponential Parameter
$g$ .....	Anisotropy Factor
$\Phi$ .....	Radiation Angular Intensity
$h$ .....	Planck's Constant
$\nu$ .....	Frequency
$c$ .....	Speed of Light in Vacuum
$k$ .....	Stefan-Boltzmann Constant
$T$ .....	Material Temperature
$a$ .....	Radiation Constant



# **Chapter 1: Introduction**

This chapter motivates the solution of highly forward-peaked scattering transport problems using conventional methods and presents a new method that improves upon previous methods. The history of forward-peaked, high scattering transport is also discussed. Lastly, an outline is given for the remainder of the dissertation.

## **1.1 Background and Motivation**

Forward-peaked, high scattering problems are difficult to solve numerically for a number of reasons. Solutions to the linear Boltzmann equation converge slowly when using conventional methods such as source iteration (SI) [1] and the generalized minimal residual method (GMRES) [2]. For high scattering problems, the iteration matrix has a spectral radius close to one, leading to slow convergence [1].

Diffusion-based acceleration, such as diffusion synthetic acceleration (DSA) [3, 4], has shown large improvement on convergence rates for high scattering problems. DSA gained popularity after conception and became a very well researched technique. DSA was found to be a special case of generalized rebalance [5]. For highly anisotropic scattering problems, it was shown that DSA will have degraded performance [6], and could be remedied by accelerating the flux and current using the solution of the low-order diffusion calculation. The original DSA [3] was extended to a four-step procedure and applied to non-diamond

differencing schemes in planar geometry [7, 8]. It was further reduced to a simpler version of the four-step DSA that provided quick convergence for discontinuous finite elements spatial discretizations [9].

Diffusion acceleration coupling techniques have been developed to accelerate transport in multiphysics models. The DSA-multigrid method was developed to solve problems in electron transport more efficiently [10]. To speed up the convergence of radiative transfer in clouds, a quasi-diffusion method has been developed [11]. An effective DSA scheme for radiative diffusion calculations was developed using a one-group operator as the preconditioner for a multigroup problem [12].

The Coarse Mesh Finite Difference (CMFD) method was also developed to accelerate diffusion problems [13]. CMFD speeds up convergence through the preservation of the net current [1, 14]. CMFD is a simple and efficient method that has been used to accelerate the convergence of transient neutron transport calculations [15–17].

Nonlinear diffusion acceleration (NDA) was developed as an alternative to DSA. NDA has been used to accelerate convergence of the multi-group transport equation [18, 19]. NDA allows for coarser mesh solves leading to faster convergence [20, 21]. Another advantage NDA offers is the variety of coupling strategies that can be used for acceleration schemes and multiphysics solves [22]. NDA has been used to further accelerate convergence for transport criticality problems using Picard iteration and Newton’s method [23]. NDA has been used in Monte Carlo multiphysics problems that have thermal hydraulic coupling leading to improved performance [24, 25]

DSA, CMFD, and NDA all accelerate up to the first moment of angular flux. This leads to inefficiency when tackling forward-peaked problems, as the higher order moments carry important information about the angular flux. Techniques have been developed that

accelerate the linear Boltzmann equation using higher order moments. For instance, work has been done on  $P_L$  acceleration using modified scattering cross section moments to accelerate convergence of anisotropic transport problems [26]. The Simplified  $P_N$  ( $SP_N$ ) equations have been applied to anisotropic high scattering problems and has shown promising results when using an angular multigrid preconditioner [27].

One of the most recent convergence methods developed is Fokker-Planck Synthetic Acceleration (FPSA) [28, 29]. FPSA utilizes the Fokker-Planck approximation to accelerate the linear Boltzmann equation. FPSA accelerates up to  $N$  moments of the angular flux and has shown significant improvement in the convergence rate for the types of problems described above. The method returns a speed-up of several orders of magnitude with respect to wall-clock time when compared to DSA [28].

In solving most realistic transport problems, the angular flux is often coupled with other relevant physics, leading to sophisticated multiphysics models. Multiphysics problems couple different physics together for a numerical solve. General coupling techniques can be separated into two categories: linear coupling and nonlinear coupling. Linear coupling typically involves direct inversion or source iteration. Nonlinear coupling is often employed in nonlinear solves [30]. The two main types of nonlinear coupling are referred to as loose and tight coupling [30]. Picard iteration is commonly used to solve loosely coupled nonlinear equations. Newton's method is a popular choice when solving tightly coupled nonlinear equations. There are many different strategies for coupling transport into a multiphysics problem [31, 32]. Figure 1.1 depicts a diagram of some of the popular solvers that are used to solve linear and nonlinear systems of equations.

There are a wide variety of areas that require solutions to angular flux including astrophysics, medical physics, and plasma physics. In medical physics, radiotherapy is one of the

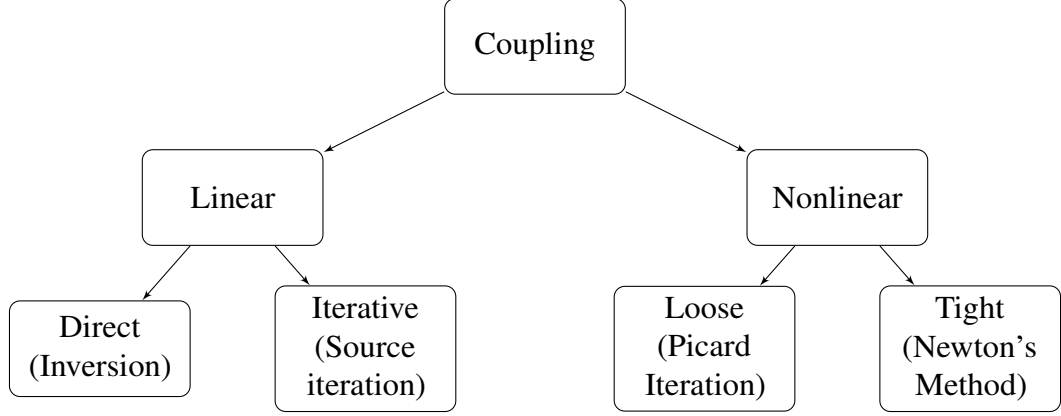


Figure 1.1: Solvers for Linear and Nonlinear Systems of Equations

most widely used treatment methods to care for cancer. Multiphysics based models are used to predict the response of tumors while undergoing treatment. When modeling radiotherapy, the dose profile is dependent upon the angular flux [33, 34]. Radiotherapy problems are typically forward-peaked and highly scattering. Understanding neutral particle transport in plasmas is an important problem that has received a lot of attention in recent years [35–37]. The transport of neutral particles in the edge and divertor regions of fusion experiments is of great interest and is predominantly modeled using Monte Carlo methods. Determining radiative transport in the atmosphere is a core objective in atmosphere modeling. The distribution of heat in Earth’s atmosphere is determined through the processes of solar radiation being absorbed and reflected as well as radiation leaving Earth out into space [38, 39]. This type of radiation heat exchange is heavily reliant on anisotropic radiation scattering [11, 40].

Strategies to solve forward-peaked, highly scattering multiphysics problems often revolve around limiting the number of transport sweeps done, as solving the linear Boltzmann equation is typically the most expensive part of the solve. When coupling transport schemes

that use an approximation, it is common practice to couple the approximation to the multiphysics problem in order to isolate the transport solve [31]. In this setup, the linear Boltzmann equation is referred to as the high-order(HO) equation and the approximation is referred to as the low-order(LO) equation. Synthetic acceleration schemes (like DSA and FPSA) are unable to couple the approximation in the multiphysics solve because the approximation is used to correct the error in each transport sweep and is not a separate equation. NDA is able to couple the LO equation in a multiphysics problem and isolate transport sweeps.

The purpose of this work is to introduce a new approach that employs the strategy of NDA and uses the Fokker-Planck approximation, called here *Modified Fokker-Planck Acceleration* (MFPA). This method employs a high-order/low-order (HOLO) scheme in which the high-order equation is the linear Boltzmann equation and the low-order equation is a modified Fokker-Planck (FP) equation. The modified FP equation contains a consistency term that preserves the moments of angular flux given by the transport equation. The preservation of moments in the modified FP equation is particularly appealing for applications to multiphysics problems [30, 33], in which the coupling between transport and the other physics can be done through the (LO) FP equation. In this document, we use a choice of a *linear* consistency term to facilitate verification of the approach, as the results obtained with this choice should be equivalent to those obtained through FPSA. In general, the definition of the consistency term is not unique, and MFPA has also been developed with a variety of nonlinear consistency terms whose results have been analyzed in this document. A target application for MFPA is radiative transfer in clouds, where photons undergo highly forward-peaked scattering. MFPA has been applied to a multiphysics problem coupled with radiative transfer [31, 41] using different coupling techniques.

## 1.2 Dissertation Layout

Chapter 2 will introduce and derive the linear Boltzmann equation in its entirety. The definitions of the energy, angular, and spatial variables are mentioned and briefly explained. The full equation will be reduced to mono-energetic, steady state transport in slab geometry.

Chapter 3 will review common approximations to the transport equation as well as acceleration methods that have been used for speeding up the solution to neutral particle transport problems. Approximations to the transport equation include the diffusion approximation, the Fokker-Planck approximation, and the discrete ordinates approximation. All will be derived and discussed in detail. Linear and nonlinear solvers are used to solve the transport equation and approximations. There are a plethora of linear and nonlinear solver methods [30]. A few of the most prevalent solver methods will be discussed.

Chapter 4 will begin with discussion of Fokker-Planck Synthetic Acceleration. This leads into introduction of the new acceleration technique called Modified Fokker-Planck Acceleration. MFPA can be formulated using linear and nonlinear consistency terms. A variety of consistency terms will be introduced and discussed. The linear version of MFPA is equivalent to FPSA and a derivation and discussion will be given.

Chapter 5 will discuss spatial and angular discretization schemes used in this document. The discrete ordinates approximation using Gauss-Legendre quadrature is used to discretize equations in angle. A moment preserving discretization is used to discretize the Fokker-Planck operator. The discretization of the Fokker-Planck operator has a significant impact on the performance of Fokker-Planck based acceleration [29]. The finite element method is used for spatial discretization.

Chapter 6 will cover numerical validation of MFPA through Fourier analysis and experimentation. We introduce the scattering kernels that generate scattering moments sets used in

experiments. The convergence criterion used for all experiments is described. Angularly discrete Fourier analysis applied to MFPA using a linear consistency term will be discussed in detail. Fourier analysis is used to determine the theoretical spectral radius of the MFPA iteration matrix. The numerical spectral radius of MFPA is also determined through numerical experimentation. We then present experiments that were tested using MFPA along with DSA, FPSA, and non-accelerated transport. The motivation of this chapter is validate the MFPA approach through comparison of results with established methods. Results using MFPA with a linear consistency term and nonlinear consistency terms are presented. Homogeneous and heterogeneous slab problems are introduced to test the stability and performance of MFPA.

Chapter 7 will introduce a radiative transfer multiphysics test problem. The results for this problem are used to examine the performance of multiphysics coupling with MFPA versus coupling with FPSA. Results will be given for MFPA, FPSA, and non-accelerated transport.

Chapter 8 contains a discussion on the overall results found in the document. Ongoing research and other potential application for related future research are mentioned. Future work and further development of MFPA will be discussed.

## **Chapter 2: The Transport Equation**

The transport equation was first derived over one hundred years ago by Ludwig Boltzmann in order to mathematically describe the behavior of gases in a medium [42]. Further development of the transport equation has led to applications in a wide variety of areas including neutral and charged particle transport [4, 6, 9, 18, 24, 33, 35, 41, 43–50]. In this chapter we first derive the linear Boltzmann equation in its integro-differential form. We then reduce this equation to the case of mono-energetic transport in slab geometry.

### **2.1 Deriving the Transport Equation**

Neutral particle transport represents the process of neutrally charged particles, such as photons and neutrons, propagating through a physical system. Particles can undergo collisions with a medium in which they scatter or are absorbed. In this section we will define the mathematical equations that describe neutral particle transport. We begin by defining the independent variables of the system. We then establish the necessary physics and the relevant unknowns. We finish with deriving the equation to find these unknowns. The concepts discussed in this section have been described in greater detail elsewhere [43–45, 51].



### 2.1.1 Variables

The general three-dimensional transport process depends on seven independent variables: three components of the position vector  $\mathbf{x}$ , two angles to specify the unit vector  $\mathbf{\Omega}$  denoting the direction of flight, the kinetic energy  $E$ , and time  $t$ . Figure 2.1 depicts the position and direction-of-flight vectors.

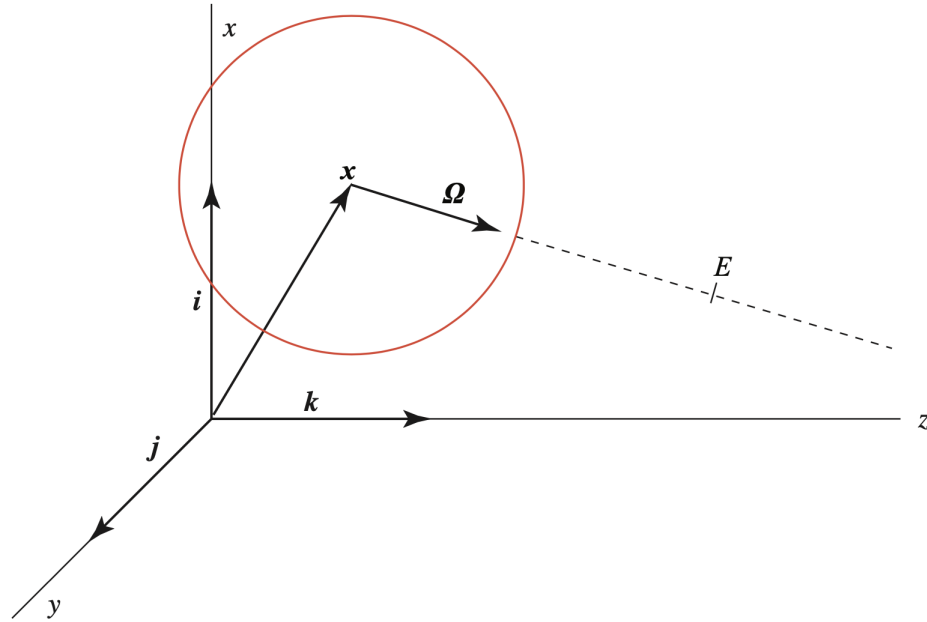


Figure 2.1: The Spatial ( $\mathbf{x}$ ), Direction-of-Flight ( $\mathbf{\Omega}$ ), and Energy ( $E$ ) Variables [51]

We use conventional Cartesian coordinates to define  $\mathbf{x}$ :

$$\mathbf{x} = x\mathbf{i} + y\mathbf{j} + z\mathbf{k}, \quad (2.1)$$

where  $\mathbf{i}$ ,  $\mathbf{j}$ , and  $\mathbf{k}$  are orthogonal unit vectors. The direction-of-flight vector is a unit vector that is specified using a polar angle  $\theta$ , defined relative to the  $z$ -axis, and an azimuthal angle

$\omega$ , defined relative to the  $x$ -axis. The cosine of the polar angle is defined as  $\mu = \cos \theta$ . The direction cosines are projected onto the three Cartesian axes in Fig. 2.2.

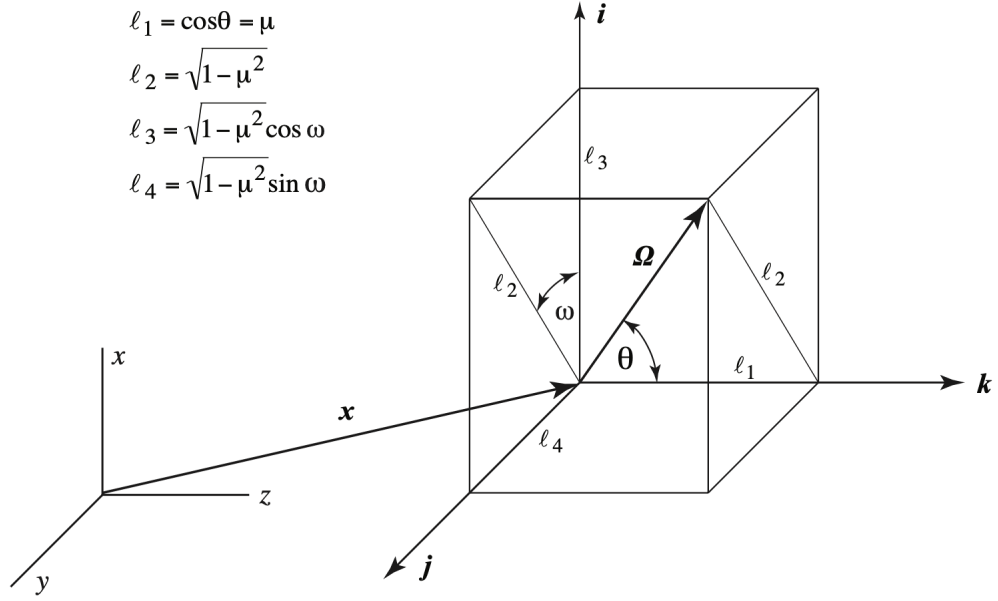


Figure 2.2: The Polar Angle  $\theta$  and Azimuthal Angle  $\omega$  [51]

We express the direction-of-flight vector  $\Omega$  as

$$\Omega = \Omega_x i + \Omega_y j + \Omega_z k, \quad (2.2)$$

where

$$\Omega_x = \ell_3 = \sqrt{1 - \mu^2} \cos \omega, \quad (2.3a)$$

$$\Omega_y = \ell_4 = \sqrt{1 - \mu^2} \sin \omega, \quad (2.3b)$$

$$\Omega_z = \ell_1 = \mu. \quad (2.3c)$$

If we displace the spatial variables  $x$ ,  $y$ , and  $z$  by incremental amounts  $dx$ ,  $dy$ , and  $dz$ , the spatial vector  $x$  sweeps out an incremental volume  $dV = dx dy dz$ . Similarly, if we displace

the angular variables  $\mu$  and  $\omega$  by incremental amounts  $d\mu$  and  $d\omega$ , then the incremental solid angle  $d\Omega$  is described by:

$$d\Omega = \sin \theta d\theta d\omega = d\mu d\omega. \quad (2.4)$$

A minus sign was omitted from Eq. (2.4), since  $\mu$  runs from 1 to -1 when  $\pi$  runs from 0 to 1.

We denote  $\mathbf{v}$  as the particle's velocity vector and  $\mathbf{\Omega} = \frac{\mathbf{v}}{|\mathbf{v}|}$ . The components of the particle's velocity in Cartesian coordinates are

$$\dot{x} = v\Omega_x, \quad (2.5a)$$

$$\dot{y} = v\Omega_y, \quad (2.5b)$$

$$\dot{z} = v\Omega_z, \quad (2.5c)$$

where  $v$  is the particle's nonrelativistic speed,  $v = \sqrt{\frac{2E}{m}}$ , and  $m$  is the mass of the particle.

### 2.1.2 Definitions

We now define the physical quantities needed to denote the particle population. We consider the phase space in Fig. 2.3, where all particles that are located in a volume increment  $dV$  about a point  $\mathbf{x}$  at time  $t$ , travel within a solid angle  $d\Omega$  about the direction  $\mathbf{\Omega}$ , and have energies between  $E$  and  $E + dE$ . The angular particle density  $\mathcal{N}(\mathbf{x}, \mathbf{\Omega}, E, t)$  is a density distribution of (generally) six independent variables and the time variable, defined by:

$$\mathcal{N}(\mathbf{x}, \mathbf{\Omega}, E, t) dV d\Omega dE = \text{the expected number of particles in } dV d\Omega dE \text{ about } (\mathbf{x}, \mathbf{\Omega}, E) \text{ at time } t. \quad (2.6)$$

The angular flux (or fluence rate)  $\psi(\mathbf{x}, \mathbf{\Omega}, E, t)$  is generally defined as [43, 44]:

$$\psi(\mathbf{x}, \mathbf{\Omega}, E, t) = v\mathcal{N}(\mathbf{x}, \mathbf{\Omega}, E, t), \quad (2.7)$$

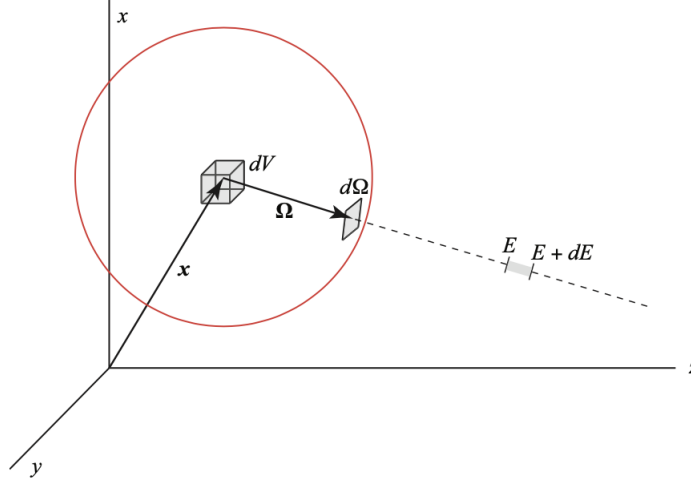


Figure 2.3:  $dVd\Omega dE$  about  $(\mathbf{x}, \boldsymbol{\Omega}, E)$  [51]

and describes the rate at which particles flow across surfaces. Integrating Eq. (2.7) over  $\boldsymbol{\Omega}$  gives the scalar flux:

$$\phi(\mathbf{x}, E, t) = \int_{4\pi} d\Omega \psi(\mathbf{x}, \boldsymbol{\Omega}, E, t). \quad (2.8)$$

Particles typically interact with the medium that they are traveling through. Generally, they interact with matter through two processes: absorption and scattering. When a particle undergoes absorption, it is absorbed by the medium and has left the system through this process. If the particles scatters with the medium, the particle likely has a new energy and direction of travel. As a particle travels an incremental distance  $ds$ , it can be assumed that the probability of interaction is proportional to  $ds$ , independent of the past history of the particle. The proportionality constant between the probability of interaction and the distance  $ds$  is known as the macroscopic total cross-section  $\Sigma_t$ . In general both the macroscopic absorption cross-section ( $\Sigma_a$ ) and the macroscopic scattering cross-section ( $\Sigma_s$ ) depend only

on energy, space, and time. We define the probability of absorption as

$$\Sigma_a(\mathbf{x}, E, t) ds = \text{probability that a particle traveling an incremental distance } ds \text{ will be absorbed,} \quad (2.9)$$

and the probability of scattering as

$$\Sigma_s(\mathbf{x}, E, t) ds = \text{probability that a particle traveling an incremental distance } ds \text{ will scatter.} \quad (2.10)$$

Particles can change their direction  $\mathbf{\Omega}$  and energy  $E$  to a new direction  $\mathbf{\Omega}'$  and energy  $E'$  after scattering. We define the macroscopic differential scattering cross-section  $\Sigma_s(\mathbf{x}, \mathbf{\Omega} \rightarrow \mathbf{\Omega}', E \rightarrow E', t)$ , such that the probability that a particle traveling a distance  $ds$  will scatter from  $E$  to  $dE'$  at  $E'$  and from  $\mathbf{\Omega}$  to  $d\mathbf{\Omega}'$  at  $\mathbf{\Omega}'$  is

$$\Sigma_s(\mathbf{x}, \mathbf{\Omega} \rightarrow \mathbf{\Omega}', E \rightarrow E', t) dE' d\mathbf{\Omega}' ds. \quad (2.11)$$

If the probability that a particle will scatter from direction  $\mathbf{\Omega}$  to direction  $\mathbf{\Omega}'$  depends only on the scattering angle (the angle between  $\mathbf{\Omega}$  and  $\mathbf{\Omega}'$ ), the scattering process is rotationally invariant. This indicates that scattering is in media with randomly distributed scattering centers. For this case, we define the cosine of the scattering angle using dot product notation:

$$\Sigma_s(\mathbf{x}, \mathbf{\Omega} \cdot \mathbf{\Omega}', E \rightarrow E', t) dE' d\mathbf{\Omega}' ds = \Sigma_s(\mathbf{x}, \mu, \mu', E \rightarrow E', t) dE' d\mathbf{\Omega}' ds, \quad (2.12)$$

where  $\mu, \mu' = \mathbf{\Omega} \cdot \mathbf{\Omega}'$ . Integrating Eq. (2.12) over all energies and angles gives the macroscopic scattering cross-section at energy  $E$

$$\Sigma_s(\mathbf{x}, E, t) = \int_0^\infty dE' \int_{4\pi} d\mathbf{\Omega}' \Sigma_s(\mathbf{x}, \mathbf{\Omega} \cdot \mathbf{\Omega}', E \rightarrow E', t). \quad (2.13)$$

Lastly, the macroscopic total cross-section is

$$\Sigma_t(\mathbf{x}, E, t) = \Sigma_a(\mathbf{x}, E, t) + \Sigma_s(\mathbf{x}, E, t), \quad (2.14)$$

and the probability that a particle traveling a distance  $ds$  will undergo any interaction is given by

$$\Sigma_t(\mathbf{x}, \mathbf{\Omega} \rightarrow \mathbf{\Omega}', E \rightarrow E', t) dE' d\mathbf{\Omega}' ds. \quad (2.15)$$

### 2.1.3 Derivation

The transport equation can be defined by the relationship between the loss and gain of particles in any given volume of a phase space. Following [45], let us consider a six-dimensional volume fixed in space with dimensions  $\Delta x, \Delta y, \Delta z, \Delta E, \Delta \mu, \Delta \omega$ . The number density in this volume at time  $t$  can be expressed using Eq. (2.6) as  $\mathcal{N}(\mathbf{x}, \mathbf{\Omega}, E, t) \Delta \alpha$ , where  $\Delta \alpha = \Delta x \Delta y \Delta z \Delta E \Delta \mu \Delta \omega$ . The number of particles in this volume changes with time. We write

$$\text{Rate of Change} = \Delta \alpha \frac{\partial}{\partial t} \mathcal{N}(\mathbf{x}, \mathbf{\Omega}, E, t). \quad (2.16)$$

The particle density changes through the gain or loss of five different mechanisms: the net rate of particles that leave the system; absorption; scattering out of  $\Delta \alpha$ , also known as outscattering; inscattering (where particles are gained when particles at a different  $E$  or  $\mathbf{\Omega}$  scatter into  $\Delta \alpha$ ); and production of particles by an internal or external source.

Particles can stream out of the volume through any dimension of the surface area. Consider the surfaces of the cube perpendicular to the  $x$ -axis. The net rate of particles leaving through the cube at these surfaces is defined by

$$(\text{Streaming})_x = \dot{x} \mathcal{N}(\mathbf{x}, \mathbf{\Omega}, E, t) \big|_x^{x+\Delta x} \Delta y \Delta z \Delta E \Delta \mu \Delta \omega. \quad (2.17)$$

where  $\dot{x}$  is defined by Eq. (2.5a) and  $\Delta y \Delta z \Delta E \Delta \mu \Delta \omega$  is the surface area. Letting  $\Delta x$  go to the differential  $dx$ , we get

$$(\text{Streaming})_x = \Delta x \frac{\partial}{\partial x} (\dot{x} \mathcal{N}(\mathbf{x}, \mathbf{\Omega}, E, t)) \Delta y \Delta z \Delta E \Delta \mu \Delta \omega. \quad (2.18)$$

The same procedure can be applied to all other components of flow through the cube, resulting in

$$\text{Streaming} = \left( \frac{\partial}{\partial x} \dot{x} + \frac{\partial}{\partial y} \dot{y} + \frac{\partial}{\partial z} \dot{z} + \frac{\partial}{\partial E} \dot{E} + \frac{\partial}{\partial \mu} \dot{\mu} + \frac{\partial}{\partial \omega} \dot{\omega} \right) \mathcal{N}(\mathbf{x}, \mathbf{\Omega}, E, t) \Delta \alpha. \quad (2.19)$$

Furthermore, neutral particles stream with no change in energy ( $\dot{E} = 0$ ) and travel in straight lines between collisions ( $\dot{\mu} = \dot{\omega} = 0$ ). Charged particles would undergo stopping power, where charged particles such as alpha or beta particles lose energy due to their interaction with matter. Applying these conditions to Eq. (2.19) and using the definitions from Eqs. (2.5) results in

$$\begin{aligned}\text{Streaming} &= \left( \frac{\partial}{\partial x} \dot{x} + \frac{\partial}{\partial y} \dot{y} + \frac{\partial}{\partial z} \dot{z} \right) \mathcal{N}(\mathbf{x}, \mathbf{\Omega}, E, t) \Delta\alpha \\ &= v \mathbf{\Omega} \cdot \nabla \mathcal{N}(\mathbf{x}, \mathbf{\Omega}, E, t) \Delta\alpha.\end{aligned}\tag{2.20}$$

The rate of absorption is described by:

$$\text{Absorption} = v \Sigma_a(\mathbf{x}, E, t) \mathcal{N}(\mathbf{x}, \mathbf{\Omega}, E, t) \Delta\alpha.\tag{2.21}$$

Similarly, the rate of inscattering and outscattering can be written as

$$\text{Inscattering} = \Delta\alpha \int_0^\infty dE' \int_{4\pi} d\Omega' v' \Sigma_s(\mathbf{x}, \mathbf{\Omega}' \cdot \mathbf{\Omega}, E' \rightarrow E, t) \mathcal{N}(\mathbf{x}, \mathbf{\Omega}', E', t),\tag{2.22}$$

and

$$\text{Outscattering} = \Delta\alpha \int_0^\infty dE' \int_{4\pi} d\Omega' v \Sigma_s(\mathbf{x}, \mathbf{\Omega} \cdot \mathbf{\Omega}', E \rightarrow E', t) \mathcal{N}(\mathbf{x}, \mathbf{\Omega}, E, t).\tag{2.23}$$

The distribution function in Eq. (2.23) does not depend on the integration variables allowing us to simplify Eq. (2.23) to

$$\text{Outscattering} = v \Sigma_s(\mathbf{x}, E, t) \mathcal{N}(\mathbf{x}, \mathbf{\Omega}, E, t) \Delta\alpha.\tag{2.24}$$

Lastly, we represent the internal and external source of particles by introducing the function  $Q(\mathbf{x}, \mathbf{\Omega}, E, t)$ , such that the rate of particles produced in the volume is

$$\text{Source} = Q(\mathbf{x}, \mathbf{\Omega}, E, t) \Delta\alpha.\tag{2.25}$$

Combining Eqs. (2.20) to (2.22), (2.24) and (2.25) allows us to build an equation that describes rate of change given by Eq. (2.16). Letting  $\Delta\alpha$  approach zero results in

$$\begin{aligned}
\frac{\partial \mathcal{N}(\mathbf{x}, \mathbf{\Omega}, E, t)}{\partial t} = & Q(\mathbf{x}, \mathbf{\Omega}, E, t) \\
& + \int_0^\infty dE' \int_{4\pi} d\Omega' v' \Sigma_s(\mathbf{x}, \mathbf{\Omega}' \cdot \mathbf{\Omega}, E' \rightarrow E, t) \mathcal{N}(\mathbf{x}, \mathbf{\Omega}', E', t) \\
& - v \mathbf{\Omega} \cdot \nabla \mathcal{N}(\mathbf{x}, \mathbf{\Omega}, E, t) \\
& - v \Sigma_s(\mathbf{x}, E, t) \mathcal{N}(\mathbf{x}, \mathbf{\Omega}, E, t) \\
& - v \Sigma_a(\mathbf{x}, E, t) \mathcal{N}(\mathbf{x}, \mathbf{\Omega}, E, t).
\end{aligned} \tag{2.26}$$

Finally, using the relationships from Eq. (2.7) and Eq. (2.14) allows us to write the transport equation

$$\begin{aligned}
\frac{1}{v} \frac{\partial \psi(\mathbf{x}, \mathbf{\Omega}, E, t)}{\partial t} + \mathbf{\Omega} \cdot \nabla \psi(\mathbf{x}, \mathbf{\Omega}, E, t) + \Sigma_t(\mathbf{x}, E, t) \psi(\mathbf{x}, \mathbf{\Omega}, E, t) \\
= \int_0^\infty dE' \int_{4\pi} d\Omega' \Sigma_s(\mathbf{x}, \mathbf{\Omega}' \cdot \mathbf{\Omega}, E' \rightarrow E, t) \psi(\mathbf{x}, \mathbf{\Omega}', E', t) + Q(\mathbf{x}, \mathbf{\Omega}, E, t).
\end{aligned} \tag{2.27}$$

Spatial and initial boundary conditions are required to solve Eq. (2.27). The angular flux of particles at all points on the surface of the system is given by

$$\psi(\mathbf{x}_b, \mathbf{\Omega}, E, t) = \psi_b(\mathbf{x}_b, \mathbf{\Omega}, E, t), \quad \mathbf{n} \cdot \mathbf{\Omega} < 0, \tag{2.28}$$

where  $\psi_b$  is the specified angular flux at the boundary,  $\mathbf{x}_b$  is the point at the surface, and  $\mathbf{n}$  is the outward normal unit vector at point  $\mathbf{x}_b$ . The initial angular flux is given by

$$\psi(\mathbf{x}, \mathbf{\Omega}, E, 0) = \psi_i(\mathbf{x}, \mathbf{\Omega}, E) \tag{2.29}$$

where  $\psi_i$  is the specified initial angular flux.

## 2.2 Mono-Energetic Transport in Slab Geometry

Under certain conditions, a simpler version of Eq. (2.27) can be defined to model mono-energetic transport in slab geometry. In this section we derive the linear Boltzmann equation under the conditions of mono-energetic transport in a homogeneous medium.



Assuming that the particles in the system are mono-energetic, Eq. (2.27) becomes

$$\begin{aligned} \frac{1}{v} \frac{\partial \psi(\mathbf{x}, \mathbf{\Omega}, t)}{\partial t} + \mathbf{\Omega} \cdot \nabla \psi(\mathbf{x}, \mathbf{\Omega}, t) + \Sigma_t(t) \psi(\mathbf{x}, \mathbf{\Omega}, t) \\ = \int_{4\pi} d\Omega' \Sigma_s(\mathbf{\Omega}' \cdot \mathbf{\Omega}, t) \psi(\mathbf{x}, \mathbf{\Omega}', t) + Q(\mathbf{x}, \mathbf{\Omega}, t), \end{aligned} \quad (2.30)$$

and the spatial boundary conditions reduce to

$$\psi(\mathbf{x}_b, \mathbf{\Omega}, t) = \psi_b(\mathbf{x}_b, \mathbf{\Omega}, t), \quad \mathbf{n} \cdot \mathbf{\Omega} < 0. \quad (2.31)$$

In 1-D slab geometry, it is assumed that the system is infinite in the  $x$ - and  $y$ - directions and finite in the  $z$ - direction; and the cross-sections, source, and boundary fluxes are independent of  $x$  and  $y$ . In other words, the system is azimuthally symmetric (or rotationally invariant) about  $z$ . The angular flux is then only dependent on  $z$ ,  $\mu$ , and  $\omega$ ; and is independent of  $x$  and  $y$ :

$$\psi(\mathbf{x}, \mathbf{\Omega}, t) = \bar{\psi}(z, \mathbf{\Omega}, t) = \bar{\psi}(z, \mu, \omega, t). \quad (2.32)$$

Equation (2.30) reduces to

$$\begin{aligned} \frac{1}{v} \frac{\partial \bar{\psi}(z, \mathbf{\Omega}, t)}{\partial t} + \mu \frac{\partial \bar{\psi}(z, \mathbf{\Omega}, t)}{\partial z} + \Sigma_t \bar{\psi}(z, \mathbf{\Omega}, t) \\ = \int_{4\pi} d\Omega' \Sigma_s(\mathbf{\Omega}' \cdot \mathbf{\Omega}) \bar{\psi}(z, \mathbf{\Omega}', t) + Q(z, \mathbf{\Omega}, t). \end{aligned} \quad (2.33)$$

Using the relationship from Eq. (2.32), we rewrite Eq. (2.33) as

$$\begin{aligned} \frac{1}{v} \frac{\partial \bar{\psi}(z, \mu, \omega, t)}{\partial t} + \mu \frac{\partial \bar{\psi}(z, \mu, \omega, t)}{\partial z} + \Sigma_t \bar{\psi}(z, \mu, \omega, t) \\ = \int_{-1}^1 d\mu' \int_0^{2\pi} d\omega \Sigma_s(\mu, \mu', \omega) \bar{\psi}(z, \mu', \omega, t) + Q(z, \mu, \omega, t), \end{aligned} \quad (2.34)$$

We can eliminate the azimuthal angle  $\omega$  by integrating Eq. (2.34) over  $0 \leq \omega \leq 2\pi$ . The azimuthally integrated angular flux is given by

$$\Psi(z, \mu, t) = \int_0^{2\pi} d\omega \bar{\psi}(z, \mu, \omega, t). \quad (2.35)$$

The azimuthally integrated differential scattering cross-section is written as

$$\Sigma_s(\mu, \mu') = \int_0^{2\pi} d\omega \Sigma_s(\mu, \mu', \omega) \quad (2.36)$$

Integrating Eq. (2.33) over  $\omega$  yields the mono-energetic transport equation in slab geometry:

$$\begin{aligned} \frac{1}{v} \frac{\partial \Psi(z, \mu, t)}{\partial t} + \mu \frac{\partial \Psi(z, \mu, t)}{\partial z} + \Sigma_t \Psi(z, \mu, t) \\ = \int_{-1}^1 d\mu' \Sigma_s(\mu, \mu') \Psi(z, \mu', t) + Q(z, \mu, t), \end{aligned} \quad (2.37)$$

where

$$Q(z, \mu, t) = \int_0^{2\pi} d\omega Q(z, \mu, \omega, t). \quad (2.38)$$

The spatial boundary conditions are now

$$\Psi(0, \mu, t) = \Psi_L(\mu), \quad \mu > 0, \quad (2.39)$$

$$\Psi(Z, \mu, t) = \Psi_R(\mu), \quad \mu < 0, \quad (2.40)$$

where  $Z$  is the length of the slab. The initial angular flux is specified as

$$\Psi(z, \mu, 0) = \Psi_i(z, \mu). \quad (2.41)$$

## 2.3 Mono-Energetic, Steady State Transport in Slab Geometry

One can further simplify Eq. (2.37) by making the assumption that enough time has passed in the system to become steady state. The angular flux and source will no longer change with respect to time, leading to:

$$\mu \frac{\partial \Psi(z, \mu)}{\partial z} + \Sigma_t \Psi(z, \mu) = \int_{-1}^1 d\mu' \Sigma_s(\mu, \mu') \Psi(z, \mu') + Q(z, \mu), \quad (2.42)$$

where the rate of change in the angular flux is now zero. The spatial boundary conditions reduce to:

$$\Psi(0, \mu) = \Psi_L(\mu), \quad \mu > 0, \quad (2.43)$$

$$\Psi(Z, \mu) = \Psi_R(\mu), \quad \mu < 0. \quad (2.44)$$

## Chapter 3: Solving the Transport Equation

The linear Boltzmann equation shown in Eq. (2.42) can be difficult to solve analytically. Numerical solutions are often necessary and many different algorithms have been developed [1, 4–6, 9, 10, 22, 23, 26, 29, 35, 52–56]. Deterministic and stochastic (or Monte Carlo) methods are typically employed. In general, Monte Carlo methods provide higher fidelity modeling, but come with a significant cost compared to deterministic methods. This document focuses on deterministic solvers that are approximations to the transport equation. These approximations are typically easier to solve with deterministic methods for certain classes of problems. The disadvantage of this approach is that accuracy is often sacrificed for faster convergence [1]. The two main classes of deterministic solvers are linear and nonlinear.

### 3.1 Approximations to the Transport Equation

Approximations to the transport equation are often used for speed and efficiency, but they come at the cost of accuracy. They can be very useful when the conditions of the problem allow for an accurate approximation. A wide range of approximations to the linear Boltzmann equation exist. Spherical harmonics, or the  $P_N$  approximation, is a well known approximation that was originally developed to model radiative transfer in stars [47, 57]. Solving the  $P_N$  approximation in three dimensions carries significant computational cost.

Solutions were difficult to obtain in the 1960s (and are still difficult today). The simplified  $P_N$  ( $SP_N$ ) approximation was introduced to work around this problem [49, 58–60]. Wynn-Epsilon [54] acceleration has been used to accelerate benchmark quality solutions to the 1-D multigroup transport equation [61]. This document will cover the diffusion approximation, the Fokker-Planck approximation, and the discrete ordinates approximation.

### 3.1.1 The Diffusion Approximation

The diffusion approximation [62] is a commonly used model for physical systems that are highly scattering. The diffusion equation has also been shown to be equivalent to the time dependent  $P_1$  approximation [46] as well as the  $S_2$  approximation [49]. The solution to the diffusion equation approaches the solution to the transport equation when the problem is highly scattering. In deriving the diffusion approximation, we assume that the angular flux depends weakly on direction  $\Omega$ , or that the scattering and angular flux are at most linearly anisotropic. For simplicity, we will also assume an external isotropic source. A source is considered isotropic when particles radiate from the source equally in all directions. As the problem becomes less scattering, the solution to the diffusion equation will deviate from the solution to the transport equation. When this happens, it is not ideal to use the diffusion approximation.

The diffusion equation can be derived from the transport equation by taking the zeroth and first moments of the transport equation [50, 63, 64].

We start with defining the scalar flux as

$$\phi_0(z) = \int_{-1}^1 d\mu \Psi(z, \mu), \quad (3.1)$$

and the net current as

$$\phi_1(z) = \int_{-1}^1 d\mu \mu \Psi(z, \mu). \quad (3.2)$$

We then integrate  $\int_{-1}^1(\cdot)d\mu$  over Eq. (2.42). This is called the zeroth order moment with respect to  $\mu$ . Performing the integration on Eq. (2.42) and using the relationships from Eqs. (3.1) and (3.2) results in

$$\frac{\partial \phi_1(z)}{\partial z} + \Sigma_t \phi_0(z) = \int_{-1}^1 d\mu \int_{-1}^1 d\mu' \Sigma_s(\mu, \mu') \Psi(z, \mu') + \int_{-1}^1 d\mu Q(z, \mu). \quad (3.3)$$

Let us investigate the inscattering term.

The azimuthally integrated differential scattering cross-section can be rewritten using a Legendre polynomial expansion and simplified to [44]:

$$\begin{aligned} \Sigma_s(\mu, \mu') &= \int_0^{2\pi} d\omega \Sigma_s(\mu, \mu', \omega) \\ &= \sum_{l=0}^{\infty} \frac{2l+1}{4\pi} \Sigma_{s,l} P_l(\mu, \mu') \int_0^{2\pi} d\omega \\ &= \sum_{l=0}^{\infty} \frac{2l+1}{2} \Sigma_{s,l} P_l(\mu, \mu') = \sum_{l=0}^{\infty} \frac{2l+1}{2} \Sigma_{s,l} P_l(\mu) P_l(\mu'). \end{aligned} \quad (3.4)$$

Substituting Eq. (3.4) into the inscattering term gives

$$\begin{aligned} \int_{-1}^1 d\mu \int_{-1}^1 d\mu' \Sigma_s(\mu, \mu') \Psi(z, \mu') &= \int_{-1}^1 d\mu \int_{-1}^1 d\mu' \sum_{l=0}^{\infty} \frac{2l+1}{2} \Sigma_{s,l} P_l(\mu) P_l(\mu') \Psi(z, \mu') \\ &= \sum_{l=0}^{\infty} \frac{2l+1}{2} \Sigma_{s,l} \int_{-1}^1 d\mu P_l(\mu) \int_{-1}^1 d\mu' P_l(\mu') \Psi(z, \mu'). \end{aligned} \quad (3.5)$$

We define the moments of angular flux as

$$\phi_l(z) = \int_{-1}^1 d\mu' P_l(\mu') \Psi(z, \mu'), \quad (3.6)$$

allowing us to express the scattering term as

$$\sum_{l=0}^{\infty} \frac{2l+1}{2} \Sigma_{s,l} \int_{-1}^1 d\mu P_l(\mu) \phi_l(z). \quad (3.7)$$

We continue by using the previously stated assumption that **the scattering is linearly anisotropic**. That is, the legendre polynomial representing the differential scattering cross-section will be expanded to only  $l = 1$ . This leads to

$$\sum_{l=0}^1 \frac{2l+1}{2} \Sigma_{s,l} \int_{-1}^1 d\mu P_l(\mu) \phi_l(z) = \frac{1}{2} \Sigma_{s,0} \int_{-1}^1 d\mu P_0(\mu) \phi_0(z) + \frac{3}{2} \Sigma_{s,1} \int_{-1}^1 d\mu P_1(\mu) \phi_1(z). \quad (3.8)$$

$P_0(\mu) = 1$  and  $P_1(\mu) = \mu$ , allowing further simplification to

$$\begin{aligned} \frac{1}{2} \Sigma_{s,0} \int_{-1}^1 d\mu P_0(\mu) \phi_0(z) + \frac{3}{2} \Sigma_{s,1} \int_{-1}^1 d\mu P_1(\mu) \phi_1(z) = \\ \frac{1}{2} \Sigma_{s,0} \int_{-1}^1 d\mu \phi_0(z) + \frac{3}{2} \Sigma_{s,1} \int_{-1}^1 d\mu \mu \phi_1(z) = \\ \Sigma_{s,0} \phi_0(z) + 0. \end{aligned} \quad (3.9)$$

Finally, putting everything together results in

$$\frac{\partial \phi_1(z)}{\partial z} + \Sigma_t \phi_0(z) = \Sigma_{s,0} \phi_0(z) + Q_0(z), \quad (3.10)$$

where

$$Q_0(z) = \int_{-1}^1 d\mu Q(z, \mu). \quad (3.11)$$

Next, we take the first order moment of Eq. (2.42) by applying  $\int_{-1}^1 (\cdot) \mu d\mu$  over the equation. Following the same steps as above gives

$$\begin{aligned} \frac{\partial}{\partial z} \int_{-1}^1 d\mu \mu^2 \Psi(z, \mu) + \Sigma_t \phi_1(z) = \left( \underbrace{\frac{1}{2} \Sigma_s \phi_0(z) \int_{-1}^1 d\mu \mu + \frac{3}{2} \Sigma_{s,1} \phi_1(z) \int_{-1}^1 d\mu \mu^2}_0 \right) \\ + \int_{-1}^1 d\mu \mu Q(z, \mu). \end{aligned} \quad (3.12)$$

To proceed, we now also assume **that the angular flux is linearly anisotropic**. To implement this assumption, the angular flux is expanded in angle and only the first two terms are retained (similar to what we just did with scattering):

$$\Psi(z, \mu) = \frac{1}{2} (\phi_0(z) + 3\phi_1(z)). \quad (3.13)$$

We insert this relationship into the streaming term in Eq. (3.12) and simplify to obtain

$$\frac{1}{3} \frac{\partial}{\partial z} \phi_0(z) + \Sigma_t \phi_1(z) = \Sigma_{s,1} \phi_1(z) + \int_{-1}^1 d\mu \mu Q(z, \mu). \quad (3.14)$$

Here, the diffusion approximation assumes that transport is steady state. Diffusive transport typically assumes that the source is isotropic, that is

$$Q(z, \mu) = \frac{Q(z)}{2}. \quad (3.15)$$

The conditions of steady state transport with an isotropic source are referred to as Fick's Law [64]. Substituting Eq. (3.15) into Eq. (3.14), we arrive at

$$\frac{1}{3} \frac{\partial}{\partial z} \phi_0(z) + \Sigma_t \phi_1(z) = \Sigma_{s,1} \phi_1(z), \quad (3.16)$$

or

$$\phi_1(z) = \frac{1}{3(\Sigma_{s,1} - \Sigma_t)} \frac{\partial \phi_0(z)}{\partial z}. \quad (3.17)$$

Finally, substituting Eq. (3.17) into Eq. (3.10) and assuming an isotropic source condition returns the diffusion equation:

$$\frac{-1}{3(\Sigma_t - \Sigma_{s,1})} \frac{\partial^2 \phi_0(z)}{\partial z^2} + \Sigma_a \phi_0(z) = Q(z), \quad (3.18)$$

where

$$\Sigma_a = \Sigma_t - \Sigma_s. \quad (3.19)$$

### 3.1.2 The Fokker-Planck Approximation

The diffusion approximation depends only on the zeroth and first order moments of angular flux. For highly scattering, forward-peaked problems, higher order moments carry necessary information about the system, which is not captured by the diffusion approximation. For forward-peaked scattering problems, a commonly used model known as

the Fokker-Planck (FP) approximation is used. The Fokker-Planck equation is an asymptotic limit of the linear Boltzmann equation under the forward-peaked condition; in other words, when the mean scattering cosine angle,  $\bar{\mu}_0$ , approaches unity.

We consider a homogeneous medium with mono-energetic, steady state transport in slab geometry, and rewrite the inscattering term using Legendre polynomials:

$$\mu \frac{\partial \Psi(z, \mu)}{\partial z} + \Sigma_t \Psi(z, \mu) = \underbrace{\sum_{l=0}^{\infty} \frac{2l+1}{2} \Sigma_{s,l} P_l(\mu) \phi_l(z)}_{S\Psi} + Q(z, \mu). \quad (3.20)$$

where  $S\Psi$  will represent the inscattering term for this derivation. The moments of angular flux are represented by

$$\phi_l(z) = \int_{-1}^1 d\mu' P_l(\mu') \Psi(z, \mu'). \quad (3.21)$$

We introduce a normalization for the scattering cross-section moments

$$\Sigma_{s,l} = \Sigma_s f_l, \quad (3.22)$$

where

$$f_l = \int_{-1}^1 d\mu f(\mu) P_l(\mu). \quad (3.23)$$

Under the forward-peaked condition, we assume that the mean cosine of the scattering angle, or  $\bar{\mu}_0$ , approaches 1. The scattering cross-section and moments are insignificant away from  $\bar{\mu}_0$ ; allowing us to Taylor-expand  $P_l(\mu)$  about one. Expanding to the first two terms gives

$$P_l(\mu) \approx 1 - \left. \frac{\partial P_l(\mu)}{\partial \mu} \right|_{\mu=1} (1 - \mu). \quad (3.24)$$

Recall the Legendre ordinary differential equation [44]:

$$\frac{\partial}{\partial \mu} (1 - \mu^2) \frac{\partial}{\partial \mu} P_l(\mu) = (1 - \mu^2) \frac{\partial^2 P_l(\mu)}{\partial \mu^2} - 2\mu \frac{\partial P_l(\mu)}{\partial \mu} = -l(l+1) P_l(\mu). \quad (3.25)$$



We evaluate Eq. (3.25) for  $\mu = 1$  and solve for  $\frac{\partial P_l(\mu)}{\partial \mu}$ . Note that  $P_l(1) = 1$  for all  $l$ . Substituting the result into Eq. (3.24) returns

$$P_l(\mu) \approx 1 - \frac{l(l+1)}{2}(1-\mu). \quad (3.26)$$

Replacing the relation from Eq. (3.26) in Eq. (3.23) results in

$$f_l = \int_{-1}^1 d\mu f(z, \mu) \left( 1 - \frac{l(l+1)}{2}(1-\mu) \right). \quad (3.27)$$

For clarity, we separate the integral before evaluating:

$$\begin{aligned} f_l &= \int_{-1}^1 d\mu f(\mu) \\ &\quad - \int_{-1}^1 d\mu f(\mu) \frac{l(l+1)}{2} \\ &\quad + \int_{-1}^1 d\mu f(\mu) \frac{l(l+1)}{2} \mu. \end{aligned} \quad (3.28)$$

Due to normalization  $\int_{-1}^1 d\mu f(\mu) = 1$ . Simplifying Eq. (3.28) gives

$$f_l = 1 - \frac{l(l+1)}{2}(1-\hat{\mu}), \quad (3.29)$$

where

$$\hat{\mu} = \int_{-1}^1 d\mu f(\mu) \mu. \quad (3.30)$$

The relationships from Eq. (3.22) and Eq. (3.29) update the inscattering term to

$$S\Psi = \Sigma_s \sum_{l=0}^{\infty} \frac{2l+1}{2} \left( 1 - \frac{l(l+1)}{2}(1-\hat{\mu}) \right) P_l(\mu) \phi_l(z), \quad (3.31)$$

where we have truncated the polynomial expansion at  $L$ . Expanding Eq. (3.31) gives

$$S\Psi = \Sigma_s \sum_{l=0}^{\infty} \frac{2l+1}{2} P_l(\mu) \phi_l(z) - \Sigma_s(1-\hat{\mu}) \sum_{l=0}^{\infty} \frac{2l+1}{2} P_l(\mu) \phi_l(z) \frac{l(l+1)}{2}. \quad (3.32)$$

Using the relationship from Eq. (3.25) and defining the momentum transfer cross-section as  $\Sigma_{tr} = \Sigma_s(1-\hat{\mu})$  results in

$$S\Psi = \Sigma_s \sum_{l=0}^{\infty} \frac{2l+1}{2} P_l(\mu) \phi_l(z) + \frac{\Sigma_{tr}}{2} \frac{\partial}{\partial \mu} (1-\mu^2) \frac{\partial}{\partial \mu} \sum_{l=0}^{\infty} \frac{2l+1}{2} P_l(\mu) \phi_l(z). \quad (3.33)$$

The angular flux can be represented by a linear combination of the flux moments:

$$\Psi(z) = \sum_{l=0}^{\infty} \frac{2l+1}{2} P_l(\mu) \phi_l(z). \quad (3.34)$$

Substituting the relationship from Eq. (3.34) into Eq. (3.33) returns

$$S\Psi = \Sigma_s \Psi(z) + \frac{\Sigma_{tr}}{2} \frac{\partial}{\partial \mu} (1 - \mu^2) \frac{\partial}{\partial \mu} \Psi(z). \quad (3.35)$$

Finally, updating the inscattering term in Eq. (3.20) using Eq. (3.35) gives the mono-energetic, steady state Fokker-Planck equation in slab geometry:

$$\mu \frac{\partial \Psi(z, \mu)}{\partial z} + \Sigma_a \Psi(z, \mu) = \frac{\Sigma_{tr}}{2} \frac{\partial}{\partial \mu} (1 - \mu^2) \frac{\partial}{\partial \mu} \Psi(z) + Q(z, \mu). \quad (3.36)$$

### 3.1.3 The Discrete Ordinates Approximation

The discrete ordinates approximation [65] is a widely used technique that holds Eq. (2.42) for a number of distinct angles  $\mu_n$  while a compatible quadrature approximation is applied to the integral term. An approximation is introduced to the integral term, where we no longer sum to  $\infty$  and now sum to a finite variable  $L$ . We have

$$\mu_n \frac{\partial \Psi(z, \mu_n)}{\partial z} + \Sigma_t \Psi(z, \mu_n) = \sum_{l=0}^L \frac{2l+1}{2} \Sigma_{s,l} P_l(\mu_n) \phi_l(z) + Q(z, \mu_n), \quad (3.37)$$

where  $\Psi(z, \mu_n)$  is typically written as  $\Psi_n(z)$  and  $\phi_l(z)$  contains the integral term

$$\phi_l(z) = \int_{-1}^1 d\mu' P_l(\mu') \Psi(z, \mu'). \quad (3.38)$$

We choose the directions such that the ordinates accurately evaluate the flux moments  $\phi_l(z)$  by a quadrature formula. Quadrature formulas most often are taken to operate on an even number of ordinates that are symmetric about  $\mu = 0$ . There are a wide variety of quadratures out there [66].

Gauss-Legendre is commonly used as an approximation to the definite integral of a function

$$\int_{-1}^1 f(x)dx \approx \sum_{i=1}^N w_i f(x_i). \quad (3.39)$$

It was constructed to yield an exact result for polynomials of degree  $2N - 1$  or less. In discrete ordinates, Gauss-Legendre quadrature is typically used to represent  $\phi_l(z)$  as

$$\phi_l(z) = \frac{1}{2} \sum_{n=1}^N w_n P_l(\mu_n) \Psi_n(z). \quad (3.40)$$

The weights  $w_n$  are given by [67]

$$w_n = \frac{2}{(1 - \mu_n^2) \left( \frac{\partial P_n(\mu_n)}{\partial \mu_n} \right)^2}, \quad (3.41)$$

where  $w_n > 0$  and the quadrature formula is normalized by

$$\sum_{n=1}^N w_n = 2. \quad (3.42)$$

The nodes  $\mu_n$  are determined by finding the  $n_{th}$  root of the associated Legendre polynomial  $P_N$ .

The zeroth and first Legendre polynomials are  $P_0(\mu_n) = 0$  and  $P_1(\mu_n) = \mu_n$ . Legendre polynomials for  $1 < n < N$  can be found using Bonnet's recursion formula [67]

$$(n+1)P_{n+1}(\mu_n) = (2n+1)\mu_n P_n(\mu_n) - nP_{n-1}(\mu_n). \quad (3.43)$$

## 3.2 Linear Solver Methods

Linear solver methods use iterative and direct approaches to solve differential equations. Matrix inversion is an example of a direct solver. Source iteration and synthetic acceleration are popular iterative linear solvers that have been developed to solve the transport equation.

### 3.2.1 Source Iteration

Source iteration (SI) is one of the most commonly used methods in transport [1, 65]. Consider a homogenous medium with mono-energetic, steady state transport in slab geometry. Equation (2.42) can be rewritten in operator form as

$$\left( \underbrace{\mu \frac{\partial}{\partial z} + \Sigma_t}_{\mathcal{L}} \right) \Psi = \left( \underbrace{\sum_{l=0}^L \frac{2l+1}{2} \Sigma_{s,l} P_l(\mu) \int_{-1}^1 d\mu' P_l(\mu')}_S \right) \Psi + Q, \quad (3.44)$$

where we have dropped the  $z$  and  $\mu$  notation in  $\Psi$  for simplicity. The SI method is mathematically described by

$$\mathcal{L}\Psi^{\ell+1} = S\Psi^{\ell} + Q, \quad (3.45)$$

where  $\ell$  is the iteration index, and the initial guess for angular flux  $\Psi^0$  is chosen by the user. The SI scheme works the following way: an estimate for the flux moments is found from the initial guess of the angular flux and the relationship shown in Eq. (3.21). Next, Eq. (3.45) is solved for  $\Psi^{\ell+1}$  by inverting the  $\mathcal{L}$  operator to obtain the next estimate of the angular flux. The angular flux is used in Eq. (3.21) to obtain the new estimate of the flux moments. This iterative process is repeated until some convergence criterion is met.

For problems that have low scattering and high leakage, the SI method converges rapidly [1]. However, for optically thick, highly scattering problems, SI becomes inefficient and expensive, leading to slow convergence [29]. Newer methods have been developed to tackle problems with high scattering and optically thick media, as well as problems with anisotropic scattering. In the following sections, we discuss acceleration techniques that take advantage of approximations given in Chapter 2 that speed up convergence rates for these types of problems.

### 3.2.2 Synthetic Acceleration

An efficient acceleration technique known as synthetic acceleration is commonly used today. Synthetic acceleration introduces a second step to the SI process that speeds up convergence [1, 65, 68]. We begin with a single source iteration, or transport sweep:

$$\mathcal{L}\Psi^{\ell+\frac{1}{2}} = S\Psi^\ell + Q. \quad (3.46)$$

where  $\Psi^{\ell+\frac{1}{2}}$  is the estimation, or prediction, for the next iteration of angular flux  $\Psi^{\ell+1}$ . We want  $\Psi^{\ell+1}$  to be a more accurate approximation to  $\Psi$  so we include a second stage in the process.

We subtract Eq. (3.46) from Eq. (3.44) to obtain

$$\mathcal{L}\left(\Psi - \Psi^{\ell+\frac{1}{2}}\right) = S\left(\Psi - \Psi^\ell\right) = S\left(\Psi - \Psi^{\ell+\frac{1}{2}}\right) + S\left(\Psi^{\ell+\frac{1}{2}} - \Psi^\ell\right). \quad (3.47)$$

Rearranging terms in Eq. (3.47) gives us the the exact solution  $\Psi$  in terms of  $\Psi^{\ell+\frac{1}{2}}$  and  $\Psi^\ell$ ,

$$(\mathcal{L} - S)\left(\Psi - \Psi^{\ell+\frac{1}{2}}\right) = S\left(\Psi^{\ell+\frac{1}{2}} - \Psi^\ell\right), \quad (3.48)$$

or

$$\Psi = \Psi^{\ell+\frac{1}{2}} + (\mathcal{L} - S)^{-1} S\left(\Psi^{\ell+\frac{1}{2}} - \Psi^\ell\right). \quad (3.49)$$

Equation (3.49) yields the exact equation for the additive correction  $\Psi - \Psi^{\ell+\frac{1}{2}}$  [1]. Inverting the transport operator  $(\mathcal{L} - S)$  in Eq. (3.49) would be solving the transport equation exactly. This would be inefficient and expensive, so instead we use an approximation to the  $(\mathcal{L} - S)$  operator:

$$\mathcal{P} \approx (\mathcal{L} - S) \quad (3.50)$$

such that  $\mathcal{P}^{-1}$  is easier to evaluate than  $(\mathcal{L} - S)^{-1}$ .

The synthetic acceleration process is then described by a predict and correct stage:

$$\text{Predict : } \mathcal{L} \psi^{m+\frac{1}{2}} = S \psi^m + Q, \quad (3.51a)$$

$$\text{Correct : } \psi^{m+1} = \psi^{m+\frac{1}{2}} + \mathcal{P}^{-1} S \left( \psi^{m+\frac{1}{2}} - \psi^m \right), \quad (3.51b)$$

where  $\mathcal{P}$  can be represented by any approximation, such as the Diffusion or Fokker-Planck approximation.

In Diffusion Synthetic Acceleration (DSA), the operator  $\mathcal{P}$  in Eq. (3.51b) is given by [1, 3, 7]

$$\mathcal{P} = \left( \frac{-1}{3(\Sigma_t - \Sigma_{s,1})} \frac{d^2}{dz^2} + \Sigma_a \right) \int_{-1}^1 (\cdot) d\mu, \quad (3.52)$$

leading to the DSA scheme:

$$\text{Predict : } \mathcal{L} \psi^{m+\frac{1}{2}} = S \psi^m + Q, \quad (3.53a)$$

$$\text{Correct : } \psi^{m+1} = \psi^{m+\frac{1}{2}} + \quad (3.53b)$$

$$\left[ \left( \frac{-1}{3(\Sigma_t - \Sigma_{s,1})} \frac{d^2}{dz^2} + \Sigma_a \right) \int_{-1}^1 (\cdot) d\mu \right]^{-1} S \left( \psi^{m+\frac{1}{2}} - \psi^m \right). \quad (3.53c)$$

DSA begins with one transport sweep (or source iteration) to get a prediction for the next iteration of angular flux. The prediction is corrected using Eq. (3.53b) and the next iteration of angular flux is given. This procedure is continued until some convergence criteria is met.

### 3.2.3 Preconditioning

Preconditioning is an alternative to synthetic acceleration that is well known in the mathematical community. A popular iteration scheme that utilizes preconditioning is Preconditioned Richardson iteration [52, 69]. It can be shown that synthetic acceleration is mathematically equivalent to preconditioning. We operate  $\mathcal{L}^{-1}$  on Eq. (3.45) and define

$$A = I - \mathcal{L}^{-1} S, \quad (3.54a)$$

$$\hat{q} = \mathcal{L}^{-1} Q, \quad (3.54b)$$

where  $I$  is an identity matrix, to obtain

$$\Psi^{\ell+1} = (I - A) \Psi^\ell + \hat{q}. \quad (3.55)$$

Equation (3.55) is known as the Richardson Iteration scheme and is a special case of source iteration [70]. Next we rewrite Eq. (3.55) as

$$\Psi^{\ell+\frac{1}{2}} = (I - A) \Psi^\ell + \hat{q}. \quad (3.56)$$

We eliminate  $\Psi^{\ell+\frac{1}{2}}$  using the relationship in Eq. (3.51b), resulting in

$$\Psi^{\ell+1} = \Psi^\ell + (I + \mathcal{P}^{-1}S) (-A\Psi^\ell + \hat{q}). \quad (3.57)$$

Defining

$$P = I + \mathcal{P}^{-1}S \quad (3.58)$$

allows us to write Eq. (3.57) as

$$\Psi^{\ell+1} = (I - PA) \Psi^\ell + P\hat{q}. \quad (3.59)$$

Equation (3.59) is referred to as the Preconditioned Richardson iteration scheme with preconditioner  $P$ . The same procedure of source iteration can be applied to this preconditioned iteration scheme. Consequently, the general synthetic acceleration scheme can be viewed as a Preconditioned Richardson iteration.

### 3.3 Nonlinear Solver Methods

Nonlinear solvers and accelerators are used to solve systems of equations that are nonlinearly coupled. There are two main types of coupling, loose and tight. This section will cover popular methods for both types of coupling.

### 3.3.1 Picard Iteration

One of the most robust methods for solving systems of loosely coupled nonlinear equations is the fixed-point iteration, also referred to as Picard or nonlinear Richardson iteration [30, 53].

Picard iteration works by solving the first equation for the first unknown, given the second unknown, and the second equation for the second unknown, given the first. We start with two functions that depend on  $\mathbf{x} = (x_1, x_2)$ , that is

$$F_1(\mathbf{x}) = F_1(x_1, x_2) = 0, \quad (3.60a)$$

$$F_2(\mathbf{x}) = F_2(x_1, x_2) = 0. \quad (3.60b)$$

Given initial iterates  $x_1^0, x_2^0$ , the Picard algorithm can be setup as follows

$$\text{Solve for } v : F_1(v, x_2^\ell) = 0, \quad (3.61a)$$

$$\text{Update } x_1 : x_1^{\ell+1} = v, \quad (3.61b)$$

$$\text{Solve for } w : F_2(x_1^{\ell+1}, w) = 0, \quad (3.61c)$$

$$\text{Update } x_2 : x_2^{\ell+1} = w. \quad (3.61d)$$

Iteration is done until some convergence criterion is met.

Nonlinear diffusion acceleration (NDA) [1] is a popular nonlinear acceleration technique that can be solved with Picard iteration [71]. Given initial flux moments  $\phi_l^0$ , the NDA Picard



algorithm is given by

$$\text{Solve for } \Psi^{\ell+\frac{1}{2}} : \left( \mu \frac{\partial}{\partial z} + \Sigma_t \right) \Psi^{\ell+\frac{1}{2}} = \sum_{l=0}^L \frac{2l+1}{2} \Sigma_{s,l} P_l(\mu) \phi_l^\ell + Q, \quad (3.62a)$$

$$\text{Update } \hat{D} : \hat{D} \phi_0^{\ell+\frac{1}{2}} = \left( \phi_1^{\ell+\frac{1}{2}} + \frac{1}{3(\Sigma_t - \Sigma_{s,1})} \frac{\partial \phi_0^{\ell+\frac{1}{2}}}{\partial z} \right), \quad (3.62b)$$

$$\text{Solve for } \phi_0^{\ell+1} : \left[ \left( \frac{\partial}{\partial z} \frac{-1}{3(\Sigma_t - \Sigma_{s,1})} \frac{\partial}{\partial z} + \hat{D} \right) + \Sigma_a \right] \phi_0^{\ell+1} = Q, \quad (3.62c)$$

$$\text{Update } \phi_0 : \phi_0^\ell = \phi_0^{\ell+1}, \quad (3.62d)$$

where  $\hat{D}$  is referred to as the consistency term. The role of  $\hat{D}$  is to keep the solutions of the transport equation and diffusion equation consistent. First, a transport sweep is performed. The consistency term is solved for using the current and scalar flux found from the transport sweep. The consistency term is included in the diffusion solve to get the next scalar flux estimate. The scalar flux estimate is then used in the following transport sweep. Iteration is continued until some convergence criterion is met. It is important to note that NDA is only accelerating up to the first two moments, which can lead to poor performance when the higher order moments carry more information about the system.

### 3.3.2 Newton's Method

Convergence of Picard iteration is typically linear and can result in slow convergence even when starting with a good initial guess at the solution [30, 53]. Newton's method is used to solve tightly coupled nonlinear equations and can offer faster (up to quadratic) convergence [30, 53]. Newton's method typically requires that the function derivatives can be calculated directly. Approximations can be used if the analytical expression of the derivative is not easily obtainable, but this can lead to slower convergence times.

Using Eq. (3.60) one can construct a Jacobian matrix,  $J$ , such that

$$J = \begin{bmatrix} \frac{\partial F_1}{\partial x_1} & \frac{\partial F_1}{\partial x_2} \\ \frac{\partial F_2}{\partial x_1} & \frac{\partial F_2}{\partial x_2} \end{bmatrix}. \quad (3.63)$$

The Newton algorithm is given by the following, given initial guess  $\mathbf{x}^0$  and function  $F(\mathbf{x}^0) = (F_1(\mathbf{x}^0), F_2(\mathbf{x}^0))$ :

$$\text{Solve : } J(\mathbf{x}^\ell) \boldsymbol{\delta x} = -F(\mathbf{x}^\ell), \quad (3.64a)$$

$$\text{Update : } \mathbf{x}^{\ell+1} = \mathbf{x}^\ell + \boldsymbol{\delta x}, \quad (3.64b)$$

where  $\boldsymbol{\delta x} = (\delta x_1, \delta x_2)$ . Newton's method begins with initial guess  $\mathbf{x}^0$ . The Jacobian is inverted in Eq. (3.64a) to solve for  $\boldsymbol{\delta x}$ . We update  $\mathbf{x}^{\ell+1}$  by adding on  $\boldsymbol{\delta x}$  to  $\mathbf{x}^\ell$ . Iteration is done until some precision requirement is met.

## Chapter 4: A New Fokker-Planck Acceleration Technique

Acceleration schemes that use the Fokker-Planck approximation are relatively new, and research is ongoing [28, 48]. For forward-peaked, highly scattering problems, acceleration using the FP approximation has shown significant improvement on convergence rate versus acceleration using the diffusion approximation [28]. This chapter will discuss an acceleration technique known as Fokker-Planck synthetic acceleration (FPSA), derive the new method referred to as Modified Fokker-Planck Acceleration, (MFPA), describe the methodology of MFPA, and discuss the relationship between FPSA and MFPA. The goal of this new method is to have consistency between a high-order transport equation and a low-order Fokker-Planck equation. Setting up the method this way in mutlipysics problems allows for isolation of high-order transport sweeps through coupling of the low-order FP equation.

### 4.1 Fokker-Planck Synthetic Acceleration

FPSA is a relatively new method that uses synthetic acceleration to speed up the convergence of forward-peaked, highly scattering problems. In the FPSA scheme [28, 29], the FP approximation is used to synthetically accelerate convergence when solving Eq. (3.51). The operator  $\mathcal{P}$  in Eq. (3.51b) is given by [28, 29]

$$\mathcal{P} = \mathcal{A} - \mathcal{F} = \underbrace{\left( \mu \frac{\partial}{\partial z} + \Sigma_a \right)}_{\mathcal{A}} - \underbrace{\left( \frac{\Sigma_{tr}}{2} \frac{\partial}{\partial \mu} (1 - \mu^2) \frac{\partial}{\partial \mu} \right)}_{\mathcal{F}}. \quad (4.1)$$

The FP approximation is used to estimate the error in the prediction. The prediction is corrected and the next iteration is performed if convergence criterion is not met. The scheme is given by the following:

$$\text{Predict : } \mathcal{L}\psi^{m+\frac{1}{2}} = S\psi^m + Q, \quad (4.2a)$$

$$\text{Correct : } \psi^{m+1} = \psi^{m+\frac{1}{2}} + (\mathcal{A} - \mathcal{F})^{-1}S\left(\psi^{m+\frac{1}{2}} - \psi^m\right). \quad (4.2b)$$

FPSA has the advantage of accelerating up to  $N$  moments of angular flux and can converge up to three order of magnitudes faster when compared to standard acceleration techniques such as DSA or NDA [28, 29]. DSA and NDA do not utilize the higher order moments(they only accelerate up to the first moment) and show poor performance due to this. A flowchart of this algorithm is shown in Fig. 4.1.

As stated in Chapter 3, synthetic acceleration and preconditioning are equivalent. Research into creating an effective Fokker-Planck preconditioner is still ongoing [28, 29]. An effective FP solver needs to be further developed for an attractive FP preconditioning method.

It is important to note that with FPSA, there is no consistency between the FP approximation and the transport equation. The FP equation is used to synthetically accelerate the transport equation by correcting error in the moments of angular flux. An acceleration setup where the FP equation is consistent with the transport equation can be very useful, especially for multiphysics problems. By creating a FP equation that is consistent with the transport equation, the consistent FP equation can be coupled in multiphysics problems in place of the transport equation. This should lead to faster convergence times by isolating expensive transport sweeps.

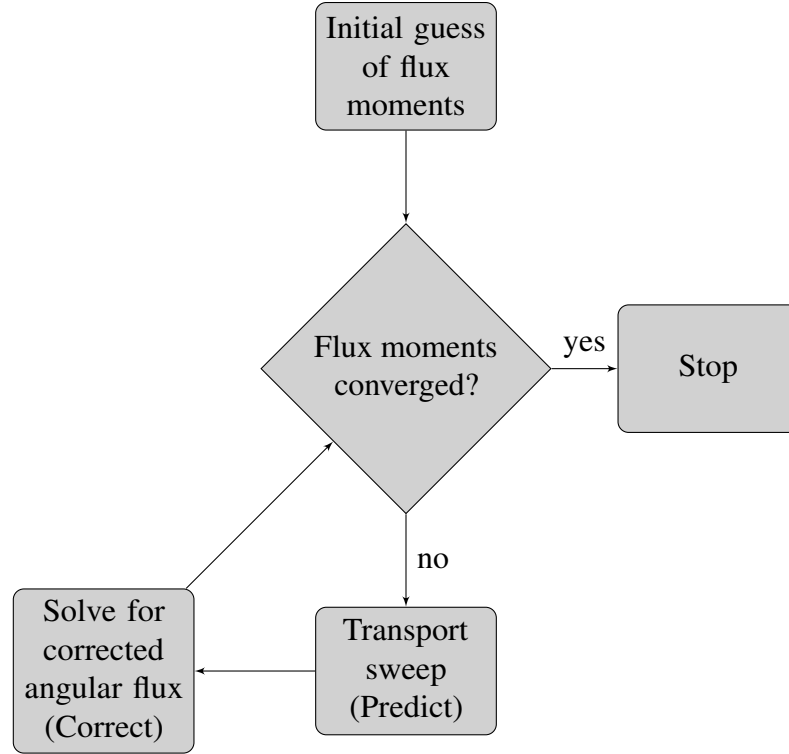


Figure 4.1: MFPA algorithm

## 4.2 Modified Fokker-Planck Acceleration

Modified Fokker-Planck Acceleration similarly takes advantage of the Fokker-Planck approximation to accelerate the solution to the linear Boltzmann equation. However MFPA preserves the moments of angular flux of the transport equation, allowing for multiphysics applications. This will be shown in Chapter 7. In this section we will derive the MFPA method and methodology.

### 4.2.1 MFPA using a Linear Consistency Term

Consider a homogeneous system with monoenergetic, steady state transport in slab geometry. Under these conditions the linear Boltzmann equation is given by Eq. (2.42)

and the Fokker-Planck equation is given by Eq. (3.36). We want the solutions of both equations to be the same. To do this we start with introducing a linear consistency term  $\hat{D}_F$  to Eq. (3.36), obtaining a modified Fokker-Planck (MFP) equation

$$\mu \frac{\partial \Psi(z, \mu)}{\partial z} + \Sigma_a \Psi(z, \mu) = \frac{\Sigma_{tr}}{2} \frac{\partial}{\partial \mu} (1 - \mu^2) \frac{\partial}{\partial \mu} \Psi(z, \mu) + \hat{D}_F(z, \mu) + Q(z, \mu). \quad (4.3)$$

The role of  $\hat{D}_F$  is to force the transport and modified FP equations to be consistent. This consistency term can be defined in a number of ways, and its choice may determine the numerical stability of the method. The expression for  $\hat{D}_F$  is found by subtracting Eq. (4.3) from Eq. (2.42). After subtraction and rearrangement of terms, we arrive at

$$\hat{D}_F = \sum_{l=0}^L \frac{(2l+1)}{2} \Sigma_{s,l} P_l(\mu) \phi_l(z) - \frac{\Sigma_{tr}}{2} \frac{\partial}{\partial \mu} (1 - \mu^2) \frac{\partial \Psi(z, \mu)}{\partial \mu} - \Sigma_{s,0} \Psi(z, \mu). \quad (4.4)$$

The MFPA method is given by the following equations:

$$\mu \frac{\partial \Psi}{\partial z} + \Sigma_t \Psi = \sum_{l=0}^L \frac{2l+1}{2} \Sigma_{s,l} P_l \phi_l + Q, \quad (4.5a)$$

$$\mu \frac{\partial \Psi}{\partial z} + \Sigma_a \Psi = \frac{\Sigma_{tr}}{2} \frac{\partial}{\partial \mu} (1 - \mu^2) \frac{\partial}{\partial \mu} \Psi + \hat{D}_F + Q, \quad (4.5b)$$

$$\hat{D}_F = \sum_{l=0}^L \frac{(2l+1)}{2} \Sigma_{s,l} P_l \phi_l - \frac{\Sigma_{tr}}{2} \frac{\partial}{\partial \mu} (1 - \mu^2) \frac{\partial \Psi}{\partial \mu} - \Sigma_{s,0} \Psi, \quad (4.5c)$$

where we have dropped the  $z$  and  $\mu$  notation for clarity.

The system of equations given in Eqs. (4.5) can be solved using a variety of linear solution techniques [72]. Although our system of equations is linear, we take advantage of Picard iteration in MFPA:

$$\text{Transport Sweep : } \mathcal{L} \Psi^{\ell+\frac{1}{2}} = S \Psi^\ell + Q, \quad (4.6a)$$

$$\text{Evaluate Consistency Term : } \hat{D}_F^{\ell+1} = (S - \mathcal{F} - \Sigma_{s,0} I) \Psi^{\ell+\frac{1}{2}}, \quad (4.6b)$$

$$\text{Solve MFP Equation : } \Psi^{\ell+1} = \mathcal{P}^{-1} \left( \hat{D}_F^{\ell+1} + Q \right), \quad (4.6c)$$

where  $\Psi^\ell$  is the angular flux from the previous iteration,  $\Psi^{\ell+\frac{1}{2}}$  is the initial estimate for angular flux,  $\Psi^{\ell+1}$  is the next iteration of angular flux,  $\mathcal{L}$  and  $S$  are given in Eq. (3.44),  $\mathcal{P}$  and  $\mathcal{F}$  are given in Eq. (4.1),  $I$  is the identity operator, and  $\ell$  is the iteration index. Iteration is done until a convergence criterion is met.

We use Picard iteration here to separate the linear Boltzmann equation from the modified FP equation. The goal is to couple the MFP equation in multiphysics problems and isolate the transport equation. Isolating the transport equation and coupling the low order approximation has shown improvement on convergence rate when using NDA [23]. We want to apply the same approach when using the FP approximation. **FPSA does not have the ability to separate the FP equation to couple with multiphysics.**

The main advantage of setting up the MFP equation using a linear consistency term is that the matrix  $\mathcal{P}$  needs to be setup and inverted *only once*, just as with FPSA [29]. This has a large impact on the method's performance. A flowchart of this algorithm is shown in Fig. 4.2.

An alternative way to solve Eqs. (4.5) would be to use a linear solver known as the generalized minimum residual method (GMRES) [2]. GMRES is commonly used to solve linear systems [56, 73]. First we need to rewrite Eqs. (4.5) in the following way

$$\text{LBE} : \mathcal{L}\Psi_1 = S\Psi_2 + Q, \quad (4.7a)$$

$$\text{MFP} : \mathcal{P}\Psi_2 = \hat{D}_F + Q, \quad (4.7b)$$

$$\text{Consistency Term} : \hat{D}_F = (S - \mathcal{F} - \Sigma_{s,0}I)\Psi_1. \quad (4.7c)$$

where  $\Psi_1$  is the unknown angular flux from the LBE,  $\Psi_2$  is the unknown angular flux from the MFP.

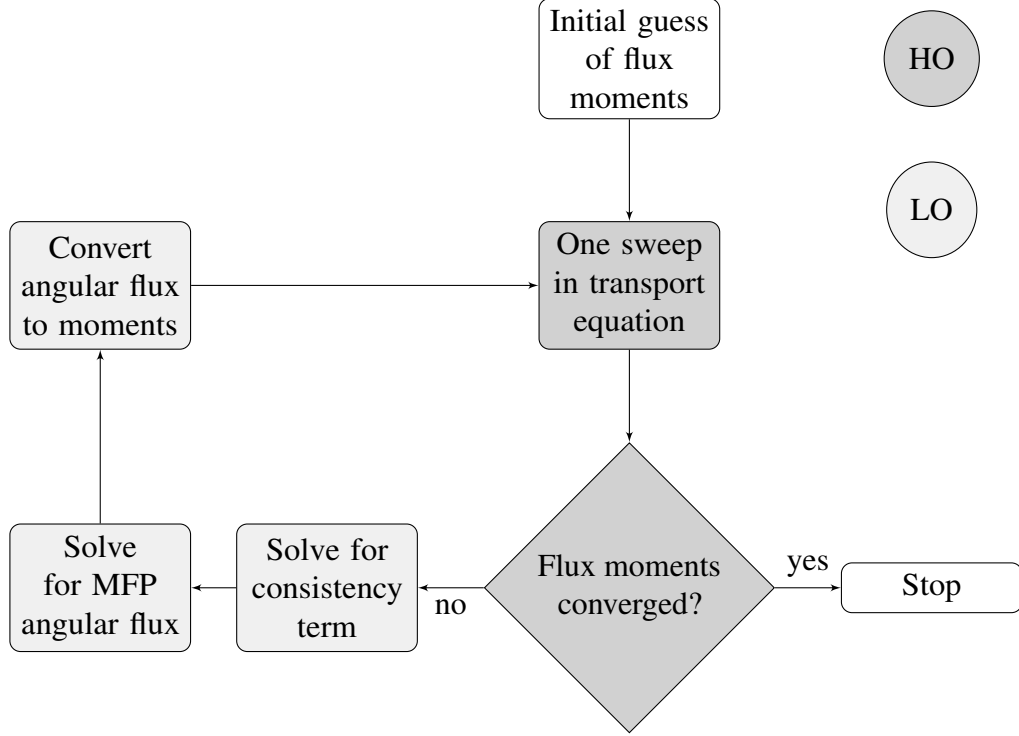


Figure 4.2: MFPA algorithm

We can substitute the expression for  $\hat{D}_F$  into Eq. (4.7b) to get

$$\mathcal{P}\Psi_2 = \underbrace{(S - \mathcal{F} - \Sigma_{s,0}I)}_{\mathcal{B}} \Psi_1 + Q. \quad (4.8)$$

Solving for  $\Psi_2$  in Eq. (4.8) we get

$$\Psi_2 = \mathcal{P}^{-1}(\mathcal{B}\Psi_1 + Q). \quad (4.9)$$

Substituting the expression for Eq. (4.9) into Eq. (4.7a) gives

$$\mathcal{L}\Psi_1 = S[\mathcal{P}^{-1}(\mathcal{B}\Psi_1 + Q)] + Q. \quad (4.10)$$

Finally, we solve for  $\Psi_1$  to arrive at

$$\Psi_1 = (I - \mathcal{L}^{-1}S\mathcal{P}^{-1}\mathcal{B})^{-1}[\mathcal{L}^{-1}(S\mathcal{P}^{-1} + I)Q]. \quad (4.11)$$



Here,  $\Psi_1$  is the angular flux from Eq. (4.7a) that is also consistent with the angular flux  $\Psi_2$  from Eq. (4.7b). Setting up MFPA for a linear or direct solve does not offer the advantage that the MFPA setup for Picard iteration has. Coupling Eq. (4.11) with a multiphysics problem would not isolate transport sweeps. By setting up MFPA for a Picard solve, we change the approach of coupling with multiphysics problems. The coupling of the FP equation isolates the transport equation, resulting in faster convergence.

### 4.2.2 MFPA using Nonlinear Consistency Terms

The definition of the consistency term used in Eq. (4.3) is not unique. The NDA scheme primarily uses a nonlinear consistency term [18] which warrants an inspection of the performance of MFPA using a nonlinear consistency term. Two different nonlinear terms will be introduced and discussed in this section.

We begin with defining the nonlinear consistency term  $D\Psi$  and adding it to Eq. (3.36):

$$\mu \frac{\partial \Psi(z, \mu)}{\partial z} + \Sigma_a \Psi(z, \mu) = \frac{\Sigma_{tr}}{2} \frac{\partial}{\partial \mu} (1 - \mu^2) \frac{\partial}{\partial \mu} \Psi(z, \mu) + D(z, \mu) \Psi(z, \mu) + Q(z, \mu). \quad (4.12)$$

Following the same procedure in Section 4.2.1, we derive an expression for  $D$ :

$$D = \frac{\sum_{l=0}^L \frac{(2l+1)}{2} P_l \Sigma_l \phi_l - \frac{\Sigma_{tr}}{2} \frac{\partial}{\partial \mu} (1 - \mu^2) \frac{\partial \Psi}{\partial \mu}}{\Psi} - \Sigma_{s,0}, \quad (4.13)$$

and the nonlinear MFPA method:

$$\mu \frac{\partial \Psi_{HO}}{\partial x} + \Sigma_t \Psi_{HO} = \sum_{l=0}^L \frac{(2l+1)}{2} P_l \Sigma_{s,l} \phi_{l,LO} + Q, \quad (4.14a)$$

$$\mu \frac{\partial \Psi_{LO}}{\partial x} + \Sigma_a \Psi_{LO} = \frac{\Sigma_{tr}}{2} \frac{\partial}{\partial \mu} (1 - \mu^2) \frac{\partial \Psi_{LO}}{\partial \mu} + D \Psi_{LO} + Q, \quad (4.14b)$$

$$D = \frac{\sum_{l=0}^L \frac{(2l+1)}{2} P_l \Sigma_{s,l} \phi_{l,HO} - \frac{\Sigma_{tr}}{2} \frac{\partial}{\partial \mu} (1 - \mu^2) \frac{\partial \Psi_{HO}}{\partial \mu}}{\Psi_{HO}} - \Sigma_{s,0}. \quad (4.14c)$$

To solve Eqs. (4.14), we use Picard iteration similar to Eqs. (4.6):

$$\text{Transport Sweep : } \mathcal{L}\Psi_{HO}^{k+1} = \mathcal{S}\Psi_{LO}^k + Q, \quad (4.15a)$$

$$\text{Evaluate Consistency Term : } D^{k+1} = \frac{(\mathcal{S} - \mathcal{F})\Psi_{HO}^{k+1}}{\Psi_{HO}^{k+1}} - \Sigma_{s,0}\mathcal{I}, \quad (4.15b)$$

$$\text{Solve MFP Equation : } \Psi_{LO}^{k+1} = \left( \mathcal{P} - D^{k+1} \right)^{-1} Q. \quad (4.15c)$$

The disadvantage of setting up the consistency term this way is that it leads to a potential numerical problem in Eq. (4.15b). If there is zero angular flux anywhere, such as a transport problem with a beam boundary condition, numerical catastrophe will be introduced due to the division by zero in Eq. (4.15b).

Alternatively we can introduce the nonlinear consistency term  $\bar{D}(1 + \Psi)$  that solves the numerical instability issue. Setting up MFPA with this consistency term leads to the scheme:

$$\mu \frac{\partial \Psi_{HO}}{\partial x} + \Sigma_t \Psi_{HO} = \sum_{l=0}^L \frac{(2l+1)}{2} P_l \Sigma_{s,l} \phi_{l,LO} + Q, \quad (4.16a)$$

$$\mu \frac{\partial \Psi_{LO}}{\partial x} + \Sigma_a \Psi_{LO} = \frac{\Sigma_{tr}}{2} \frac{\partial}{\partial \mu} (1 - \mu^2) \frac{\partial \Psi_{LO}}{\partial \mu} + \bar{D}(1 + \Psi_{LO}) + Q, \quad (4.16b)$$

$$\bar{D} = \frac{\sum_{l=0}^L \frac{(2l+1)}{2} P_l \Sigma_{s,l} \phi_{l,HO} - \frac{\Sigma_{tr}}{2} \frac{\partial}{\partial \mu} (1 - \mu^2) \frac{\partial \Psi_{HO}}{\partial \mu} - \Sigma_{s,0} \Psi_{HO}}{1 + \Psi_{HO}}. \quad (4.16c)$$

Solving Eqs. (4.16) using Picard iteration gives the following setup:

$$\text{Transport Sweep : } \mathcal{L}\Psi_{HO}^{k+1} = \mathcal{S}\Psi_{LO}^k + Q, \quad (4.17a)$$

$$\text{Evaluate Consistency Term : } \bar{D}^{k+1} = \frac{(\mathcal{S} - \mathcal{F} - \Sigma_{s,0}\mathcal{I})\Psi_{HO}^{k+1}}{1 + \Psi_{HO}^{k+1}}, \quad (4.17b)$$

$$\text{Solve MFP Equation : } \Psi_{LO}^{k+1} = \left( \mathcal{P} - \bar{D}^{k+1} \right)^{-1} \left( \bar{D}^{k+1} + Q \right). \quad (4.17c)$$

Problems with zero angular flux will not have numerical instability when using the  $\bar{D}(1 + \Psi)$  consistency term.

The drawback of using a nonlinear consistency term is that the inverted matrices in Eqs. (4.15c) and (4.17c) need to be setup at each iteration, leading to performance loss when compared to MFPA with a linear consistency term.

### 4.3 Equivalency between MFPA and FPSA

It can be shown that MFPA using a linear consistency term and FPSA are mathematically equivalent. Substituting Eq. (4.6b) into Eq. (4.6c) gives

$$\begin{aligned}\Psi^{\ell+1} &= \mathcal{P}^{-1} \left( (S - \mathcal{F} - \Sigma_{s,0}I) \Psi^{\ell+\frac{1}{2}} + Q \right), \\ &= \mathcal{P}^{-1} \left( (S - \mathcal{A} + \mathcal{P} - \Sigma_{s,0}I) \Psi^{\ell+\frac{1}{2}} + Q \right), \\ &= \Psi^{\ell+\frac{1}{2}} + \mathcal{P}^{-1} \left( (S - \mathcal{A} - \Sigma_{s,0}I) \Psi^{\ell+\frac{1}{2}} + Q \right).\end{aligned}\tag{4.18}$$

Substituting the expression of the source term  $Q$  from Eq. (4.6a) into Eq. (4.18) results in

$$\begin{aligned}\Psi^{\ell+1} &= \Psi^{\ell+\frac{1}{2}} + \mathcal{P}^{-1} \left( (S - \mathcal{A} - \Sigma_{s,0}I) \Psi^{\ell+\frac{1}{2}} + \mathcal{L}\Psi^{\ell+\frac{1}{2}} - S\Psi^{\ell} \right), \\ &= \Psi^{\ell+\frac{1}{2}} + \mathcal{P}^{-1} S \left( \Psi^{\ell+\frac{1}{2}} - \Psi^{\ell} \right) + \mathcal{P}^{-1} \left( (-\mathcal{A} - \Sigma_{s,0}I) \Psi^{\ell+\frac{1}{2}} + \mathcal{L}\Psi^{\ell+\frac{1}{2}} \right), \\ &= \Psi^{\ell+\frac{1}{2}} + \mathcal{P}^{-1} S \left( \Psi^{\ell+\frac{1}{2}} - \Psi^{\ell} \right) + \mathcal{P}^{-1} \underbrace{(\mathcal{L} - \mathcal{A} - \Sigma_{s,0}I)}_0 \Psi^{\ell+\frac{1}{2}}.\end{aligned}\tag{4.19}$$

Consequently, Eq. (4.21) and the correction stage of Eq. (4.2) are equivalent. Therefore, the performance of FPSA and linear MFPA are expected to be the same.

MFPA using a nonlinear consistency term and FPSA are not mathematically equivalent.

Substituting Eq. (4.15b) into Eq. (4.15c) gives

$$\Psi^{\ell+1} = \left( \mathcal{P} - \frac{(S - \mathcal{F} - \Sigma_{s,0}I) \Psi^{\ell+\frac{1}{2}}}{\Psi^{\ell+\frac{1}{2}}} \right)^{-1} Q.\tag{4.20}$$

Following the substitution of the expression of the source term  $Q$  from Eq. (4.15a) into Eq. (4.21) results in

$$\Psi^{\ell+1} = \left( \mathcal{P} - \frac{(S - \mathcal{F} - \Sigma_{s,0}I) \Psi^{\ell+\frac{1}{2}}}{\Psi^{\ell+\frac{1}{2}}} \right)^{-1} (\mathcal{L}\Psi^{\ell+\frac{1}{2}} - S\Psi^{\ell}).\tag{4.21}$$

From here there is no discernible way to simplify Eq. (4.21) into an equation that is equivalent to the correction stage of Eq. (4.2).

## Chapter 5: Discretization

This chapter describes the discretization techniques used in this work to numerically solve the transport and FP equations. We use Gauss-Legendre quadrature alongside the discrete ordinates approximation to discretize the transport and Fokker-Planck equations in angle. The moment preserving discretization technique is used to discretize the Fokker-Planck operator. The transport and Fokker-Planck equations are discretized in space using the finite element method.

### 5.1 Fokker-Planck Operator

Gauss-Legendre is used to discretize the FP equation in angle. The derivatives of angular flux in the FP equation can be discretized using standard finite-difference approximations. Weighted finite-difference (WFD) schemes have been developed for discrete ordinates to preserve the zeroth and first moments of angular flux [74]. The application of WFD schemes is geared towards diffusive problems. A Moment Preserving Discretization (MPD) has been developed that preserves up to  $N$  moments of angular flux and is used in this paper [74]. The MPD used for the FP equation is given below. We start with the discrete ordinates FP equation:

$$\mu_n \frac{\partial \Psi_n(z)}{\partial z} + \Sigma_a \Psi_n(z) - \frac{\Sigma_{tr}}{2} \nabla_n^2 \Psi_n(z) = Q_n(z), \quad (5.1)$$

for  $n = 1, \dots, N$ . Here,  $\nabla_n^2 = \frac{\partial}{\partial \mu}(1 - \mu_n^2)\frac{\partial}{\partial \mu}$  is the discrete form of the angular Laplacian operator evaluated at angle  $n$ .

The MPD scheme is used to discretize the angular Laplacian operator [74]:

$$\nabla_n^2 \Psi_n = M \Psi_n = V^{-1} L V \Psi_n, \quad (5.2)$$

where  $M$  is the MPD discretized operator defined by

$$V_{i,j} = P_{i-1}(\mu_j) w_j \quad (5.3a)$$

and

$$L_{i,j} = -i(i-1), \quad (5.3b)$$

for  $i, j = 1, \dots, N$ . Here,  $P_i(\mu_j)$  are the Legendre polynomials evaluated at each angle  $\mu_j$  and  $w_j$  are their respective weights.  $M$  is defined as a  $(N \times N)$  operator for a vector of  $N$  angular fluxes  $\Psi(x)$  at spatial location  $x$ .

In summary, if we write the FP equation as

$$\mathcal{H} \frac{\partial \Psi_n}{\partial z}(z) + \Sigma_a \Psi_n(z) - \mathcal{F} \Psi_n(z) = Q_n(z), \quad (5.4)$$

then  $\mathcal{H}$  is  $\text{Diag}(\mu_n)$  for  $n = 1, \dots, N$ ,  $Q(z)$  is a vector of source terms  $Q_n(z)$ , and  $\mathcal{F}$  is represented by  $\frac{\Sigma_{tr}}{2} M$ .

## 5.2 Finite Element Method

We use the linear-discontinuous finite element method to discretize equations in space [29, 75, 76]. We begin with partitioning the spatial domain,  $(z_L, z_R)$ , into a set of contiguous cells:  $(z_{i-\frac{1}{2}}, z_{i+\frac{1}{2}})$ , where  $i = 1, 2, \dots, K$  and  $z_L = z_1$  and  $z_R = z_K$ . We assume a linear-discontinuous representation for the angular flux within each cell, that is

$$\Psi(z) = \Psi_i^L B_i^L(z) + \Psi_i^R B_i^R(z), \quad (5.5)$$

where the linear basis functions are defined as

$$B_i^L(z) = \frac{z_{i+\frac{1}{2}} - z}{\Delta z_i}, \quad (5.6a)$$

$$B_i^R(z) = \frac{z - z_{i-\frac{1}{2}}}{\Delta z_i}, \quad (5.6b)$$

with

$$\Delta z_i = z_{i+\frac{1}{2}} - z_{i-\frac{1}{2}}, \quad (5.7)$$

and the edge fluxes are

$$\Psi_i^L = \Psi_i(z_i^L), \quad (5.8)$$

$$\Psi_i^R = \Psi_i(z_i^R). \quad (5.9)$$

The angular flux at each cell interface is designed to be continuous in the direction of particle flow:

$$\Psi(z_{i+\frac{1}{2}}) = \begin{cases} \Psi_i^R & \text{for } \mu > 0, \\ \Psi_{i+1}^L & \text{for } \mu < 0. \end{cases} \quad (5.10a)$$

The linear discontinuous angular flux for  $\mu > 0$  and  $\mu < 0$  are illustrated in Fig. 5.1 and Fig. 5.2, respectively.

We construct the weighted residual form of Eq. (3.37) by forming two equations. The first equation is formed by multiplying Eq. (3.37) by the linear basis function  $B_i^L(z)$  and integrating over spatial cell  $i$ . The second equation follows the same procedure except the linear basis function  $B_i^R(z)$  is used instead:

$$\int_{z_i^L}^{z_i^R} dz B_i^L(z) \left( \mu_n \frac{\partial \Psi(z, \mu_n)}{\partial z} + \Sigma_t \Psi(z, \mu_n) - \sum_{l=0}^L \frac{2l+1}{2} \Sigma_{s,l} P_l(\mu_n) \phi_l(z) - Q(z, \mu_n) \right) = 0, \quad (5.11)$$

$$\int_{z_i^L}^{z_i^R} dz B_i^R(z) \left( \mu_n \frac{\partial \Psi(z, \mu_n)}{\partial z} + \Sigma_t \Psi(z, \mu_n) - \sum_{l=0}^L \frac{2l+1}{2} \Sigma_{s,l} P_l(\mu_n) \phi_l(z) - Q(z, \mu_n) \right) = 0, \quad (5.12)$$

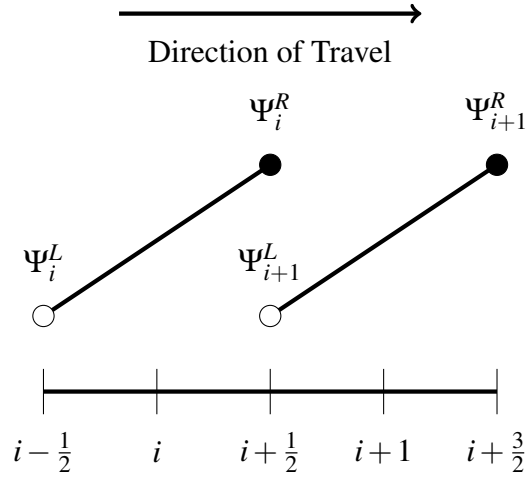


Figure 5.1: Spatial dependence of angular flux for  $\mu > 0$ . The flux at a cell interface is defined by the solution from the previous cell.

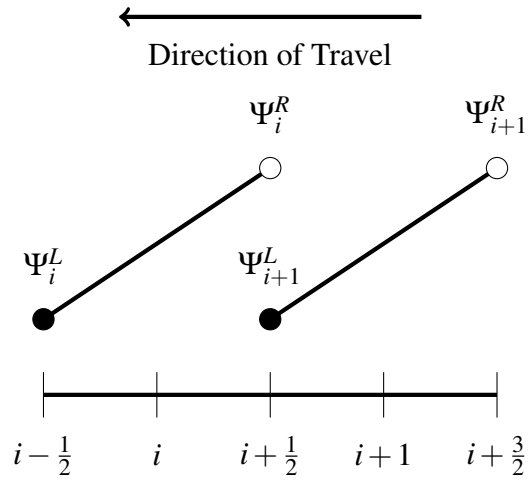


Figure 5.2: Spatial dependence of angular flux for  $\mu < 0$ . Similar to Fig. 5.1, the flux at a cell interface is defined by the solution from the previous cell.



We insert the definition Eq. (5.5) into Eqs. (5.11) and (5.12) and carry out the integration. For both Eq. (5.11) and Eq. (5.12), the direction  $\mu_n$  will determine how the angular flux is updated in each cell. We will have two equations that represent Eq. (5.11), one for  $\mu_n > 0$  and one for  $\mu_n < 0$ . The same will be true for Eq. (5.12). For  $\mu_n > 0$  we have the following equations:

$$\begin{aligned} & \left( \frac{\mu_n}{2} + \frac{\Sigma_t \Delta z_i}{3} \right) \Psi_i^L(\mu_n) + \left( \frac{\mu_n}{2} + \frac{\Sigma_t \Delta z_i}{6} \right) \Psi_i^R(\mu_n) \\ &= \mu_n \Psi_{i-1}^R(\mu_n) + \sum_{l=0}^L \frac{2l+1}{2} \Sigma_{s,l} P_l(\mu_n) \left( \frac{\Delta z_i}{3} \phi_l(z_i^L) + \frac{\Delta z_i}{6} \phi_l(z_i^R) \right) + Q(z_i^L, \mu_n), \end{aligned} \quad (5.13)$$

and

$$\begin{aligned} & \left( -\frac{\mu_n}{2} + \frac{\Sigma_t \Delta z_i}{6} \right) \Psi_i^L(\mu_n) + \left( \frac{\mu_n}{2} + \frac{\Sigma_t \Delta z_i}{3} \right) \Psi_i^R(\mu_n) \\ &= \sum_{l=0}^L \frac{2l+1}{2} \Sigma_{s,l} P_l(\mu_n) \left( \frac{\Delta z_i}{6} \phi_l(z_i^L) + \frac{\Delta z_i}{3} \phi_l(z_i^R) \right) + Q(z_i^R, \mu_n). \end{aligned} \quad (5.14)$$

For clarity, we can rewrite Eqs. (5.13) and (5.14) in matrix form as:

$$\begin{aligned} & \begin{bmatrix} \frac{\mu_n}{2} + \frac{\Sigma_t \Delta z_i}{3} & \frac{\mu_n}{2} + \frac{\Sigma_t \Delta z_i}{6} \\ -\frac{\mu_n}{2} + \frac{\Sigma_t \Delta z_i}{6} & \frac{\mu_n}{2} + \frac{\Sigma_t \Delta z_i}{3} \end{bmatrix} \begin{bmatrix} \Psi_i^L(\mu_n) \\ \Psi_i^R(\mu_n) \end{bmatrix} = \begin{bmatrix} \mu_n \Psi_{i-1}^R(\mu_n) \\ 0 \end{bmatrix} \\ & + \sum_{l=0}^L \frac{2l+1}{2} \Sigma_{s,l} P_l(\mu_n) \begin{bmatrix} \frac{\Delta z_i}{3} & \frac{\Delta z_i}{6} \\ \frac{\Delta z_i}{6} & \frac{\Delta z_i}{3} \end{bmatrix} \begin{bmatrix} \phi_l(z_i^L) \\ \phi_l(z_i^R) \end{bmatrix} + \begin{bmatrix} Q(z_i^L, \mu_n) \\ Q(z_i^R, \mu_n) \end{bmatrix}. \end{aligned} \quad (5.15)$$

For  $\mu_n > 0$ , we sweep from left to right. We update  $\Psi_{i-1}^R(\mu_n)$  from the previous cell to the left, and then solve for  $\Psi_i^L(\mu_n)$  and  $\Psi_i^R(\mu_n)$  in the current cell. This process is repeated until we reach the right edge of the slab  $z_K$ .

For  $\mu_n < 0$  we get

$$\begin{aligned} & \left( -\frac{\mu_n}{2} + \frac{\Sigma_t \Delta z_i}{3} \right) \Psi_i^L(\mu_n) + \left( \frac{\mu_n}{2} + \frac{\Sigma_t \Delta z_i}{6} \right) \Psi_i^R(\mu_n) \\ &= \sum_{l=0}^L \frac{2l+1}{2} \Sigma_{s,l} P_l(\mu_n) \left( \frac{\Delta z_i}{3} \phi_l(z_i^L) + \frac{\Delta z_i}{6} \phi_l(z_i^R) \right) + Q(z_i^L, \mu_n), \end{aligned} \quad (5.16)$$

and

$$\begin{aligned} & \left( -\frac{\mu_n}{2} + \frac{\Sigma_t \Delta z_i}{6} \right) \Psi_i^L(\mu_n) + \left( -\frac{\mu_n}{2} + \frac{\Sigma_t \Delta z_i}{3} \right) \Psi_i^R(\mu_n) \\ &= -\mu_n \Psi_{i+1}^L(\mu_n) + \sum_{l=0}^L \frac{2l+1}{2} \Sigma_{s,l} P_l(\mu_n) \left( \frac{\Delta z_i}{6} \phi_l(z_i^L) + \frac{\Delta z_i}{3} \phi_l(z_i^R) \right) + Q(z_i^R, \mu_n). \end{aligned} \quad (5.17)$$

Rewriting Eqs. (5.16) and (5.17) in matrix form gives

$$\begin{aligned} & \begin{bmatrix} -\frac{\mu_n}{2} + \frac{\Sigma_t \Delta z_i}{3} & \frac{\mu_n}{2} + \frac{\Sigma_t \Delta z_i}{6} \\ -\frac{\mu_n}{2} + \frac{\Sigma_t \Delta z_i}{6} & -\frac{\mu_n}{2} + \frac{\Sigma_t \Delta z_i}{3} \end{bmatrix} \begin{bmatrix} \Psi_i^L(\mu_n) \\ \Psi_i^R(\mu_n) \end{bmatrix} = \begin{bmatrix} 0 \\ -\mu_n \Psi_{i+1}^L(\mu_n) \end{bmatrix} \\ & + \sum_{l=0}^L \frac{2l+1}{2} \Sigma_{s,l} P_l(\mu_n) \begin{bmatrix} \frac{\Delta z_i}{3} & \frac{\Delta z_i}{6} \\ \frac{\Delta z_i}{6} & \frac{\Delta z_i}{3} \end{bmatrix} \begin{bmatrix} \phi_l(z_i^L) \\ \phi_l(z_i^R) \end{bmatrix} + \begin{bmatrix} Q(z_i^L, \mu_n) \\ Q(z_i^R, \mu_n) \end{bmatrix}. \end{aligned} \quad (5.18)$$

For  $\mu_n < 0$ , we sweep from right to left. We update  $\Psi_{i+1}^L(\mu_n)$  from the previous cell to the right, and then solve for  $\Psi_i^L(\mu_n)$  and  $\Psi_i^R(\mu_n)$  in the current cell. This process is repeated until we reach the left edge of the slab  $z_1$ .

The weighted residual form of the Fokker-Planck equation, Eq. (5.1), is formed by following the same steps as above. We multiply Eq. (5.1) by the basis functions and integrate over spatial cell  $i$ :

$$\int_{z_i^L}^{z_i^R} dz B_i^L(z) \left( \mu_n \frac{\partial \Psi(z, \mu_n)}{\partial z} + \Sigma_a \Psi(z, \mu_n) - \frac{\Sigma_{tr}}{2} \nabla_n^2 \Psi(z, \mu_n) - Q(z, \mu_n) \right) = 0, \quad (5.19)$$

$$\int_{z_i^L}^{z_i^R} dz B_i^R(z) \left( \mu_n \frac{\partial \Psi(z, \mu_n)}{\partial z} + \Sigma_a \Psi(z, \mu_n) - \frac{\Sigma_{tr}}{2} \nabla_n^2 \Psi(z, \mu_n) - Q(z, \mu_n) \right) = 0, \quad (5.20)$$

We carry out the integration and follow the same steps as above to get the following matrix equations. For  $\mu_n > 0$  we have

$$\begin{aligned} & \begin{bmatrix} \frac{\mu_n}{2} + \frac{\Sigma_a \Delta z_i}{3} - \frac{\Sigma_{tr}}{6} \nabla_n^2 & \frac{\mu_n}{2} + \frac{\Sigma_t \Delta z_i}{6} - \frac{\Sigma_{tr}}{12} \nabla_n^2 \\ -\frac{\mu_n}{2} + \frac{\Sigma_a \Delta z_i}{6} - \frac{\Sigma_{tr}}{12} \nabla_n^2 & \frac{\mu_n}{2} + \frac{\Sigma_t \Delta z_i}{3} - \frac{\Sigma_{tr}}{6} \nabla_n^2 \end{bmatrix} \begin{bmatrix} \Psi_i^L(\mu_n) \\ \Psi_i^R(\mu_n) \end{bmatrix} = \\ & \begin{bmatrix} \mu_n \Psi_{i-1}^R(\mu_n) \\ 0 \end{bmatrix} + \begin{bmatrix} Q(z_i^L, \mu_n) \\ Q(z_i^R, \mu_n) \end{bmatrix}, \end{aligned} \quad (5.21)$$

and for  $\mu_n < 0$  we have

$$\begin{aligned} & \begin{bmatrix} -\frac{\mu_n}{2} + \frac{\Sigma_a \Delta z_i}{3} - \frac{\Sigma_{tr}}{6} \nabla_n^2 & \frac{\mu_n}{2} + \frac{\Sigma_t \Delta z_i}{6} - \frac{\Sigma_{tr}}{12} \nabla_n^2 \\ -\frac{\mu_n}{2} + \frac{\Sigma_a \Delta z_i}{6} - \frac{\Sigma_{tr}}{12} \nabla_n^2 & -\frac{\mu_n}{2} + \frac{\Sigma_t \Delta z_i}{3} - \frac{\Sigma_{tr}}{6} \nabla_n^2 \end{bmatrix} \begin{bmatrix} \Psi_i^L(\mu_n) \\ \Psi_i^R(\mu_n) \end{bmatrix} = \\ & \begin{bmatrix} 0 \\ -\mu_n \Psi_{i+1}^L(\mu_n) \end{bmatrix} + \begin{bmatrix} Q(z_i^L, \mu_n) \\ Q(z_i^R, \mu_n) \end{bmatrix}, \end{aligned} \quad (5.22)$$

We follow the same sweeping procedure used for Eqs. (5.15) and (5.18) to solve Eqs. (5.21) and (5.22).

## Chapter 6: Numerical and Experimental Validation

In this chapter, we validate the MFPA method through comparison with FPSA, DSA, and non accelerated transport. We also apply angular discrete Fourier Analysis to MFPA and compare with FPSA and source iteration.

All numerical experiments were performed using MATLAB. Runtime was tracked using the tic-toc functionality [77], with only the solver runtime being taken into consideration in the comparisons. A 2017 MacBook Pro with a 2.8 GHz Quad-Core Intel Core i7 and 16 GB of RAM was used for all simulations.

Two problems are tested against MFPA, FPSA, DSA, and non accelerated transport. Problem set 1 has vacuum boundaries and a homogeneous, isotropic source  $Q$  for  $0 < z < Z$ . Problem set 2 has no internal source and an incoming beam at the left boundary at the highest order angle. The source and boundary conditions used are shown in Table 6.1. A delta function is used to represent a beam flux at the highest order angle. For both problems

	Problem set 1	Problem set 2
$Q(z)$	0.5	0
$\Psi_L$	0	$\delta(\mu - \mu_N)$
$\Psi_R$	0	0

Table 6.1: Problem Parameters

sets, homogeneous and heterogeneous media were used to test the accuracy of MFPA using interface conditions. Homogeneous media refers to a medium that is the same throughout. A heterogeneous medium will have at least one interface where there are different cross-sections on each side of the interface. The results obtained with MFPA using Picard iteration are compared with those obtained using non accelerated transport with GMRES, DSA, and FPSA with the moment preserving discretization scheme.

## 6.1 Scattering Kernels

To run numerical experiments the scattering moments used in Eq. (3.37) need to be defined. The scattering moments are generated through a scattering kernel and dictate the physics of the scattering. The performance of Fokker-Planck based acceleration methods rely on scattering kernels having a valid Fokker-Planck limit. In this document, we test MFPA using the Screened Rutherford kernel (SRK), the Exponential kernel (EK), and the Henyey-Greenstein kernel (HGK). The kernels are discussed in detail in this section. Each kernel was used to generate three sets of scattering moments for numerical experiments.

### 6.1.1 Screened Rutherford Kernel

The Screened Rutherford Kernel [78] is a widely used scattering kernel for modeling scattering behavior of electrons [28, 55, 79]. The kernel depends on the screening parameter  $\eta$  [55, 78], such that

$$\Sigma_{s,l}^{SRK} = \Sigma_s \int_{-1}^1 d\mu P_l(\mu) \frac{\eta(\eta+1)}{(1+2\eta-\mu)^2}. \quad (6.1)$$

The SRK has a valid FP limit as  $\eta$  approaches 0 [28, 29]. Three different values of  $\eta = 10^{-5}, 10^{-6}, 10^{-7}$  were used to generate the scattering kernels shown in Table 6.2.

	$\eta = 10^{-7}$		$\eta = 10^{-6}$		$\eta = 10^{-5}$
$\Sigma_{s,0}$	0.5	$\Sigma_{s,0}$	0.5	$\Sigma_{s,0}$	0.5
$\Sigma_{s,1}$	0.4999984881902637	$\Sigma_{s,1}$	0.4999871844746265	$\Sigma_{s,1}$	0.4998948694940573
$\Sigma_{s,2}$	0.4999957645698841	$\Sigma_{s,2}$	0.4999645533469864	$\Sigma_{s,2}$	0.4997146021743414
$\Sigma_{s,3}$	0.4999919291371969	$\Sigma_{s,3}$	0.499933106478293	$\Sigma_{s,3}$	0.4994691869248763
$\Sigma_{s,4}$	0.4999870485565143	$\Sigma_{s,4}$	0.4998935103411987	$\Sigma_{s,4}$	0.4991652751543127
$\Sigma_{s,5}$	0.4999811728248328	$\Sigma_{s,5}$	0.4998462646906273	$\Sigma_{s,5}$	0.4988078478784902
$\Sigma_{s,6}$	0.4999743419385311	$\Sigma_{s,6}$	0.4997917692335063	$\Sigma_{s,6}$	0.4984008826928098
$\Sigma_{s,7}$	0.4999665892267273	$\Sigma_{s,7}$	0.4997303569645318	$\Sigma_{s,7}$	0.497947687347766
$\Sigma_{s,8}$	0.4999579432560612	$\Sigma_{s,8}$	0.4996623132158051	$\Sigma_{s,8}$	0.4974510904257452
$\Sigma_{s,9}$	0.4999484290211878	$\Sigma_{s,9}$	0.4995878875633187	$\Sigma_{s,9}$	0.4969135605598148
$\Sigma_{s,10}$	0.4999380687384428	$\Sigma_{s,10}$	0.4995073017649702	$\Sigma_{s,10}$	0.4963372859480047
$\Sigma_{s,11}$	0.4999268824014123	$\Sigma_{s,11}$	0.4994207553174542	$\Sigma_{s,11}$	0.4957242300410234
$\Sigma_{s,12}$	0.4999148881849843	$\Sigma_{s,12}$	0.4993284294978682	$\Sigma_{s,12}$	0.4950761720648456
$\Sigma_{s,13}$	0.4999021027483907	$\Sigma_{s,13}$	0.4992304903951062	$\Sigma_{s,13}$	0.4943947374311556
$\Sigma_{s,14}$	0.4998885414683172	$\Sigma_{s,14}$	0.499127091241861	$\Sigma_{s,14}$	0.4936814211455058
$\Sigma_{s,15}$	0.4998742186220628	$\Sigma_{s,15}$	0.4990183742470478	$\Sigma_{s,15}$	0.4929376062126142

Table 6.2: SRK cross-section Moments

### 6.1.2 Exponential Kernel

The exponential kernel [80] is a test kernel made for problems that have a valid Fokker-Planck limit [28, 79, 81]. The zero<sup>th</sup> moment,  $\Sigma_{s,0}^{EK}$ , is chosen arbitrarily; we define  $\Sigma_{s,0}^{EK}$  as the same zero<sup>th</sup> moment from the SRK. The  $\Delta$  parameter determines the kernel: the first and second moments are given by

$$\Sigma_{s,1}^{EK} = \Sigma_{s,0}^{EK} (1 - \Delta), \quad (6.2a)$$

$$\Sigma_{s,2}^{EK} = \Sigma_{s,0}^{EK} (1 - 3\Delta + 3\Delta^2), \quad (6.2b)$$

and the relationship for  $l \geq 3$  is

$$\Sigma_{s,l+1}^{EK} = \Sigma_{s,l-1}^{EK} - \Delta(2l+1)\Sigma_{s,l}^{EK}. \quad (6.2c)$$

As  $\Delta$  is reduced, the scattering kernel becomes more forward-peaked.

The EK has a valid FP limit as  $\Delta$  approaches 0 [28, 29]. Three different values of  $\Delta = 10^{-5}, 10^{-6}, 10^{-7}$  were used to generate the scattering kernels shown in Table 6.3.

	$\Delta = 10^{-7}$		$\Delta = 10^{-6}$		$\Delta = 10^{-5}$
$\Sigma_{s,0}$	0.5	$\Sigma_{s,0}$	0.5	$\Sigma_{s,0}$	0.5
$\Sigma_{s,1}$	0.49999995	$\Sigma_{s,1}$	0.4999995	$\Sigma_{s,1}$	0.499995
$\Sigma_{s,2}$	0.499999850000015	$\Sigma_{s,2}$	0.49999850000015	$\Sigma_{s,2}$	0.499985000015
$\Sigma_{s,3}$	0.499999650000035	$\Sigma_{s,3}$	0.49999650000035	$\Sigma_{s,3}$	0.499965000035
$\Sigma_{s,4}$	0.499999500000135	$\Sigma_{s,4}$	0.4999950000135	$\Sigma_{s,4}$	0.4999500013499865
$\Sigma_{s,5}$	0.4999993000004	$\Sigma_{s,5}$	0.49999300004	$\Sigma_{s,5}$	0.4999300039999615
$\Sigma_{s,6}$	0.499999000000685	$\Sigma_{s,6}$	0.4999900000684998	$\Sigma_{s,6}$	0.4999000068498245
$\Sigma_{s,7}$	0.499998750001185	$\Sigma_{s,7}$	0.4999875001184994	$\Sigma_{s,7}$	0.4998750118493865
$\Sigma_{s,8}$	0.4999984500021	$\Sigma_{s,8}$	0.4999845002099988	$\Sigma_{s,8}$	0.499845020998797
$\Sigma_{s,9}$	0.49999805000306	$\Sigma_{s,9}$	0.4999805003059975	$\Sigma_{s,9}$	0.4998050305975731
$\Sigma_{s,10}$	0.49999770000444	$\Sigma_{s,10}$	0.499977000443995	$\Sigma_{s,10}$	0.4997700443949768
$\Sigma_{s,11}$	0.499997300006585	$\Sigma_{s,11}$	0.4999730006584918	$\Sigma_{s,11}$	0.4997300658417596
$\Sigma_{s,12}$	0.49999680000881	$\Sigma_{s,12}$	0.4999680008809864	$\Sigma_{s,12}$	0.4996800880864744
$\Sigma_{s,13}$	0.49999635001173	$\Sigma_{s,13}$	0.4999635011729772	$\Sigma_{s,13}$	0.4996351172771995
$\Sigma_{s,14}$	0.499995850015865	$\Sigma_{s,14}$	0.4999585015864663	$\Sigma_{s,14}$	0.4995851586162145
$\Sigma_{s,15}$	0.499995250020125	$\Sigma_{s,15}$	0.49995250201245	$\Sigma_{s,15}$	0.4995252012001185

Table 6.3: EK cross-section Moments

### 6.1.3 Henyey-Greenstein Kernel

The Henyey-Greenstein Kernel [40] is most commonly used in light transport in clouds.

It relies on the anisotropy factor  $g$ , such that

$$\Sigma_{s,l}^{HGK} = \Sigma_s g^l. \quad (6.3)$$

As  $g$  goes from zero to unity, the scattering shifts from isotropic to highly anisotropic. The HGK does *not* have a valid FP limit [28, 29], so FPSA and MFPA should not perform as well when compared to SRK or EK. The three kernels generated from  $g = 0.9, 0.95, 0.99$  are shown in Table 6.4.

	$g = 0.99$		$g = 0.95$		$g = 0.9$
$\Sigma_{s,0}$	1	$\Sigma_{s,0}$	1	$\Sigma_{s,0}$	1
$\Sigma_{s,1}$	0.99	$\Sigma_{s,1}$	0.95	$\Sigma_{s,1}$	0.9
$\Sigma_{s,2}$	0.9801	$\Sigma_{s,2}$	0.9025	$\Sigma_{s,2}$	0.8100000000000001
$\Sigma_{s,3}$	0.970299	$\Sigma_{s,3}$	0.857375	$\Sigma_{s,3}$	0.729
$\Sigma_{s,4}$	0.9605960099999999	$\Sigma_{s,4}$	0.81450625	$\Sigma_{s,4}$	0.6561
$\Sigma_{s,5}$	0.9509900499	$\Sigma_{s,5}$	0.7737809375	$\Sigma_{s,5}$	0.59049
$\Sigma_{s,6}$	0.9414801494	$\Sigma_{s,6}$	0.7350918906	$\Sigma_{s,6}$	0.5314410000000001
$\Sigma_{s,7}$	0.9320653479	$\Sigma_{s,7}$	0.6983372960999999	$\Sigma_{s,7}$	0.4782969
$\Sigma_{s,8}$	0.9227446944	$\Sigma_{s,8}$	0.6634204312999999	$\Sigma_{s,8}$	0.43046721
$\Sigma_{s,9}$	0.9135172475	$\Sigma_{s,9}$	0.6302494097	$\Sigma_{s,9}$	0.387420489
$\Sigma_{s,10}$	0.904382075	$\Sigma_{s,10}$	0.5987369392	$\Sigma_{s,10}$	0.3486784401
$\Sigma_{s,11}$	0.8953382543	$\Sigma_{s,11}$	0.5688000922999999	$\Sigma_{s,11}$	0.3138105961
$\Sigma_{s,12}$	0.8863848717	$\Sigma_{s,12}$	0.5403600877	$\Sigma_{s,12}$	0.2824295365
$\Sigma_{s,13}$	0.877521023	$\Sigma_{s,13}$	0.5133420833	$\Sigma_{s,13}$	0.2541865828
$\Sigma_{s,14}$	0.8687458128	$\Sigma_{s,14}$	0.4876749791	$\Sigma_{s,14}$	0.2287679245
$\Sigma_{s,15}$	0.8600583546	$\Sigma_{s,15}$	0.4632912302	$\Sigma_{s,15}$	0.2058911321

Table 6.4: HGK cross-section Moments

## 6.2 Convergence Criterion

False convergence has been shown to result in inaccurate solutions for slowly converging problems when popular convergence criteria such as  $L_\infty$  [1]. To work around this issue, the convergence criterion is modified to use information about the current and previous iteration:

$$\frac{\|\phi_0^m(z) - \phi_0^{m-1}(z)\|_2}{1 - \frac{\|\phi_0^{m+1}(z) - \phi_0^m(z)\|_2}{\|\phi_0^m(z) - \phi_0^{m-1}(z)\|_2}} < 10^{-8}. \quad (6.4)$$

Furthermore, results are given for non-accelerated GMRES along with MFPA and FPSA using GMRES and compared with the results from MFPA using Picard iteration. The solve time for GMRES has been shown to be quicker than synthetic or picard acceleration [48]; but the setup time for a GMRES solve tends to be much larger than setup time for synthetic or picard iteration. MATLAB has a GMRES function [77] with built-in convergence criterion. The convergence criterion used for Picard iteration was chosen to

match MATLAB's GMRES function such that:

$$\frac{\|Q - (\mathcal{L} - S)\Psi_{HO}\|_2}{\|Q\|_2} < 10^{-8}. \quad (6.5)$$

### 6.3 Choice of Consistency Term

Three different consistency terms were introduced in Section 4.2. The disadvantages of using the nonlinear consistency terms were briefly discussed. To further illustrate the difference in performance between the linear and nonlinear consistency terms, we test MFPA with all three consistency terms against problem sets 1 and 2 using the parameters shown in Table 6.1. We setup a homogeneous slab using 100 spatial cells, slab width  $Z = 100$  mean free paths,  $\Sigma_a = 0$ ,  $\Sigma_t = \Sigma_{s,0}$ ,  $L = 15$ , and  $N = 16$ . Problems 1 and 2 were tested for the SRK with  $\eta = 10^{-7}$ . The false convergence criteria from Eq. (6.4) was used.

Figure 6.1 shows that for problem 1, MFPA converges to the transport solution using any of the consistency terms. The unaccelerated transport solution was converged using GMRES. Table 6.5 shows the runtimes and iterations for MFPA with each consistency term tested for problem 1. We see that the linear consistency term outperforms the nonlinear consistency terms in time, even though MFPA with the  $D$  consistency term converges in fewer iterations. This was expected because for the nonlinear consistency terms, the LO iteration matrix needs to be modified after each transport sweep. For the linear consistency term, the LO iteration matrix remains the same because the consistency term is added to the source term and not to the iteration matrix. Modifying the LO iteration matrix at each sweep increases the numerical cost and time.

Figure 6.2 shows that for problem 2, MFPA converges to the GMRES transport solution when using  $\hat{D}_f$  and  $\bar{D}$ . MFPA does not converge when using  $D$ , due to zero angular flux existing in the beam problem. Table 6.6 shows the runtimes and iterations for MFPA with



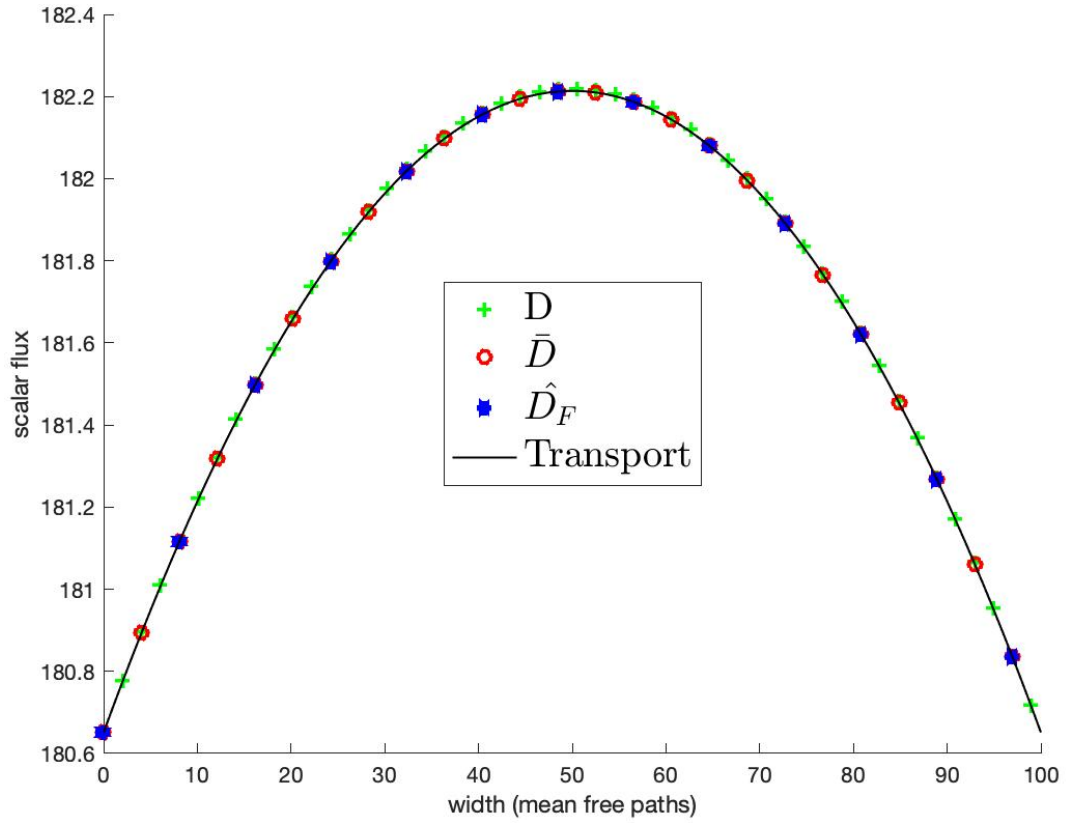


Figure 6.1: Problem 1 Results for SRK with  $\eta = 10^{-7}$  using Different Consistency Terms

the linear and nonlinear consistency terms tested for problem 2. We see that the linear consistency term still outperforms the nonlinear consistency term for problem 2.

In the coming sections, MFPA using a linear consistency term is compared against FPSA, source iteration, GMRES, and DSA. Linear MFPA outperformed MFPA using nonlinear consistency terms for both problem sets. Linear MFPA still allows for multiphysics coupling due to the way that it is setup, and has been shown to be the superior choice when compared to the nonlinear consistency terms.

Parameter	Consistency Term	Runtime (s)	Iterations
$\eta = 10^{-7}$	$D$ -nonlinear	6.55	4
	$\bar{D}$ -nonlinear	12.9	8
	$\hat{D}_f$ -linear	0.110	7
	Transport	12.5	536

Table 6.5: Runtime and Iteration Counts for Problem 1 with SRK using MFPA with Different Consistency Terms

Parameter	Consistency Term	Runtime (s)	Iterations
$\eta = 10^{-7}$	$\bar{D}$ -nonlinear	11.5	7
	$\hat{D}_f$ -linear	0.111	7
	Transport	5.13	450

Table 6.6: Runtime and Iteration Counts for Problem 2 with SRK using MFPA with Different Consistency Terms

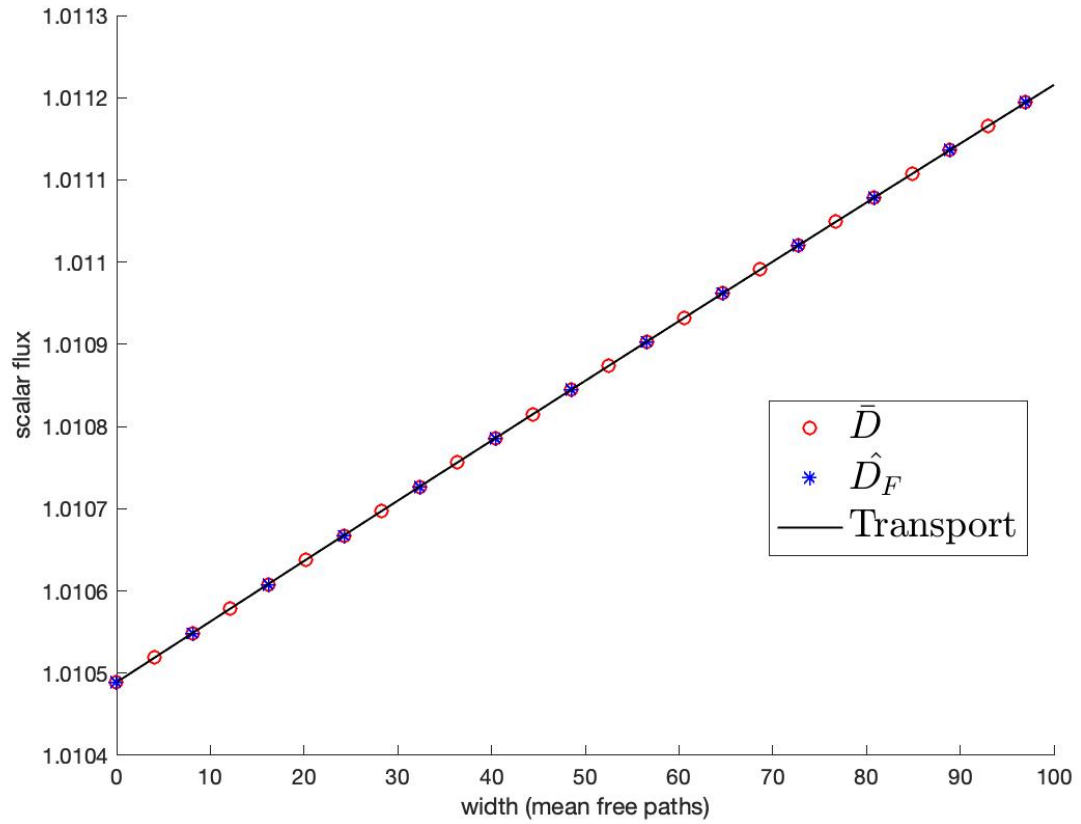


Figure 6.2: Problem 2 Results for SRK with  $\eta = 10^{-7}$  using MFPA with Different Consistency Terms

## 6.4 Angularly Discrete Fourier Analysis

In this section we analyze linear MFPA using angular-discrete Fourier analysis. Moment preserving discretization was used to discretize the Fokker-Planck operator, as it preserves up to  $N$  moments of angular flux. The iteration matrix of MFPA is determined through angular-discrete Fourier analysis. The scattering kernels introduced in Section 6.1 are used. The theoretical spectral radius is deciphered and compared against the numerical spectral radius for each scattering kernel. Finally a comparison of the theoretical spectral radii for source iteration, FPSA, and MFPA is given.

### 6.4.1 Theory

Our goal is to theoretically determine how efficient the proposed MFPA method is through the spectral radius of the iteration matrix. This analysis closely follows the work done in [28].

We begin with rewriting Eqs. (4.5) using source iteration, as

$$\mu \frac{\partial \Psi_{HO}^{k+1}}{\partial x} + \Sigma_t \Psi_{HO}^{k+1} = \sum_{l=0}^L \frac{(2l+1)}{2} P_l \Sigma_{s,l} \phi_{l,LO}^{k+1} + Q, \quad (6.6a)$$

$$\begin{aligned} \mu \frac{\partial \Psi_{LO}^{k+1}}{\partial x} + \Sigma_a \Psi_{LO}^{k+1} - \frac{\Sigma_{tr}}{2} \frac{\partial}{\partial \mu} (1 - \mu^2) \frac{\partial \Psi_{LO}^{k+1}}{\partial \mu} = \\ Q + \sum_{l=0}^L \frac{(2l+1)}{2} P_l \Sigma_{s,l} \phi_{l,HO}^k - \frac{\Sigma_{tr}}{2} \frac{\partial}{\partial \mu} (1 - \mu^2) \frac{\partial \Psi_{HO}^k}{\partial \mu} - \Sigma_{s,0} \Psi_{HO}^k. \end{aligned} \quad (6.6b)$$

Subtracting the exact equations (4.5a) and (4.5b) from Eqs. (6.6) returns the error equations

$$\mu \frac{\partial \epsilon_{HO}^{k+1}}{\partial x} + \Sigma_t \epsilon_{HO}^{k+1} = \sum_{l=0}^L \frac{(2l+1)}{2} P_l \Sigma_{s,l} \epsilon_{LO}^{k+1}, \quad (6.7a)$$

$$\begin{aligned} \mu \frac{\partial \epsilon_{LO}^{k+1}}{\partial x} + \Sigma_a \epsilon_{LO}^{k+1} - \frac{\Sigma_{tr}}{2} \frac{\partial}{\partial \mu} (1 - \mu^2) \frac{\partial \epsilon_{LO}^{k+1}}{\partial \mu} = \\ \sum_{l=0}^L \frac{(2l+1)}{2} P_l \Sigma_{s,l} \epsilon_{HO}^k - \frac{\Sigma_{tr}}{2} \frac{\partial}{\partial \mu} (1 - \mu^2) \frac{\partial \epsilon_{HO}^k}{\partial \mu} - \Sigma_{s,0} \epsilon_{HO}^k, \end{aligned} \quad (6.7b)$$

where the error in the HO and LO angular flux are defined as

$$\hat{\epsilon}_{HO}^{k+1} = \Psi_{HO}^{k+1} - \Psi_{HO}, \quad (6.8a)$$

$$\hat{\epsilon}_{HO}^k = \Psi_{HO}^k - \Psi_{HO}, \quad (6.8b)$$

$$\hat{\epsilon}_{LO}^{k+1} = \Psi_{LO}^{k+1} - \Psi_{LO}. \quad (6.8c)$$

To perform Fourier analysis, we introduce the following Fourier mode ansatz for the HO and LO errors:

$$\hat{\epsilon}_{HO}^{k+1} = \epsilon_{HO}^{k+1}(\mu) e^{i \Sigma_t \lambda x}, \quad (6.9a)$$

$$\hat{\epsilon}_{HO}^k = \epsilon_{HO}^k(\mu) e^{i \Sigma_t \lambda x}, \quad (6.9b)$$

$$\hat{\epsilon}_{LO}^{k+1} = \epsilon_{LO}^{k+1}(\mu) e^{i \Sigma_t \lambda x}. \quad (6.9c)$$

Substituting Eqs. (6.9a) and (6.9c) into Eq. (6.7a) and simplifying, leads to

$$(\Sigma_t + i \Sigma_t \lambda \mu) \epsilon_{HO}^{k+1} = \sum_{l=0}^L \frac{(2l+1)}{2} P_l \Sigma_{s,l} \epsilon_{LO}^{k+1} \quad (6.10)$$

Next, we take the  $n^{\text{th}}$  Legendre moment of Eq. (6.10) and use the orthogonality property of Legendre polynomials, which allows us to write

$$\int_{-1}^1 d\mu P_l(\mu) (\Sigma_t + i \Sigma_t \lambda \mu) \epsilon_{HO}^{k+1} = \int_{-1}^1 d\mu P_l(\mu) \Sigma_{s,l} \epsilon_{LO}^{k+1}, \quad (6.11)$$

where  $\epsilon_{l,LO}^{k+1}$  represents the LO flux moment error. Here, the flux moment error is defined as

$$\epsilon_l^k = \int_{-1}^1 d\mu P_l(\mu) \epsilon^k = \sum_{n=1}^N w_n P_l(\mu_n) \epsilon^k. \quad (6.12)$$

We can now rewrite the integrals as weighted sums:

$$\underbrace{\sum_{n=1}^N P_l(\mu_n) w_n (\Sigma_t + i \Sigma_t \lambda \mu_n)}_Y \epsilon_{HO}^{k+1} = \underbrace{\sum_{n=1}^N P_l(\mu_n) w_n \Sigma_{s,l}}_Z \epsilon_{LO}^{k+1}. \quad (6.13)$$

Inverting the  $Y$  operator leads to the HO matrix equation

$$\epsilon_{HO}^{k+1} = \underbrace{Y^{-1} Z}_{\hat{A}} \epsilon_{LO}^{k+1}. \quad (6.14)$$

Here,  $\hat{A}$  is part of the MFPA iteration matrix.

Similarly, substituting Eqs. (6.9b) and (6.9c) into Eq. (6.7b) and simplifying returns

$$\begin{aligned} & \left( i \Sigma_t \lambda \mu + \Sigma_a - \frac{\Sigma_{tr}}{2} \frac{\partial}{\partial \mu} (1 - \mu^2) \frac{\partial}{\partial \mu} \right) \epsilon_{LO}^{k+1} = \\ & \left( \sum_{l=0}^L \frac{(2l+1)}{2} P_l \Sigma_{s,l} - \frac{\Sigma_{tr}}{2} \frac{\partial}{\partial \mu} (1 - \mu^2) \frac{\partial}{\partial \mu} - \Sigma_{s,0} \right) \epsilon_{HO}^k. \end{aligned} \quad (6.15)$$

Now, we operate on Eq. (6.15) by  $\int_{-1}^1 d\mu P_l(\mu)(\cdot)$ , rewrite the integrals as weighted sums, and use moment preserving discretization (MPD) [74] for the Fokker-Planck in-scattering term  $\frac{\partial}{\partial \mu} (1 - \mu^2) \frac{\partial}{\partial \mu}$ . This yields the LO matrix equation

$$\begin{aligned} & \underbrace{\sum_{n=1}^N P_l(\mu_n) w_n \left( i \Sigma_t \lambda \mu + \Sigma_a + \frac{\Sigma_{tr}}{2} l(l+1) \right)}_{\hat{B}} \epsilon_{LO}^{k+1} = \\ & \underbrace{\sum_{n=1}^N P_l(\mu_n) w_n \left( \Sigma_{s,l} - \Sigma_{s,0} - \frac{\Sigma_{tr}}{2} l(l+1) \right)}_{\hat{C}} \epsilon_{HO}^k. \end{aligned} \quad (6.16)$$

Finally, we combine Eqs. (6.14) and (6.16) to obtain the final matrix equation

$$\epsilon_{HO}^{k+1} = \hat{A} \hat{B}^{-1} \hat{C} \epsilon_{HO}^k, \quad (6.17)$$

where  $\hat{A} \hat{B}^{-1} \hat{C}$  is the iteration matrix, such that its spectral radius determines the convergence rate of MFPA with MPD.

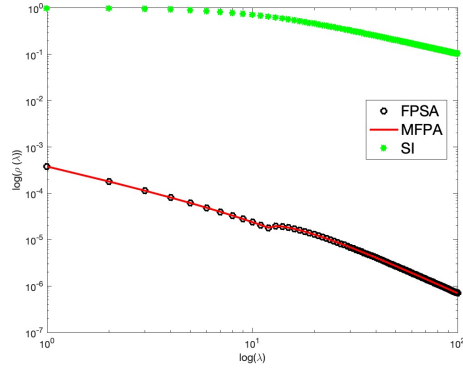
### 6.4.2 Spectral Radii Evaluations

Next, we test the results of this analysis against our numerical results. The theoretical spectral radius ( $\rho_{th}$ ) was tested using  $\Sigma_a = 0.0001\Sigma_{s,0}$ ,  $L = 15$ , and  $N = 16$ . The numerical spectral radius ( $\rho_{nu}$ ) was tested for a homogeneous slab with vacuum boundaries and an isotropic source  $Q = 0.5$  for  $0 < x < X$ . We used 200 spatial cells,  $X = 400$ ,  $L = 15$ ,  $N = 16$ , and  $\Sigma_a = 0.0001\Sigma_{s,0}$ . The Euclidean norm with a tolerance of  $10^{-10}$  was used for convergence. Table 6.7 shows the results for  $\rho_{th}$  and  $\rho_{nu}$ . We observe that the numerical

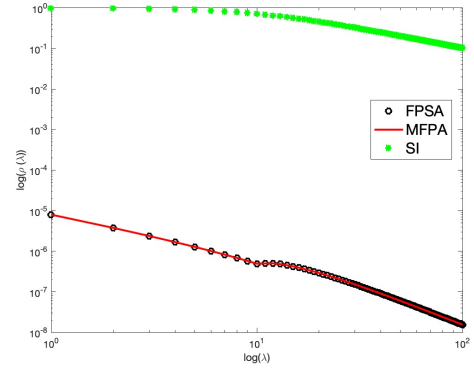
Kernel	Parameter	$\rho_{th}$	$\rho_{nu}$
SRK	$\eta = 10^{-7}$	0.298	0.299
EK	$\Delta = 10^{-7}$	0.114	0.110
HGK	$g = 0.99$	0.760	0.759

Table 6.7: Theoretical Spectral Radius Results for MFPA

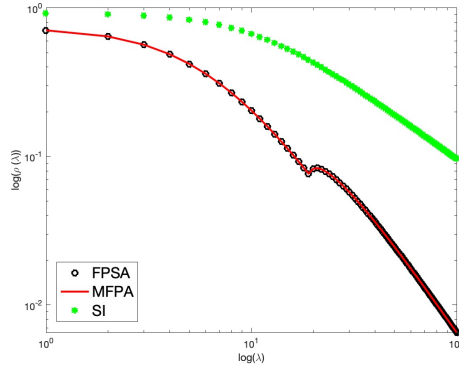
and theoretical spectral radii are in close agreement for all kernels. We also compare the MFPA theoretical spectral radius for each kernel with the theoretical spectral radius of source iteration and FPSA, as shown in Fig. 6.3. We see that the spectral radii of MFPA and FPSA are very close, which is expected due to the equivalency of the methods. Both MFPA and FPSA have significantly smaller spectral radii compared to source iteration.



(a)  $\rho_{th}$  for SRK with  $\eta = 10^{-7}$



(b)  $\rho_{th}$  for EK with  $\Delta = 10^{-7}$



(c)  $\rho_{th}$  for HGK with  $g = 0.99$

Figure 6.3: Results of  $\rho_{th}$  for SRK, EK, and HGK

## 6.5 Homogeneous Slab Results

All homogeneous slab problems were simulated using 200 spatial cells, slab width  $Z = 400$ ,  $\Sigma_a = 0$ ,  $\Sigma_t = \Sigma_{s,0}$ ,  $L = 15$ , and  $N = 16$ . The boundary and source conditions for problems 1 and 2 are shown in Table 6.1. All kernels described in Section 6.1 were used.

### 6.5.1 Problem Set 1

Problem 1 was tested for the SRK, EK, and HGK. The results found are shown below.



## SRK Results

The solution for problem 1 with SRK with  $\eta = 10^{-7}$  is shown in Fig. 6.4. FPFA, and

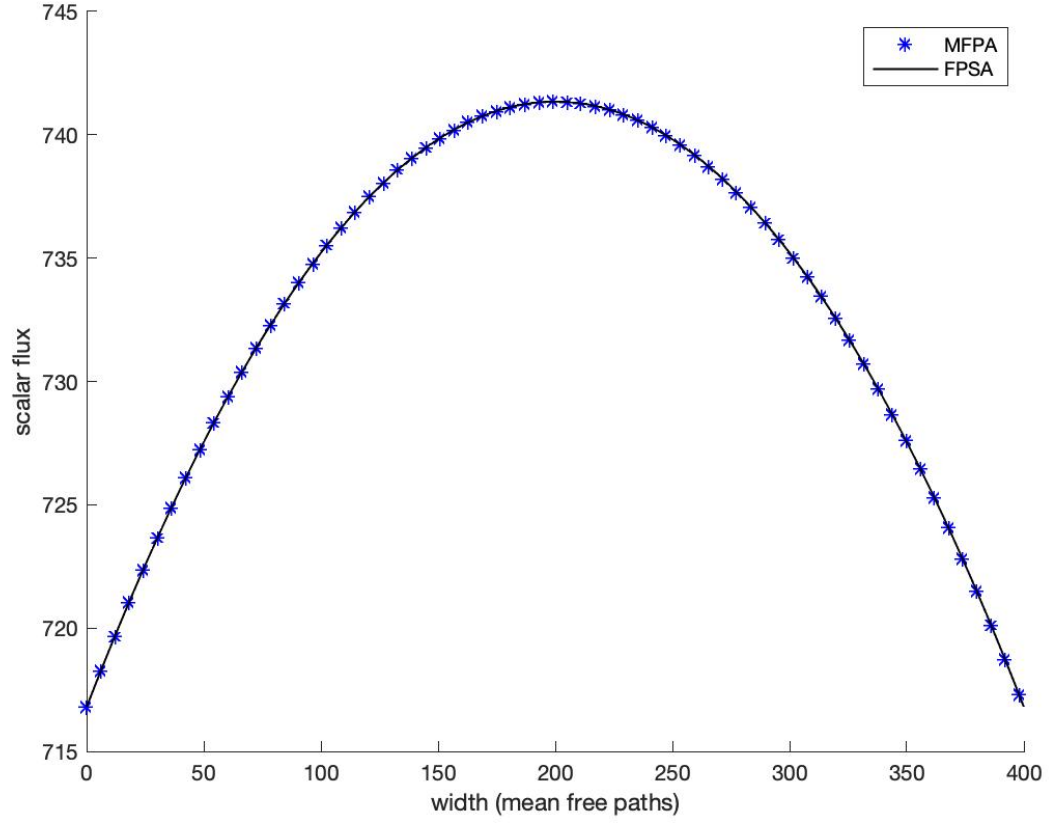


Figure 6.4: Problem 1 Results for SRK with  $\eta = 10^{-7}$

MFPA all converged to the same solution for problem 1 using the false convergence criterion from Eq. (6.4).

Runtime and iteration count are shown Table 6.8. MFPA and FPFA have comparable results, both tremendously outperforming DSA in runtime for all cases. We see a reduction

Parameter	Solver	Runtime (s)	Iterations
$\eta = 10^{-5}$	DSA	2380	53585
	FPSA	1.21	26
	MFPA	1.39	26
$\eta = 10^{-6}$	DSA	3040	69156
	FPSA	0.747	16
	MFPA	0.857	16
$\eta = 10^{-7}$	DSA	3270	73940
	FPSA	0.475	10
	MFPA	0.542	10

Table 6.8: Runtime and Iteration Counts for Problem 1 with SRK

in runtime and iterations for FPSA and MFPA as the FP limit is approached, with DSA requiring many more iterations by comparison as  $\eta$  approaches 0.

A comparison of runtimes and iterations is given in Table 6.9 of non accelerated transport, MFPA, and FPSA using GMRES against MFPA using Picard iteration with the GMRES convergence criterion in Eq. (6.5). We see that FPSA-GMRES, MFPA-GMRES, and MFPA-Picard greatly outperform non accelerated GMRES. Note that FPSA- GMRES and MFPA-GMRES require extra time for the setup of the preconditioner, adding more time(one to two orders of magnitude) to the results shown in the tables. For example, the setup time for MFPA-GMRES Problem 1 with SRK using  $\eta = 10^{-7}$  was 20 seconds longer than the setup using Picard. MFPA-Picard therefore has the fastest runtime overall. Figure 6.4 shows the solution for SRK with  $\eta = 10^{-7}$ .

Parameter	Solver	Runtime (s)	Iterations
$\eta = 10^{-5}$	GMRES	143	2210
	FPSA-GMRES	0.589	11
	MFPA-Picard	1.02	18
	MFPA-GMRES	0.539	11
$\eta = 10^{-6}$	GMRES	216	3780
	FPSA-GMRES	0.367	6
	MFPA-Picard	0.558	10
	MFPA-GMRES	0.399	7
$\eta = 10^{-7}$	GMRES	168	3600
	FPSA-GMRES	0.274	6
	MFPA-Picard	0.301	5
	MFPA-GMRES	0.311	4

Table 6.9: Runtime and Iteration Counts for GMRES Problem 1 with SRK

### **EK Results**

Figure 6.5 shows the solution for problem 1 with EK with  $\Delta = 10^{-7}$ . FPSA and MFPA all converged to the same solution for problem 1.

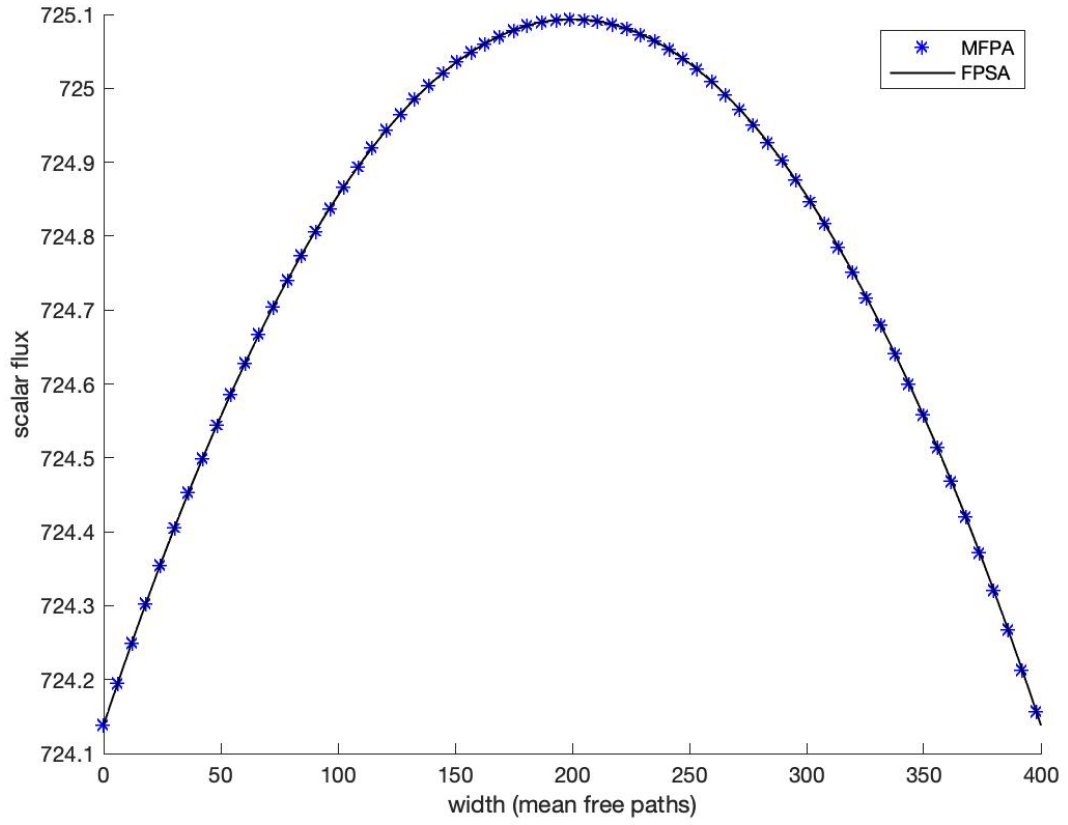


Figure 6.5: Problem 1 Results for EK with  $\Delta = 10^{-7}$

Parameter	Solver	Runtime (s)	Iterations
$\Delta = 10^{-5}$	DSA	3110	70140
	FPSA	0.514	11
	MFPA	0.630	11
$\Delta = 10^{-6}$	DSA	3120	70758
	FPSA	0.388	7
	MFPA	0.393	7
$\Delta = 10^{-7}$	DSA	3120	70851
	FPSA	0.292	6
	MFPA	0.318	6

Table 6.10: Runtime and Iteration Counts for Problem 1 with EK

The runtimes and iterations for DSA, FPSA, and MFPA are shown in Table 6.10. We see a similar trend with the EK as seen with SRK, in that smaller  $\Delta$  values lead to a reduction in runtime and iterations for MFPA and FPSA, which greatly outperform DSA in both categories.

The comparison of runtimes and iterations of non accelerated transport, MFPA, and FPSA using GMRES against MFPA using Picard iteration with the GMRES convergence criterion for the Exponential Kernel are given in Table 6.11. We see a similar behavior to the SRK problems for runtimes and iterations of MFPA-Picard when compared to FPSA-GMRES, MFPA-GMRES, and non accelerated GMRES. Once again, we note that FPSA-GMRES and MFPA-GMRES require extra time for the setup of the preconditioner, adding more time to the results shown in the tables.

Parameter	Solver	Runtime (s)	Iterations
$\Delta = 10^{-5}$	GMRES	206	4140
	FPSA-GMRES	0.320	5
	MFPA-Picard	0.350	6
	MFPA-GMRES	0.298	5
$\Delta = 10^{-6}$	GMRES	143	2860
	FPSA-GMRES	0.237	3
	MFPA-Picard	0.240	4
	MFPA-GMRES	0.228	3
$\Delta = 10^{-7}$	GMRES	124	486
	FPSA-GMRES	0.228	3
	MFPA-Picard	0.185	3
	MFPA-GMRES	0.226	3

Table 6.11: Runtime and Iteration Counts for GMRES Problem 1 with EK

## HGK Results

Figure 6.6 shows the solution for problem 1 with HGK with  $g = 0.99$ . FPSA and MFPA converged to the same solution for problem 1. The results of DSA, FPSA, and MFPA are shown in Table 6.12.

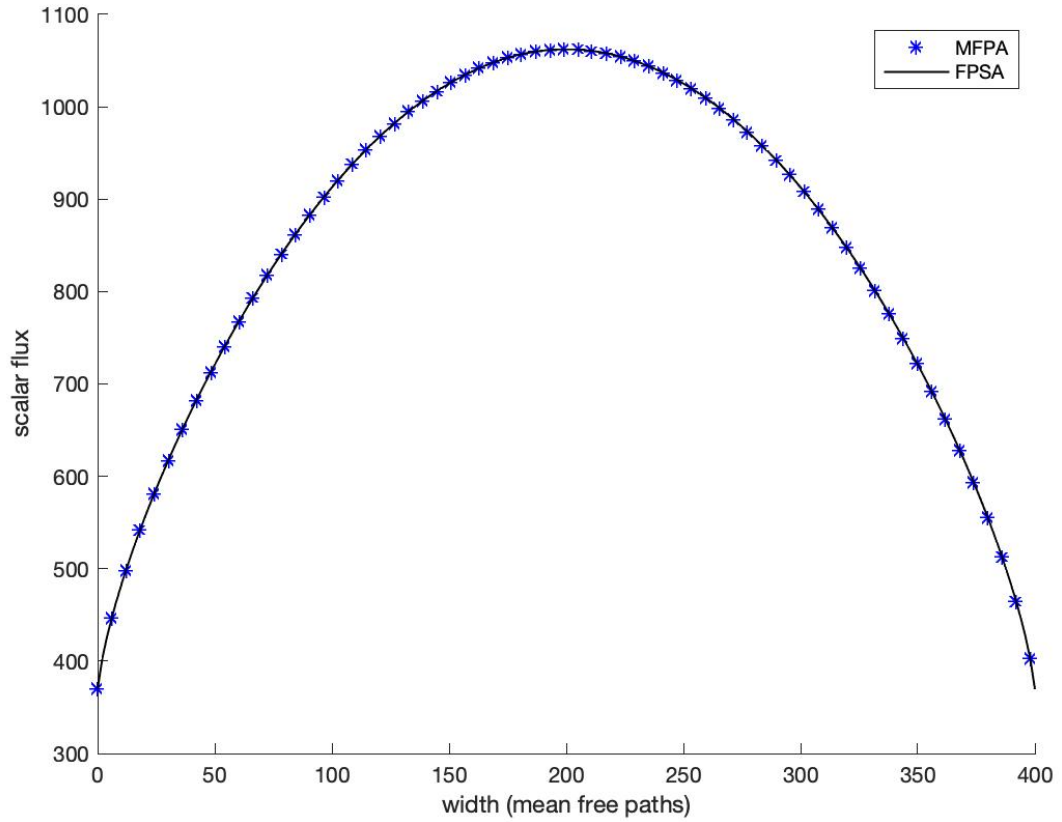


Figure 6.6: Problem 1 Results for HGK with  $g = 0.99$

Parameter	Solver	Runtime (s)	Iterations
$g = 0.9$	DSA	24.5	554
	FPSA	1.50	32
	MFPA	1.39	27
$g = 0.95$	DSA	47.7	1083
	FPSA	1.75	38
	MFPA	1.83	35
$g = 0.99$	DSA	243	5530
	FPSA	3.38	74
	MFPA	3.93	73

Table 6.12: Runtime and Iteration Counts for Problem 1 with HGK

Here we see that MFPA and FPSA do not perform as well compared to their results for the SRK and EK. Contrary to what happened in those cases, both solvers require more time and iterations as the problem becomes more anisotropic. This is somewhat expected, due to HGK not having a valid Fokker-Planck limit. However, both MFPA and FPSA continue to greatly outperform DSA.

Once again, we compare runtimes and iterations of non accelerated transport, MFPA, and FPSA using GMRES against MFPA using Picard iteration with the GMRES convergence criterion, given in Table 6.13. HGK presents a similar trend compared to SRK and EK. FPSA-GMRES, MFPA-Picard, MFPA-GMRES all outperform non accelerated GMRES.

Parameter	Solver	Runtime (s)	Iterations
$g = 0.9$	GMRES	98.6	92
	FPSA-GMRES	0.494	9
	MFPA-Picard	1.24	21
	MFPA-GMRES	0.512	10
$g = 0.95$	GMRES	106	2112
	FPSA-GMRES	0.618	12
	MFPA-Picard	1.63	29
	MFPA-GMRES	0.632	13
$g = 0.99$	GMRES	85.7	1131
	FPSA-GMRES	1.161	24
	MFPA-Picard	3.13	58
	MFPA-GMRES	1.135	26

Table 6.13: Runtime and Iteration Counts for GMRES Problem 1 with HGK

### 6.5.2 Problem Set 2

Problem 2 was tested for the SRK, EK, and HGK. The results found are shown below. GMRES, DSA, FPSA, and MFPA all converged to the same solution for problem 2 for all kernels.

#### SRK Results

Figure 6.7 shows the solution for problem 2 with SRK with  $\eta = 10^{-7}$ .



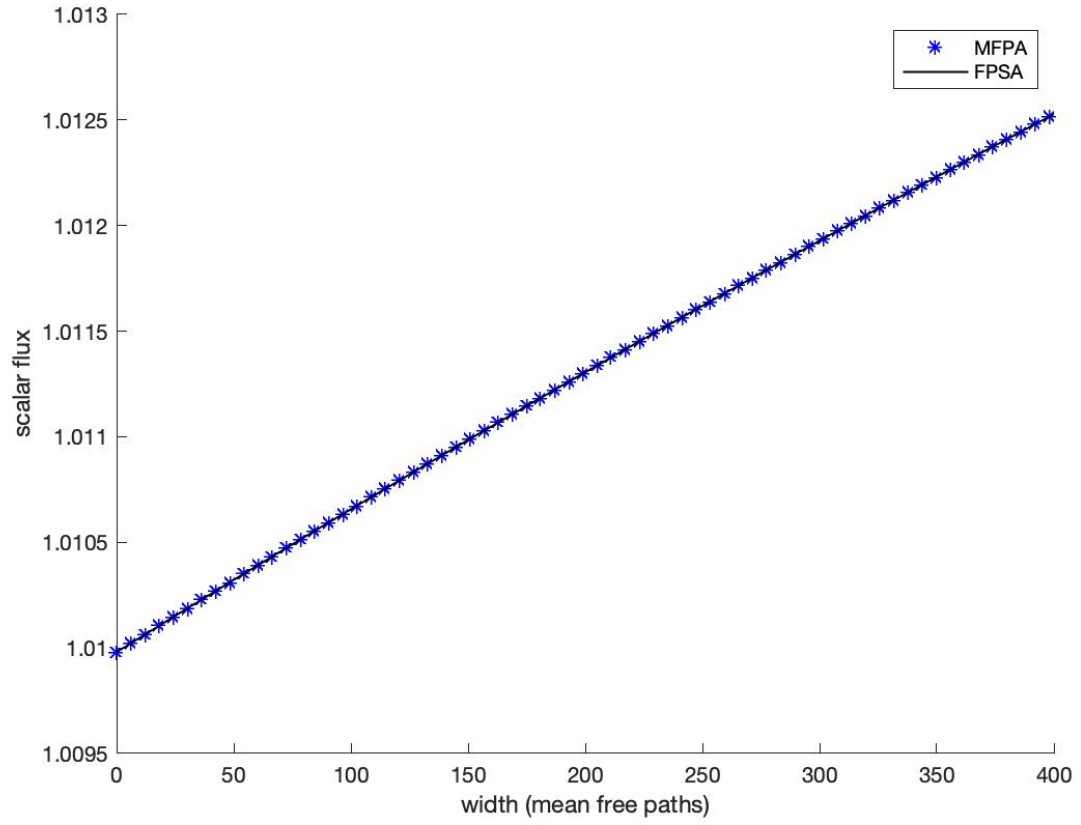


Figure 6.7: Problem 2 Results for SRK with  $\eta = 10^{-7}$

Parameter	Solver	Runtime (s)	Iterations
$\eta = 10^{-5}$	DSA	1107	25072
	FPSA	0.953	20
	MFPA	1.14	20
$\eta = 10^{-6}$	DSA	1434	32562
	FPSA	0.730	14
	MFPA	0.857	14
$\eta = 10^{-7}$	DSA	1470	33246
	FPSA	0.438	8
	MFPA	0.484	8

Table 6.14: Runtime and Iteration Counts for Problem 2 with SRK

The results shown in Tables 6.14 and 6.15 show a similar trend as those found in problem 1. FPSA and MFPA far outperform DSA in runtime and iterations. FPSA-GMRES, MFPA-Picard, and MFPA-GMRES converge faster than non accelerated GMRES.

Parameter	Solver	Runtime (s)	Iterations
$\eta = 10^{-5}$	GMRES	62.6	810
	FPSA-GMRES	0.608	11
	MFPA-Picard	0.664	12
	MFPA-GMRES	0.517	10
$\eta = 10^{-6}$	GMRES	107	72
	FPSA-GMRES	0.432	7
	MFPA-Picard	0.347	6
	MFPA-GMRES	0.389	7
$\eta = 10^{-7}$	GMRES	113	1458
	FPSA-GMRES	0.309	4
	MFPA-Picard	0.237	4
	MFPA-GMRES	0.357	4

Table 6.15: Runtime and Iteration Counts for GMRES Problem 2 with SRK

### **EK Results**

Figure 6.8 shows the solution for problem 2 with EK with  $\Delta = 10^{-7}$ .

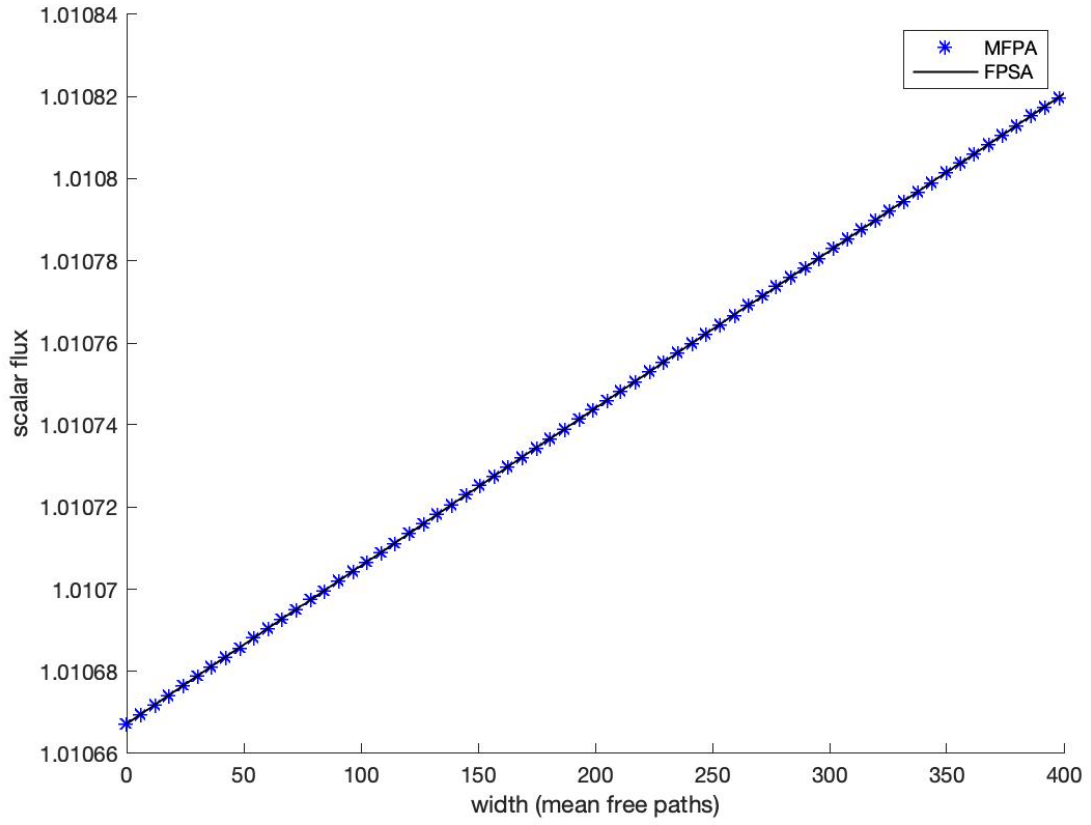


Figure 6.8: Problem 2 Results for EK with  $\Delta = 10^{-7}$

Parameter	Solver	Runtime (s)	Iterations
$\Delta = 10^{-5}$	DSA	1455	33033
	FPSA	0.492	10
	MFPA	0.613	10
$\Delta = 10^{-6}$	DSA	1470	33309
	FPSA	0.358	7
	MFPA	0.431	7
$\Delta = 10^{-7}$	DSA	1470	33339
	FPSA	0.273	5
	MFPA	0.319	5

Table 6.16: Runtime and Iteration Counts for Problem 2 with EK

Tables 6.16 and 6.17 show similar results to those found in problem 1. FPSA and MFPA far outperform DSA in runtime and iterations. FPSA-GMRES, MFPA-Picard, and MFPA-GMRES converge faster than non accelerated GMRES.

Parameter	Solver	Runtime (s)	Iterations
$\Delta = 10^{-5}$	GMRES	96.0	544
	FPSA-GMRES	0.324	5
	MFPA-Picard	0.257	4
	MFPA-GMRES	0.293	5
$\Delta = 10^{-6}$	GMRES	80.1	533
	FPSA-GMRES	0.236	3
	MFPA-Picard	0.183	3
	MFPA-GMRES	0.226	3
$\Delta = 10^{-7}$	GMRES	62.8	1110
	FPSA-GMRES	0.237	3
	MFPA-Picard	0.126	2
	MFPA-GMRES	0.182	2

Table 6.17: Runtime and Iteration Counts for GMRES Problem 2 with EK

### **HGK Results**

Figure 6.9 shows the solution for problem 2 with HGK with  $g = 0.99$ .

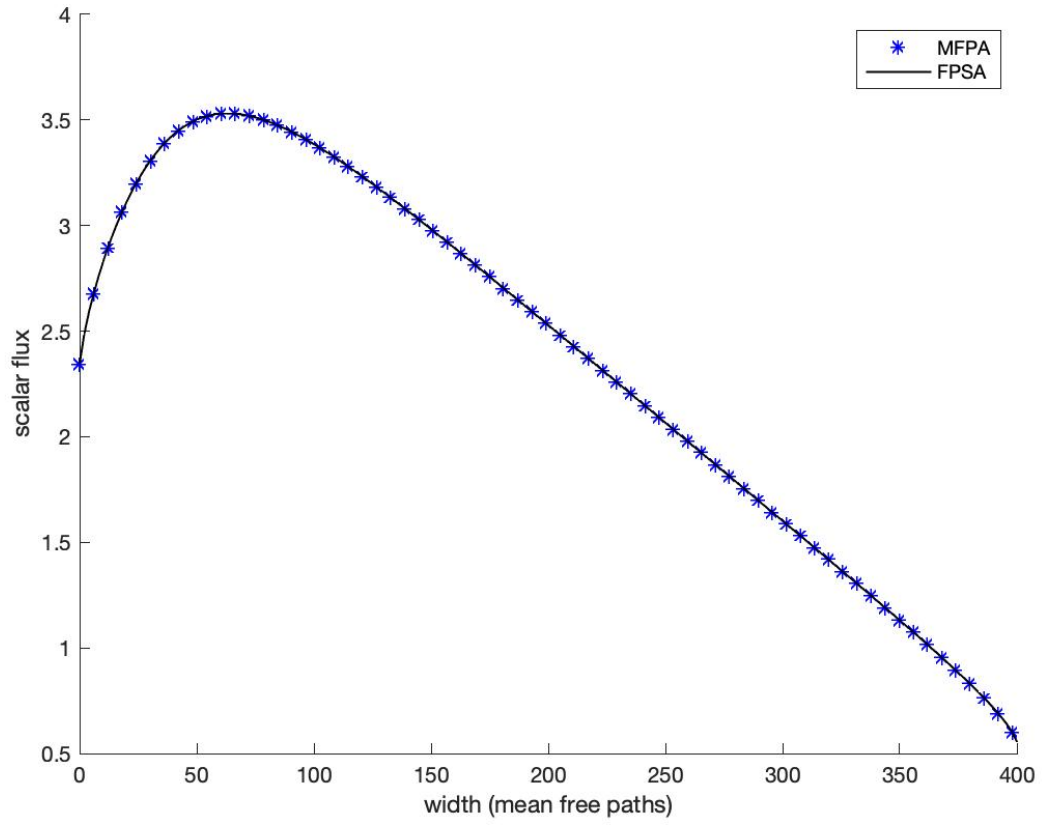


Figure 6.9: Problem 2 Results for HGK with  $g = 0.99$

Again, we see similar results in Tables 6.18 and 6.19 compared to problem 1. FPSA and MFPA outperform DSA in runtime and iterations. FPSA-GMRES, MFPA-Picard, and MFPA-GMRES converge faster than non accelerated GMRES.

Parameter	Solver	Runtime (s)	Iterations
$g = 0.9$	DSA	14.8	336
	FPSA	1.15	23
	MFPA	1.35	24
$g = 0.95$	DSA	29.7	675
	FPSA	1.56	32
	MFPA	1.90	33
$g = 0.99$	DSA	146	3345
	FPSA	3.31	67
	MFPA	3.99	67

Table 6.18: Runtime and Iteration Counts for Problem 2 with HGK

Parameter	Solver	Runtime (s)	Iterations
$g = 0.9$	GMRES	29.1	265
	FPSA-GMRES	0.678	13
	MFPA-Picard	1.07	19
	MFPA-GMRES	0.659	14
$g = 0.95$	GMRES	36.9	330
	FPSA-GMRES	0.864	17
	MFPA-Picard	1.46	26
	MFPA-GMRES	0.863	19
$g = 0.99$	GMRES	39.9	14
	FPSA-GMRES	1.53	32
	MFPA-Picard	2.98	54
	MFPA-GMRES	1.49	35

Table 6.19: Runtime and Iteration Counts for GMRES Problem 2 with HGK

## 6.6 Heterogeneous Slab Results

In order to test the accuracy of the method when dealing with interface conditions, two heterogeneous slab problems were tested. The same general parameters were used as in the previous sections, with the modification of 100 spatial cells,  $Z = 100$  mean free paths, and  $\Sigma_a = 0.0001$ . The heterogeneous slab was setup similar to the one in [82], with a step function cross-section given by

$$\bar{\Sigma}_{s,0}(z) = \begin{cases} \Sigma_{s,0}(x)(1 + \varepsilon), & 0 \leq z \leq \frac{Z}{2} \\ \Sigma_{s,0}(x)(1 - \varepsilon), & \frac{Z}{2} \leq z \leq Z \end{cases} \quad (6.18)$$

where  $\varepsilon$  is a constant.

We consider the SRK with  $\Sigma_{s,0} = 0.5$  and  $\eta = 10^{-7}$ , the EK with  $\Sigma_{s,0} = 0.5$  and  $\Delta = 10^{-7}$ , and the HGK with  $\Sigma_{s,0} = 1.0$  and  $g = 0.99$ . The values of  $\varepsilon$  are chosen as  $-0.8, -0.4, 0.4, 0.8$ . We tested non accelerated GMRES and MFPA using finite element discretization and Picard iteration with the convergence criterion shown in Eq. (6.5).

### 6.6.1 Problem Set 1

#### SRK Results

Figure 6.10 shows the SRK results for problem 1 using a heterogeneous slab. GMRES and MFPA converged to the same result. We expect to see a reflective relationship due to our choice of  $\varepsilon$  and definition of the cross-section as a step function. MFPA showed no loss of accuracy in heterogeneous media using the SRK.

#### EK Results

We see similar results in Fig. 6.11 when testing the EK for heterogeneous slab problem 1. The changes in scalar flux are not as significant as in the SRK when using the step function cross-section. The accuracy of the MFPA method in this heterogeneous slab has not been negatively affected.

### **HGK Results**

We see interesting results in Fig. 6.12 when testing the HGK for heterogeneous slab problem 1. Once again, MFPA and GMRES converged to the same solution, with MFPA having no loss of accuracy in the heterogeneous slab.

## **6.6.2 Problem Set 2**

### **SRK Results**

The results for heterogeneous problem 2 in Fig. 6.13 are similar to problem 1. GMRES and MFPA converged to the same result. MFPA showed no loss of accuracy.

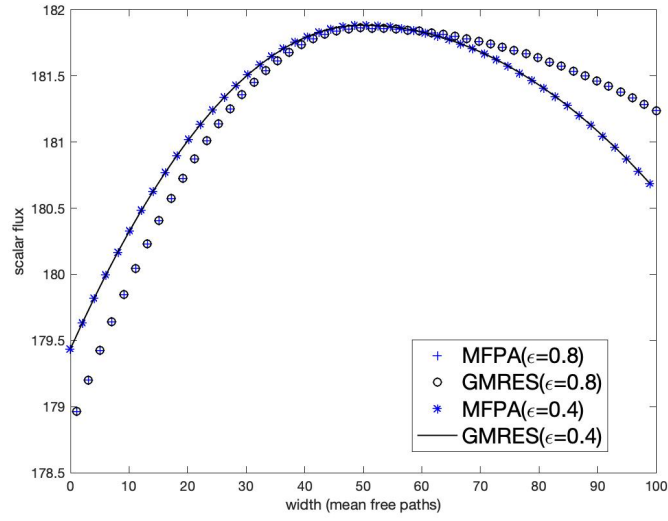
### **EK Results**

Problem 2 with the EK results in Fig. 6.14 what was expected. MFPA and GMRES converged to the same solution and MFPA had no loss of accuracy.

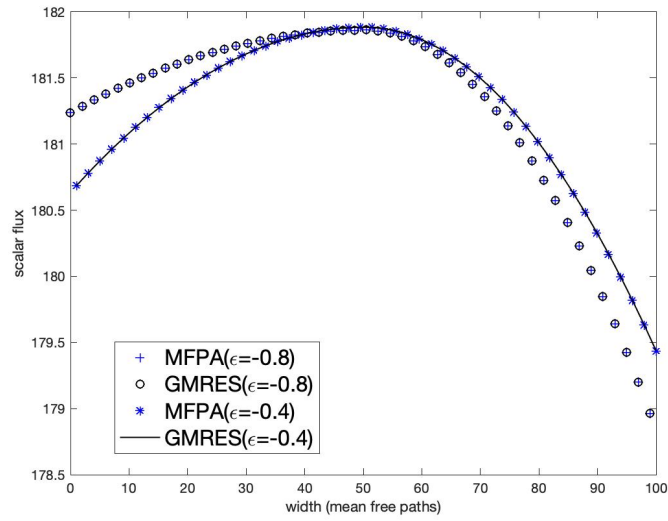
### **HGK Results**

Again we see expected results in Fig. 6.15 when testing problem 2 with the HGK. MFPA and GMRES converged to the same solution. No loss of accuracy was shown for problem 2 when using MFPA.



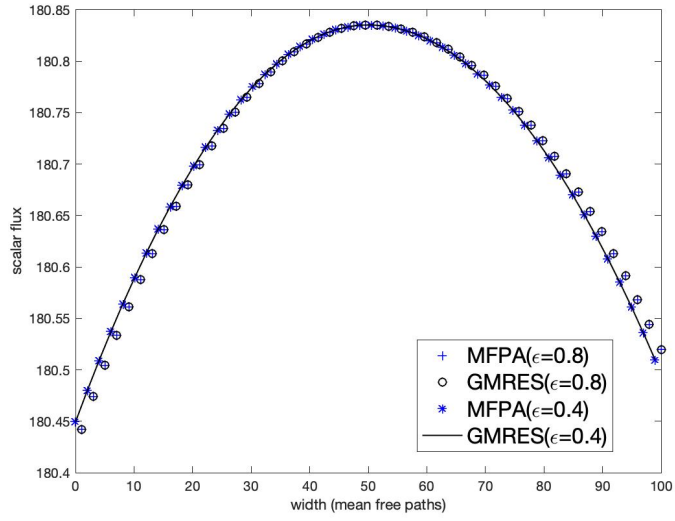


(a) Problem 1,  $\varepsilon = 0.4, 0.8$

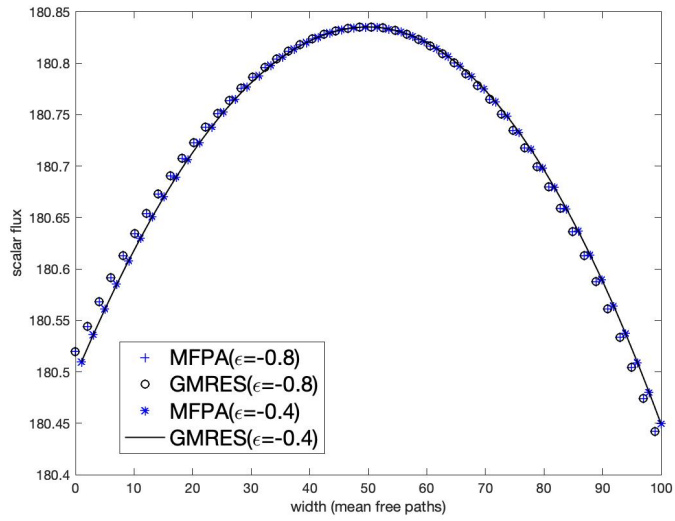


(b) Problem 1,  $\varepsilon = -0.4, -0.8$

Figure 6.10: Results for Heterogeneous Problem 1 using SRK with  $\varepsilon = \pm 0.4, \pm 0.8$

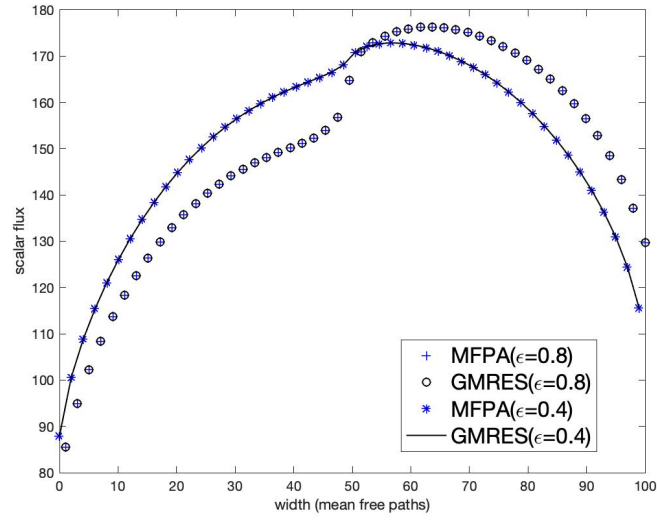


(a) Problem 1,  $\varepsilon = 0.4, 0.8$

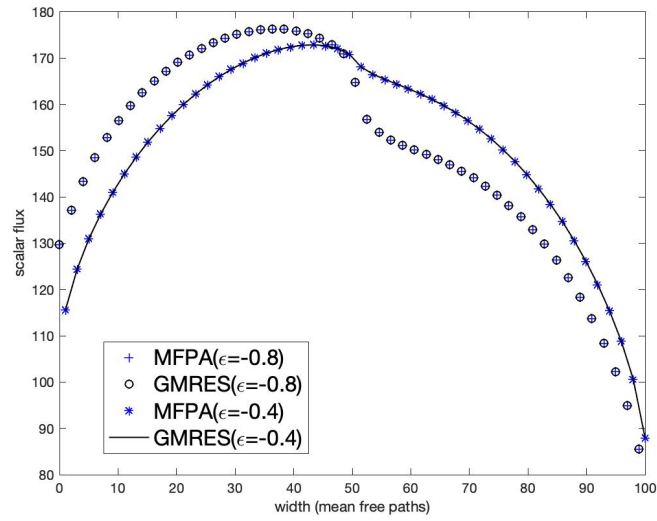


(b) Problem 1,  $\varepsilon = -0.8, -0.4$

Figure 6.11: Results for Heterogeneous Problem 1 using EK with  $\varepsilon = \pm 0.4, \pm 0.8$

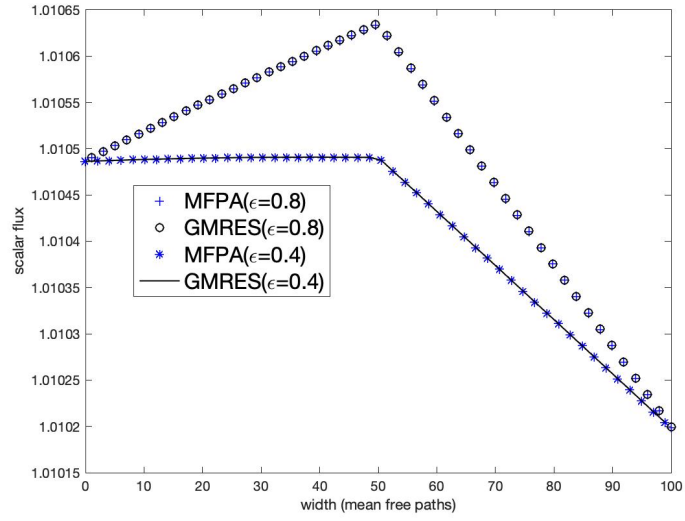


(a) Problem 1,  $\varepsilon = 0.4, 0.8$

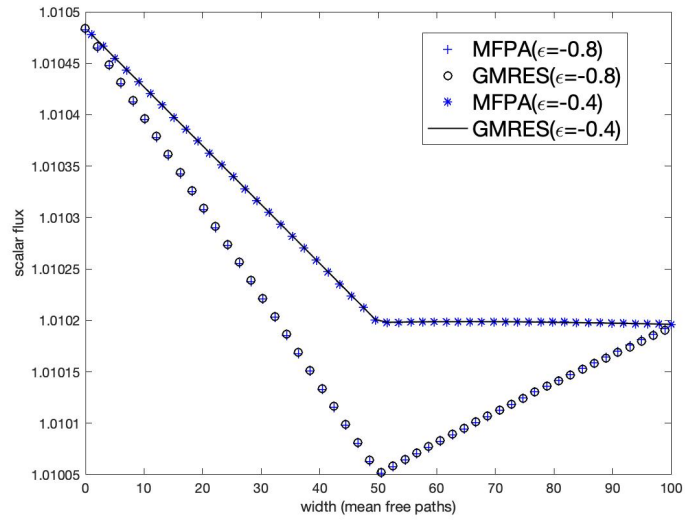


(b) Problem 1,  $\varepsilon = -0.4, -0.8$

Figure 6.12: Results for Heterogeneous Problem 1 using HGK with  $\varepsilon = \pm 0.4, \pm 0.8$

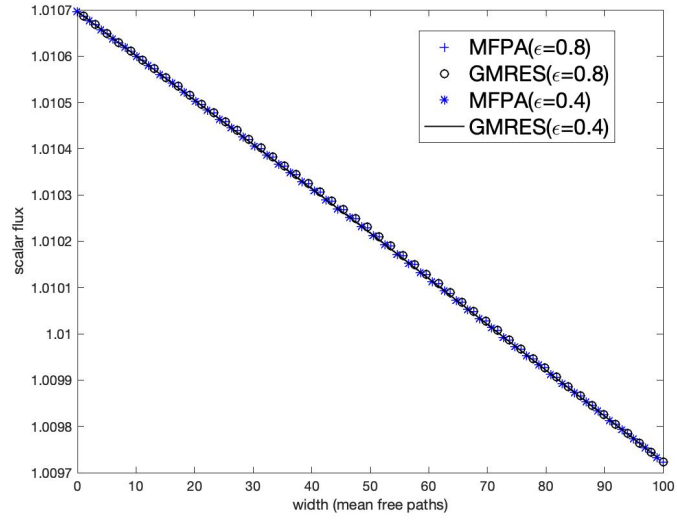


(a) Problem 2,  $\varepsilon = 0.4, 0.8$

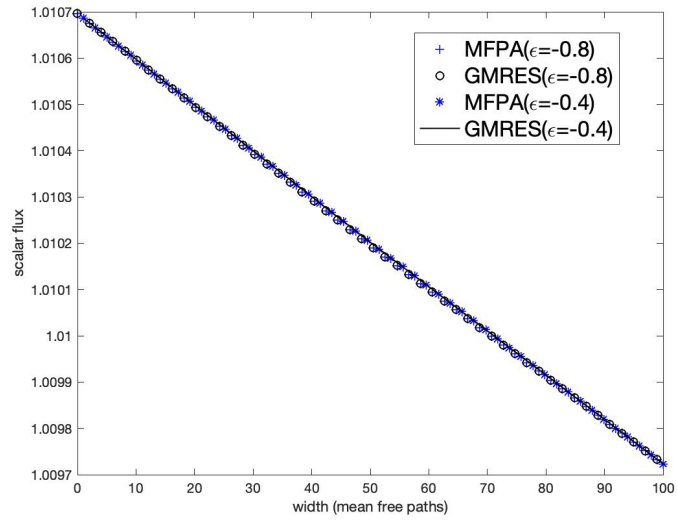


(b) Problem 2,  $\varepsilon = -0.4, -0.8$

Figure 6.13: Results for Heterogeneous Problem 2 using SRK with  $\varepsilon = \pm 0.4, \pm 0.8$

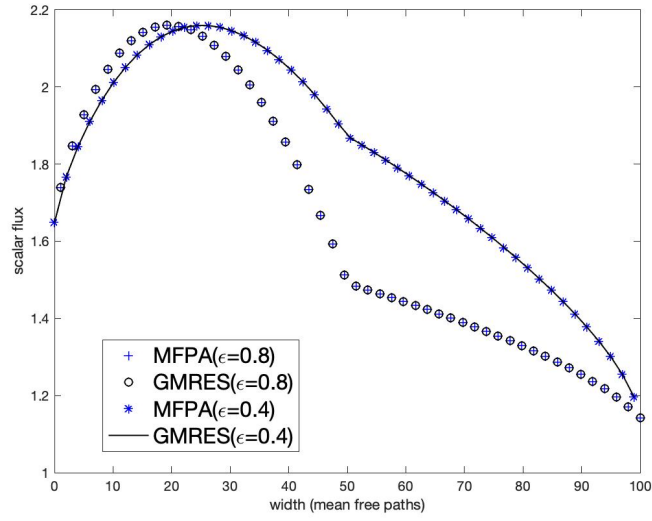


(a) Problem 2,  $\varepsilon = 0.4, 0.8$

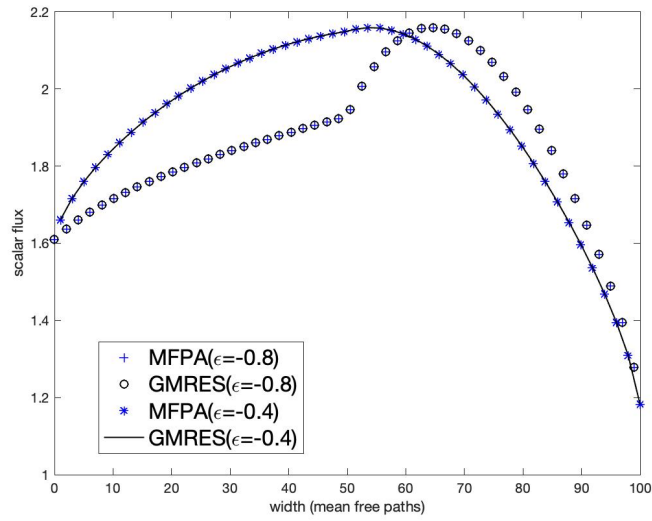


(b) Problem 2,  $\varepsilon = -0.4, -0.8$

Figure 6.14: Results for Heterogeneous Problem 2 using EK with  $\varepsilon = \pm 0.4, \pm 0.8$



(a) Problem 2,  $\varepsilon = 0.4, 0.8$



(b) Problem 2,  $\varepsilon = -0.4, -0.8$

Figure 6.15: Results for Heterogeneous Problem 2 using HGK with  $\varepsilon = \pm 0.4, \pm 0.8$

## Chapter 7: Radiative Transfer Multiphysics Test Problem

The advantage MFPA offers over FPSA is the ability to couple the FP equation in multiphysics problems. Isolating the transport equation should allow for fast convergence rates due to reducing the amount of transport sweeps [23]. In this chapter, we introduce a test multiphysics problem that couples thermal radiative transfer with transport. The coupling strategies discussed are similar to strategies shown in [23].

### 7.1 Coupling Transport

In this section, we couple transport with thermal radiative transfer, similar to the multiphysics problem described in [31]. For steady state, mono-energetic thermal radiative transfer problems in slab geometry, we start with Eq. (3.44) modified to solve for the specific radiation angular intensity  $\Phi(\mu, z) = h\nu\Psi(\mu, z)$ ,

$$\mathcal{L}\Phi = S\Phi + Q, \quad (7.1)$$

where  $h$  is Planck's constant and  $\nu$  is frequency. The source term  $Q$  becomes a black-body reemission [31],

$$Q = \Sigma_a B(T(z)) = \Sigma_a \frac{2h\nu^3}{c^3 (e^{\frac{h\nu}{kT(z)}} - 1)}, \quad (7.2)$$

where  $c$  is the speed of light in a vacuum,  $k$  is the Stefan-Boltzmann constant, and  $T(z)$  is the temperature of the material at location  $z$ . In thermal radiative transfer, photon frequency  $\nu$  is commonly used instead of the energy variable  $E$ .

For steady state, mono-energetic (or mono-frequency) transport, the temperature evolution is described by [41]

$$T^4(z) = \frac{1}{ac} \int_{-1}^1 d\mu \Phi(z, \mu) \quad (7.3)$$

where  $a$  is referred to as the radiation constant [41]. The multiphysics problem is given by the following coupled equations:

$$\mathcal{L}\Phi = S\Phi + \Sigma_a \frac{2h\nu^3}{c^3(e^{\frac{h\nu}{kT}} - 1)}, \quad (7.4a)$$

$$T^4 = \frac{1}{ac} \int_{-1}^1 d\mu \Phi. \quad (7.4b)$$

Any of the nonlinear solvers described in Chapter 3 can be used to solve these nonlinearly coupled equations. We choose Picard iteration:

$$\mathcal{L}\Phi^m = S\Phi^{m-1} + \Sigma_a \frac{2h\nu^3}{c^3(e^{\frac{h\nu}{kT^{m-1}}} - 1)}, \quad (7.5a)$$

$$T^n = \left( \frac{1}{ac} \int_{-1}^1 d\mu \Phi^m \right)^{\frac{1}{4}}. \quad (7.5b)$$

The flow chart in Fig. 7.1 displays the algorithm to solve Eqs. (7.4). In Fig. 7.1, the  $L^2$  norm of the intensity and temperature are tested at each respective iteration. The variables  $\varepsilon_\Phi$  and  $\varepsilon_T$  refer to the user specified tolerances for intensity and temperature, respectively.

In this setup there is an outer loop and inner loop. The outer loop contains the thermal sweeps and the inner loop contains the transport sweeps. After doing one thermal sweep, we get a new source term that is used in the inner loop. We converge transport then do another thermal sweep. This process is done until the temperature has converged to some tolerance.



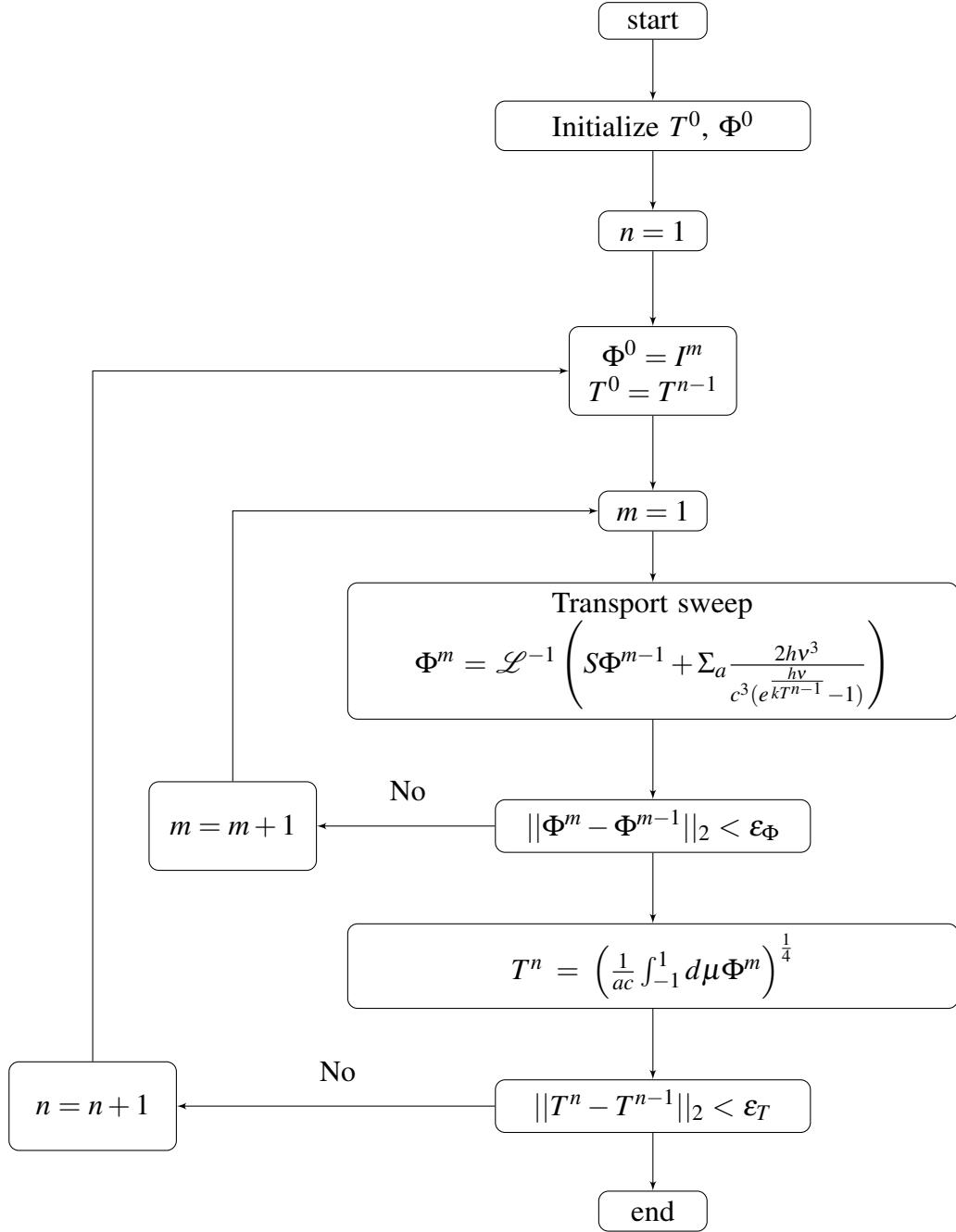


Figure 7.1: Transport-Thermal Coupling Algorithm

## 7.2 Coupling FPSA

For thermal radiative transfer problems that are forward-peaked, highly scattering, the transport sweep should be the most expensive part of the multiphysics solve. We can accelerate the transport solve of the multiphysics problem by using FPSA. We do this by adding a correction step at each transport sweep in the Picard iteration scheme:

$$\mathcal{L}\Phi^{mg} = S\Phi^{m-1} + \Sigma_a \frac{2h\nu^3}{c^3(e^{\frac{h\nu}{kT^{n-1}}} - 1)}, \quad (7.6a)$$

$$\Phi^m = \Phi^{mg} + (\mathcal{A} - \mathcal{F})^{-1} S (\Phi^{mg} - \Phi^{m-1}), \quad (7.6b)$$

$$T^n = \left( \frac{1}{ac} \int_{-1}^1 d\mu \Phi^m \right)^{\frac{1}{4}}. \quad (7.6c)$$

It is important to note that the correction step is not coupled to the thermal equation. The transport equation is still coupled to the thermal equation when using FPSA to accelerate. The flow chart for the FPSA coupled problem using Picard iteration is shown in Fig. 7.2.

We have now included an extra step in the inner loop to converge transport faster. FPSA corrects the error for each transport sweep in the inner loop. We see faster convergence by reducing total transport sweeps done. What is important to note is that transport sweeps and corrections are being done in the inner loop. We want to separate the transport equation from the inner loop to reduce the total number of transport sweeps.

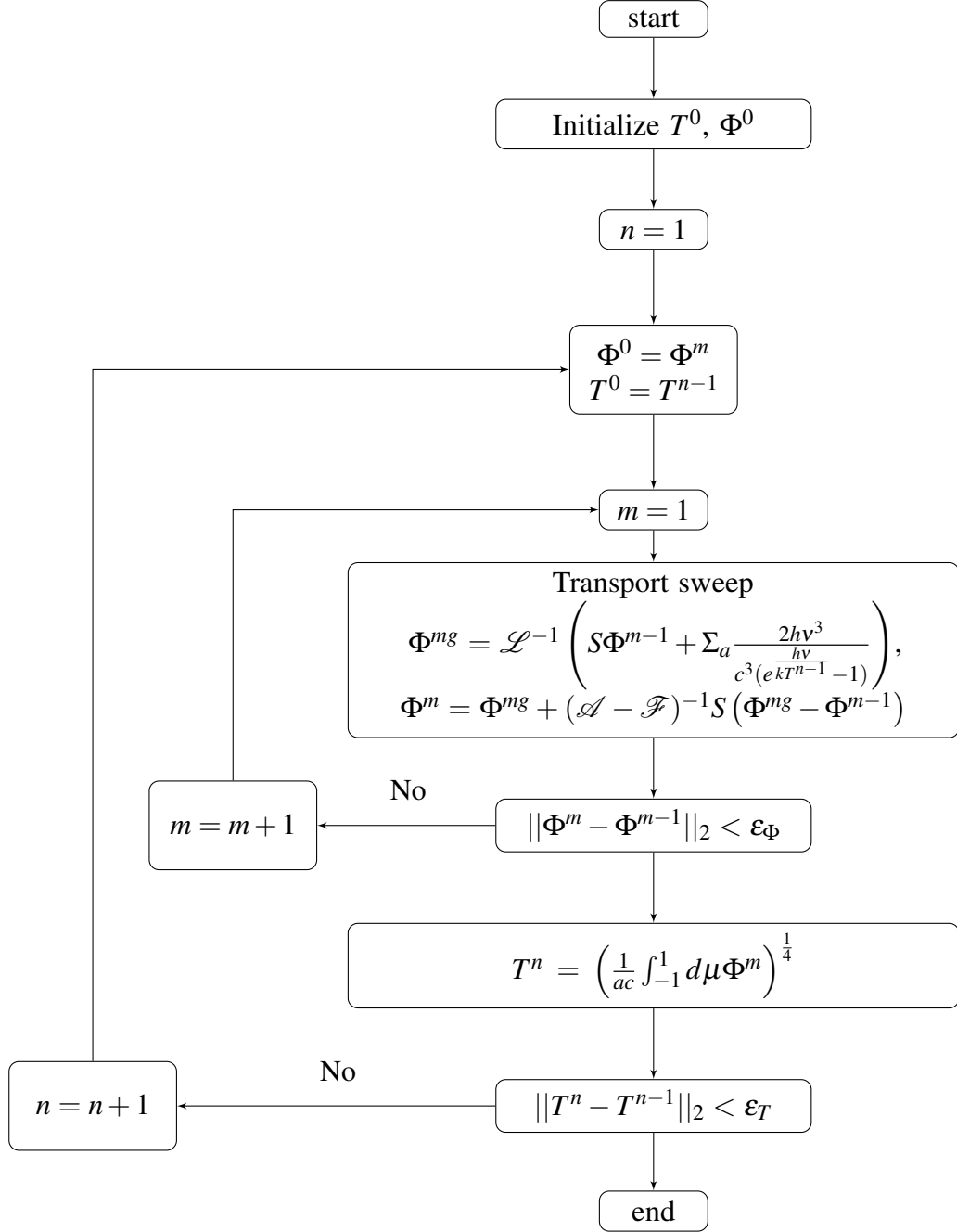


Figure 7.2: FPSA-Thermal Coupling Algorithm

### 7.3 Coupling MFPA

When using FPSA to accelerate multiphysics, transport sweeps are necessary after every thermal solve. To further improve upon accelerating convergence, we can couple the modified FP equation from the linear MFPA method to the thermal equation. In doing so, we converge thermal and the modified MP equation after each transport sweep. This should lead to less transport sweeps overall.

We start with redefining the source term  $Q$  in the modified FP equation using Eq. (7.2),

$$\Phi = \mathcal{P}^{-1} (\hat{D}_F + \Sigma_a B(T(z))), \quad (7.7)$$

with consistency term

$$\hat{D}_F = (S - \mathcal{F} - \Sigma_{s,0}I) \Phi. \quad (7.8)$$

Combining the MFPA equations with Eqs. (7.2) and (7.3) gives the following coupled equations using Picard iteration:

$$\mathcal{L}\Phi_{HO}^n = S\Phi_{HO}^{n-1} + \Sigma_a \frac{2h\nu^3}{c^3(e^{\frac{h\nu}{kT^{n-1}}} - 1)}, \quad (7.9a)$$

$$\hat{D}_F^n = (S - \mathcal{F} - \Sigma_{s,0}I) \Phi_{HO}^n, \quad (7.9b)$$

$$\Phi_{LO}^m = \mathcal{P}^{-1} \left( \hat{D}_F^n + \Sigma_a \frac{2h\nu^3}{c^3(e^{\frac{h\nu}{kT^{m-1}}} - 1)} \right), \quad (7.9c)$$

$$T^m = \left( \frac{1}{ac} \int_{-1}^1 d\mu \Phi_{LO}^m \right)^{\frac{1}{4}}. \quad (7.9d)$$

The variable  $\Phi_{HO}$  refers to the intensity found from each outer transport sweep, and  $\Phi_{LO}$  refers to the intensity found at each FP solve in the inner loop. The flow chart shown in Fig. 7.3 shows the algorithm to solve Eqs. (7.9) using Picard iteration.

In this setup we see that transport sweeps have been moved to the outer loop, and the modified FP equation and thermal equation are in the inner loop. After every transport

sweep, we converge the modified FP equation and thermal equation. In doing so, we limit the amount of transport sweeps when compared to FPSA.

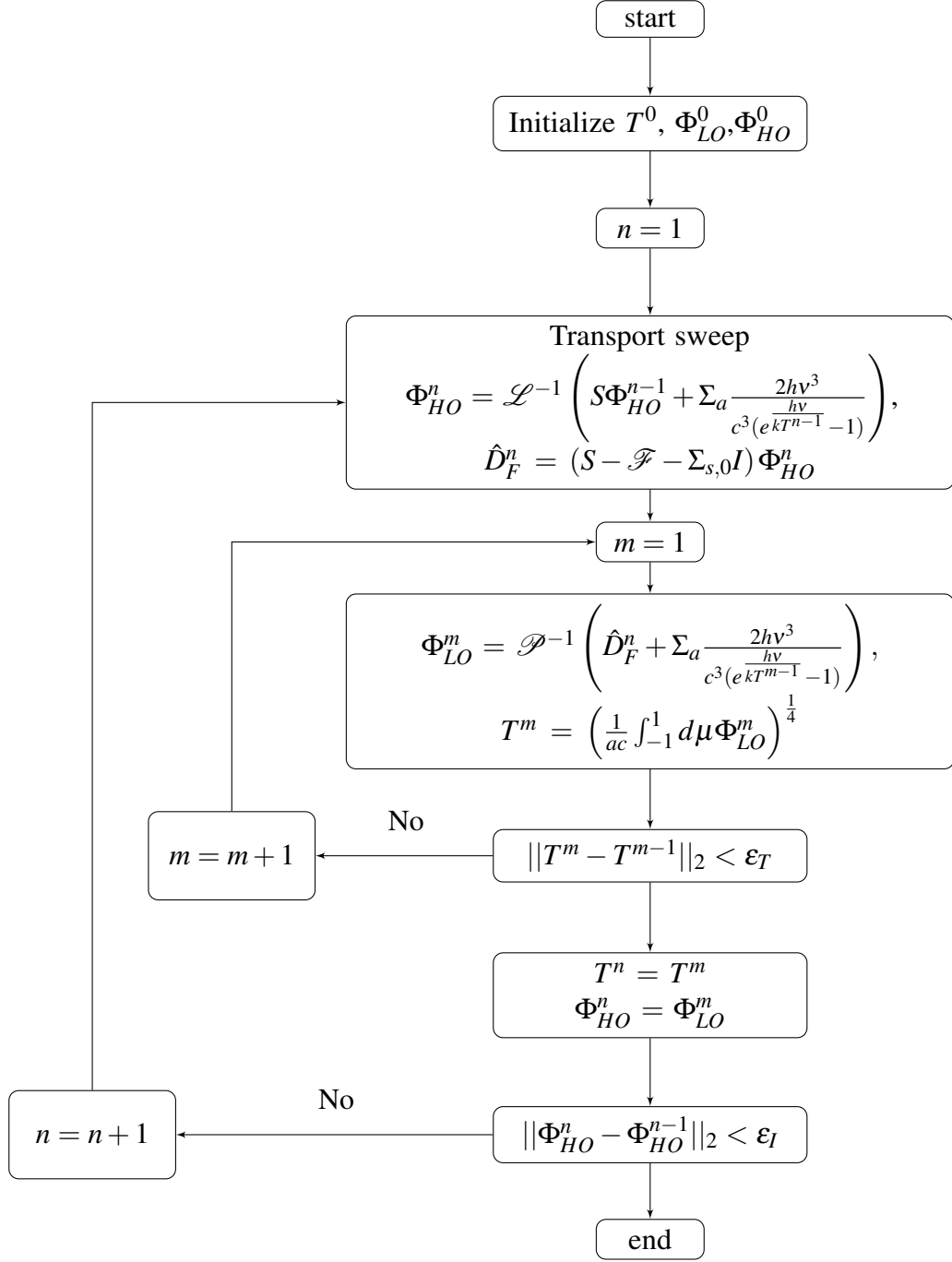


Figure 7.3: MFPA-Thermal Coupling Algorithm

## 7.4 Radiative Transfer Results

The source and boundary conditions follow the setup of problem 2 shown in Table 6.1. All tests were simulated using 100 spatial cells,  $Z = 1$  cm,  $\Sigma_a = 1\text{cm}^{-1}$ , and  $\Sigma_t = \Sigma_{s,0} + \Sigma_a$ . The focus of these tests is not to solve realistic problems, but to see how MFPA coupling performance compares to FPSA coupling performance in a multiphysics problem. The euclidean norms were used to check for convergence at the inner and outer loops in the multiphysics solve and a tolerance of  $10^{-6}$  was used for all convergences.

The performance of MFPA coupling will depend upon how fast the modified FP equation converges in the inner loop. More iterations in the inner loop lead to more thermal sweeps and modified FP solves. The convergence will depend upon the scattering kernel having a valid FP limit. We want to see how MFPA performs based on the FP limit of the kernel. To see this relationship, we test the Exponential kernel and Henyey-Greenstein kernel using three different sets of directions and moments:  $N = 16$  and  $L = 15$ ,  $N = 32$  and  $L = 31$ ,  $N = 64$  and  $L = 63$ . We will also test the Screened Rutherford kernel, as it has a valid FP limit as  $\eta$  approaches 0. We test the SRK using  $N = 16$  and  $L = 15$ , but generate three sets of moments using different  $\eta$  parameters. This will allow us to see how MFPA performs when the FP limit is approached. All MFPA coupling results are compared against unaccelerated transport coupling and FPSA coupling. Error between FPSA and MFPA scalar flux was found using the Euclidean norm:

$$|\phi_{FPSA} - \phi_{MFPA}| = \sqrt{\sum_{k=1}^K (\phi_{FPSA,k} - \phi_{MFPA,k})^2} \quad (7.10)$$

### 7.4.1 Exponential Kernel

The Exponential kernel always has a valid FP limit [28, 29]. The performance of the MFPA coupled inner loop when using the EK should be extremely efficient. The set of scattering moments generated from the Exponential kernel using  $\Delta = 10^{-7}$  are shown in Table 7.1.

For all three problems, coupling with MFPA and FPSA converge to the same solution as non accelerated transport. The results are displayed in Figs. 7.4 to 7.6. Table 7.2 shows the runtimes and transport sweeps for non accelerated transport, FPSA, and MFPA. We see that MFPA coupling outperforms FPSA coupling for all three problems by up to a factor of two. This was expected due to the isolation of transport sweeps when coupling with MFPA. We see that for all three problems, only three transport sweeps needed to be performed for MFPA, while transport sweeps increased for FPSA with increasing angles and moments. Thermal sweeps increased with increasing  $N$  for MFPA but overall sweeps were still less than FPSA. In this problem, transport sweeps are the most expensive part of the solve which is why we see the MFPA converge much faster than FPSA. Table 7.3 shows the error between FPSA and MFPA. The error between FPSA and MFPA is up to three orders of magnitude smaller than the tolerance used in the solves.



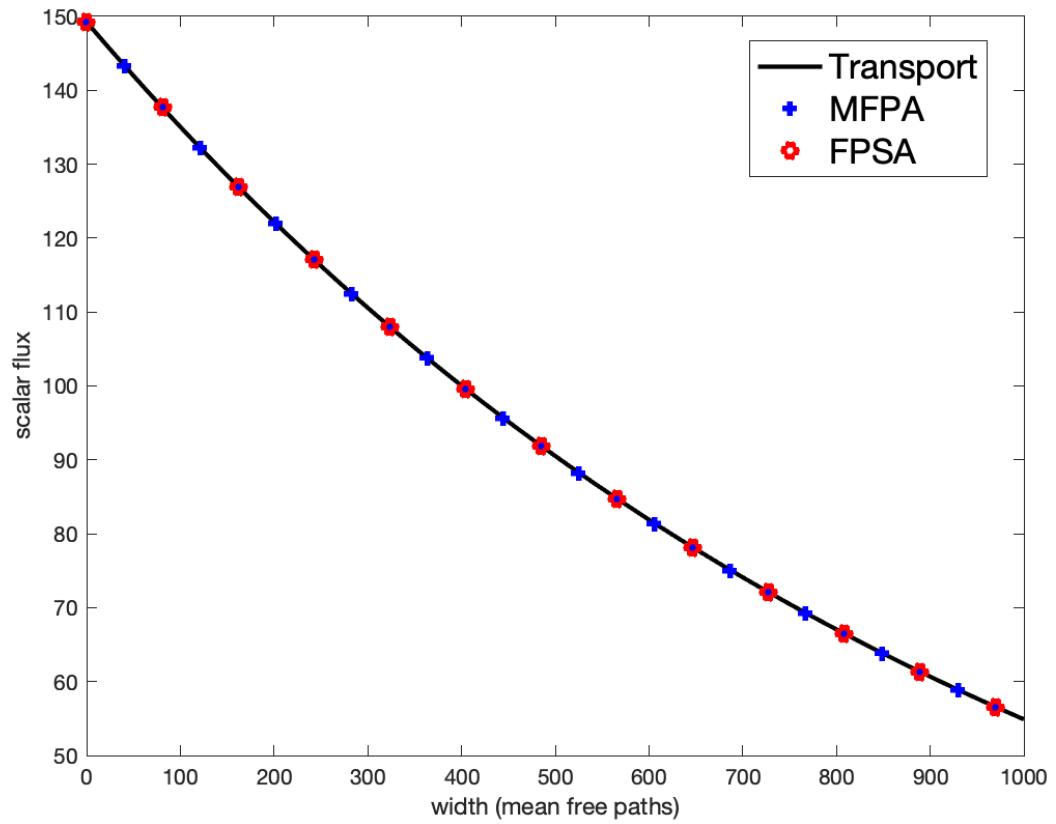


Figure 7.4: Radiative results for  $N = 16$  and  $L = 15$  using EK with  $\Delta = 10^{-7}$

	$cm^{-1}$		$cm^{-1}$
$\Sigma_{s,0}$	1000	$\Sigma_{s,32}$	999.9442
$\Sigma_{s,1}$	999.9999	$\Sigma_{s,33}$	999.9407
$\Sigma_{s,2}$	999.9997	$\Sigma_{s,34}$	999.9373
$\Sigma_{s,3}$	999.9992	$\Sigma_{s,35}$	999.9336
$\Sigma_{s,4}$	999.9988	$\Sigma_{s,36}$	999.93
$\Sigma_{s,5}$	999.9981	$\Sigma_{s,37}$	999.9261
$\Sigma_{s,6}$	999.9975	$\Sigma_{s,38}$	999.9223
$\Sigma_{s,7}$	999.9966	$\Sigma_{s,39}$	999.9182
$\Sigma_{s,8}$	999.9958	$\Sigma_{s,40}$	999.9142
$\Sigma_{s,9}$	999.9947	$\Sigma_{s,41}$	999.9099
$\Sigma_{s,10}$	999.9937	$\Sigma_{s,42}$	999.9057
$\Sigma_{s,11}$	999.9924	$\Sigma_{s,43}$	999.9012
$\Sigma_{s,12}$	999.9912	$\Sigma_{s,44}$	999.8968
$\Sigma_{s,13}$	999.9897	$\Sigma_{s,45}$	999.8921
$\Sigma_{s,14}$	999.9883	$\Sigma_{s,46}$	999.8875
$\Sigma_{s,15}$	999.9866	$\Sigma_{s,47}$	999.8826
$\Sigma_{s,16}$	999.985	$\Sigma_{s,48}$	999.8778
$\Sigma_{s,17}$	999.9831	$\Sigma_{s,49}$	999.8727
$\Sigma_{s,18}$	999.9813	$\Sigma_{s,50}$	999.8677
$\Sigma_{s,19}$	999.9792	$\Sigma_{s,51}$	999.8624
$\Sigma_{s,20}$	999.9772	$\Sigma_{s,52}$	999.8572
$\Sigma_{s,21}$	999.9749	$\Sigma_{s,53}$	999.8517
$\Sigma_{s,22}$	999.9727	$\Sigma_{s,54}$	999.8463
$\Sigma_{s,23}$	999.9702	$\Sigma_{s,55}$	999.8406
$\Sigma_{s,24}$	999.9678	$\Sigma_{s,56}$	999.835
$\Sigma_{s,25}$	999.9651	$\Sigma_{s,57}$	999.8291
$\Sigma_{s,26}$	999.9625	$\Sigma_{s,58}$	999.8233
$\Sigma_{s,27}$	999.9596	$\Sigma_{s,59}$	999.8172
$\Sigma_{s,28}$	999.9568	$\Sigma_{s,60}$	999.8112
$\Sigma_{s,29}$	999.9537	$\Sigma_{s,61}$	999.8049
$\Sigma_{s,30}$	999.9507	$\Sigma_{s,62}$	999.7987
$\Sigma_{s,31}$	999.9474	$\Sigma_{s,63}$	999.7922

Table 7.1: Exponential cross-section Moments for  $\Delta = 10^{-7}$

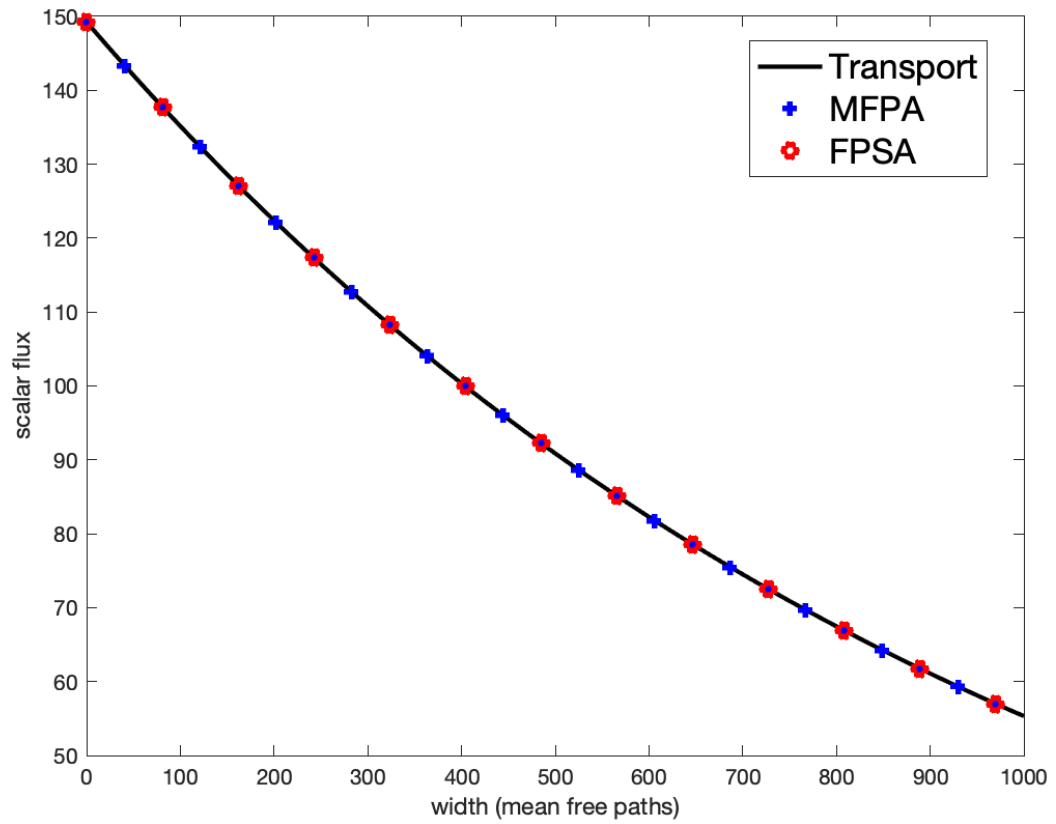


Figure 7.5: Radiative results for  $N = 32$  and  $L = 31$  using EK with  $\Delta = 10^{-7}$

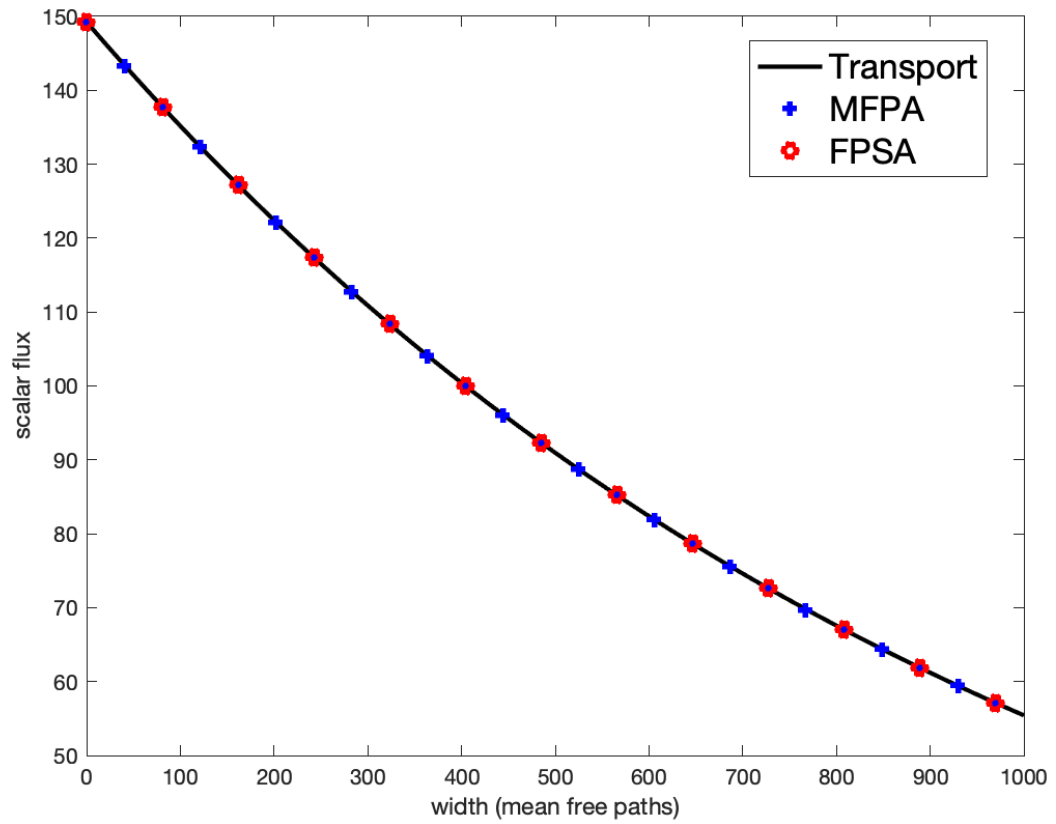


Figure 7.6: Radiative results for  $N = 64$  and  $L = 63$  using EK with  $\Delta = 10^{-7}$

N/L	Method	Runtime (s)	Transport sweeps	Thermal sweeps
16/15	Transport	5.10	5364	3
	FPSA	0.109	8	3
	MFPA	0.0488	4	7
32/31	Transport	17.0	4562	3
	FPSA	0.396	7	3
	MFPA	0.296	4	7
64/63	Transport	59.4	3700	3
	FPSA	1.63	7	3
	MFPA	1.36	4	7

Table 7.2: Runtime, Transport and Thermal Sweeps for Radiative Transfer Problem using non accelerated transport, FPSA coupling, and MFPA coupling with EK

N/L	Error ( $\times 10^{-7}$ )
16/15	0.233
32/31	0.0581
64/63	0.0845

Table 7.3: Error(Eq. (7.10)) between angular flux moments found from MFPA coupling versus FPSA coupling using EK

#### 7.4.2 Henyey-Greenstein Kernel

The Henyey-Greenstein kernel does not have a valid FP limit [28, 29]. The MFPA coupled inner loop should require more iterations when using the HGK versus the EK. The

set of scattering moments generated from the Henyey-Greenstein kernel using  $g = 0.99$  are shown in Table 7.4.

For all three problems, coupling with MFPA and FPSA converge to the same solution as non accelerated transport. The results are displayed in Figs. 7.7 to 7.9. Table 7.5 shows the runtimes and transport sweeps for non accelerated transport, FPSA, and MFPA. We see that FPSA coupling outperforms MFPA coupling for two of the three problems tested. The number of transport sweeps is reduced when using MFPA coupling versus FPSA coupling, but the number of thermal sweeps is significantly increased. We are seeing the effect of the HGK not having a valid FP limit. This leads to slower convergence of the modified FP equation and requires more iterations in the inner loop. As the problem becomes more expensive with increasing  $L$  and  $N$ , the large number of thermal sweeps by MFPA causes worse performance compared to FPSA. Table 7.6 shows the error between FPSA and MFPA. For all three problems, the error between FPSA and MFPA is the same order of magnitude as the specified tolerance.

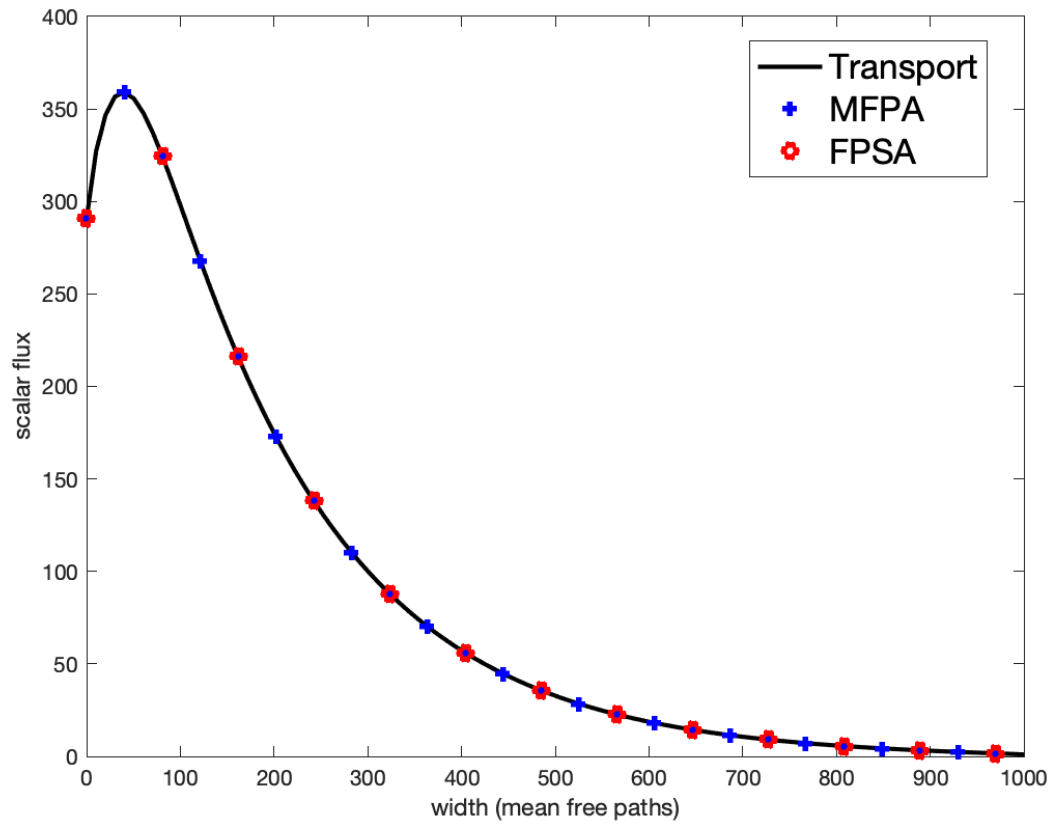


Figure 7.7: Radiative results for  $N = 16$  and  $L = 15$  using HGK with  $g = 0.99$

	$cm^{-1}$		$cm^{-1}$
$\Sigma_{s,0}$	1000	$\Sigma_{s,32}$	732.3033696543974
$\Sigma_{s,1}$	990	$\Sigma_{s,33}$	724.9803359578535
$\Sigma_{s,2}$	980.1	$\Sigma_{s,34}$	717.7305325982749
$\Sigma_{s,3}$	970.299	$\Sigma_{s,35}$	710.5532272722921
$\Sigma_{s,4}$	960.59601	$\Sigma_{s,36}$	703.4476949995692
$\Sigma_{s,5}$	950.9900498999999	$\Sigma_{s,37}$	696.4132180495734
$\Sigma_{s,6}$	941.4801494009999	$\Sigma_{s,38}$	689.4490858690779
$\Sigma_{s,7}$	932.0653479069899	$\Sigma_{s,39}$	682.5545950103869
$\Sigma_{s,8}$	922.7446944279201	$\Sigma_{s,40}$	675.729049060283
$\Sigma_{s,9}$	913.5172474836409	$\Sigma_{s,41}$	668.9717585696802
$\Sigma_{s,10}$	904.3820750088045	$\Sigma_{s,42}$	662.2820409839835
$\Sigma_{s,11}$	895.3382542587163	$\Sigma_{s,43}$	655.6592205741437
$\Sigma_{s,12}$	886.3848717161293	$\Sigma_{s,44}$	649.1026283684022
$\Sigma_{s,13}$	877.5210229989679	$\Sigma_{s,45}$	642.6116020847181
$\Sigma_{s,14}$	868.7458127689782	$\Sigma_{s,46}$	636.1854860638709
$\Sigma_{s,15}$	860.0583546412885	$\Sigma_{s,47}$	629.8236312032323
$\Sigma_{s,16}$	851.4577710948755	$\Sigma_{s,48}$	623.5253948912
$\Sigma_{s,17}$	842.9431933839268	$\Sigma_{s,49}$	617.290140942288
$\Sigma_{s,18}$	834.5137614500875	$\Sigma_{s,50}$	611.117239532865
$\Sigma_{s,19}$	826.1686238355866	$\Sigma_{s,51}$	605.0060671375363
$\Sigma_{s,20}$	817.9069375972308	$\Sigma_{s,52}$	598.9560064661609
$\Sigma_{s,21}$	809.7278682212584	$\Sigma_{s,53}$	592.9664464014994
$\Sigma_{s,22}$	801.6305895390459	$\Sigma_{s,54}$	587.0367819374844
$\Sigma_{s,23}$	793.6142836436554	$\Sigma_{s,55}$	581.1664141181095
$\Sigma_{s,24}$	785.6781408072187	$\Sigma_{s,56}$	575.3547499769285
$\Sigma_{s,25}$	777.8213593991466	$\Sigma_{s,57}$	569.6012024771592
$\Sigma_{s,26}$	770.0431458051551	$\Sigma_{s,58}$	563.9051904523875
$\Sigma_{s,27}$	762.3427143471035	$\Sigma_{s,59}$	558.2661385478636
$\Sigma_{s,28}$	754.7192872036326	$\Sigma_{s,60}$	552.6834771623851
$\Sigma_{s,29}$	747.1720943315962	$\Sigma_{s,61}$	547.1566423907612
$\Sigma_{s,30}$	739.7003733882802	$\Sigma_{s,62}$	541.6850759668536
$\Sigma_{s,31}$	732.3033696543974	$\Sigma_{s,63}$	536.268225207185

Table 7.4: Henyey-Greenstein cross-section Moments for  $g = 0.99$



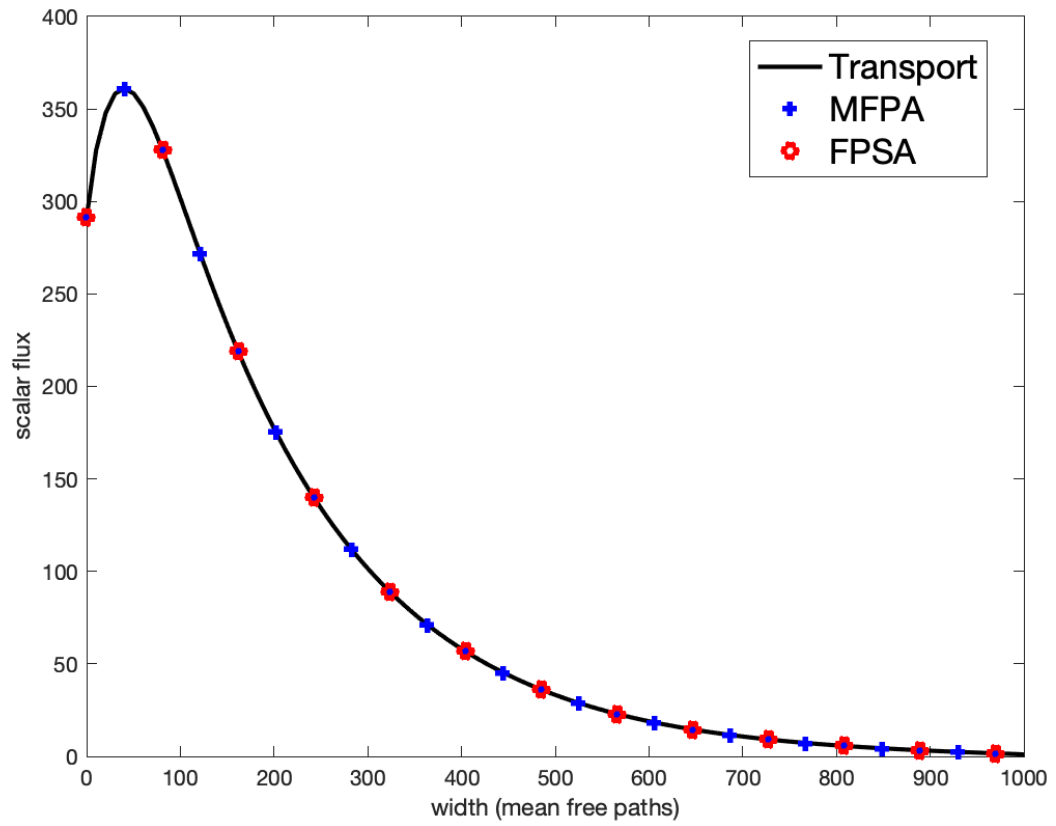


Figure 7.8: Radiative results for  $N = 32$  and  $L = 31$  using HGK with  $g = 0.99$

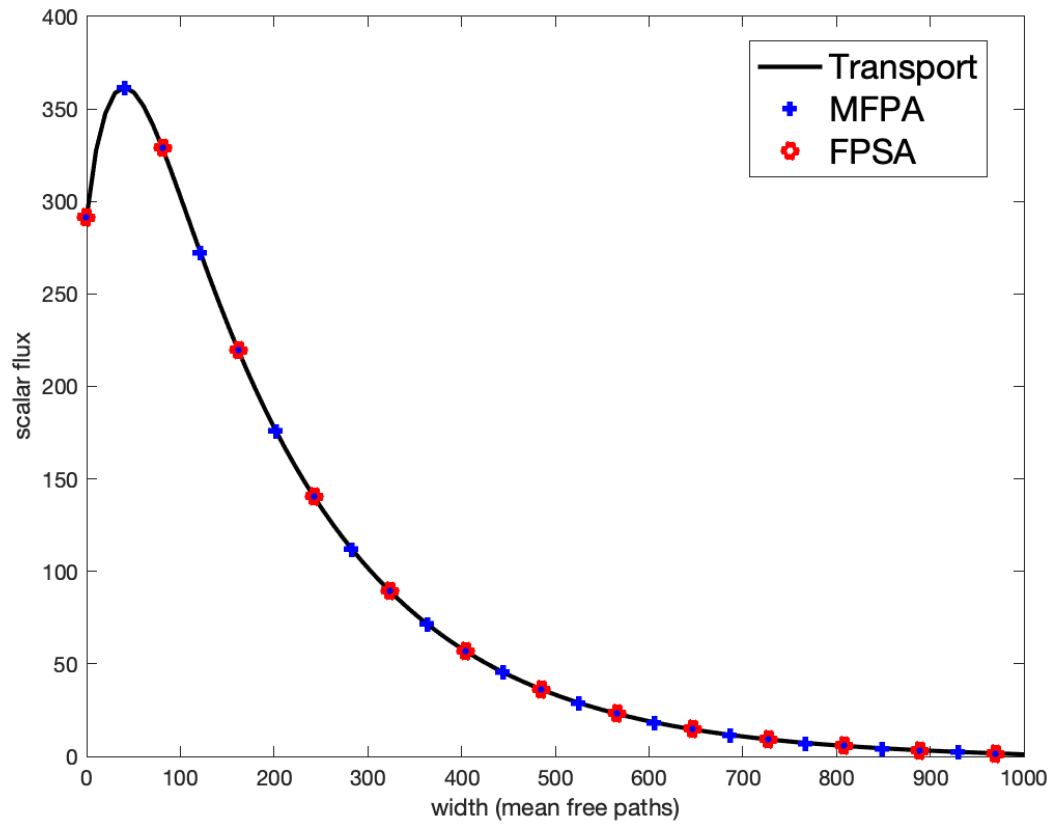


Figure 7.9: Radiative results for  $N = 64$  and  $L = 63$  using HGK with  $g = 0.99$

N/L	Method	Runtime (s)	Transport sweeps	Thermal sweeps
16/15	Transport	12.3	12285	3
	FPSA	0.828	64	3
	MFPA	0.600	51	80
32/31	Transport	44.7	11775	3
	FPSA	3.31	67	3
	MFPA	3.94	54	84
64/63	Transport	186	11272	3
	FPSA	16.5	66	3
	MFPA	27.3	55	85

Table 7.5: Runtime, Transport and Thermal Sweeps for Radiative Transfer Problem using non accelerated transport, FPSA coupling, and MFPA coupling with HGK

N/L	Error ( $\times 10^{-5}$ )
16/15	0.127
32/31	0.101
64/63	0.102

Table 7.6: Error(Eq. (7.10)) between angular flux moments found from MFPA coupling versus FPSA coupling using HGK

### 7.4.3 Screened Rutherford Kernel

The SRK approaches the FP limit as  $\eta$  approaches 0 [28, 29]. We can test the radiative transfer problem using the SRK with different  $\eta$  parameters to see how MFPA coupling

performs when  $\eta$  approaches 0. We use the three sets of scattering moments generated in Table 6.2.

For all three problems, coupling with MFPA and FPSA converge to the same solution as non accelerated transport. The results are displayed in Figs. 7.10 to 7.12. Table 7.7 shows the runtimes and transport sweeps for non accelerated transport, FPSA, and MFPA. MFPA coupling outperforms FPSA coupling in time for all three problems. As the FP limit is approached, the number of thermal sweeps in the inner loop of MFPA is reduced leading to even faster runtimes when compared to FPSA. If thermal sweeps became more complex and expensive, we could see FPSA coupling outperform MFPA coupling. The relationship of error between FPSA coupling and MFPA coupling and  $\Delta$  parameter can be seen in Table 7.8. The error is one order of magnitude than the specified tolerance.

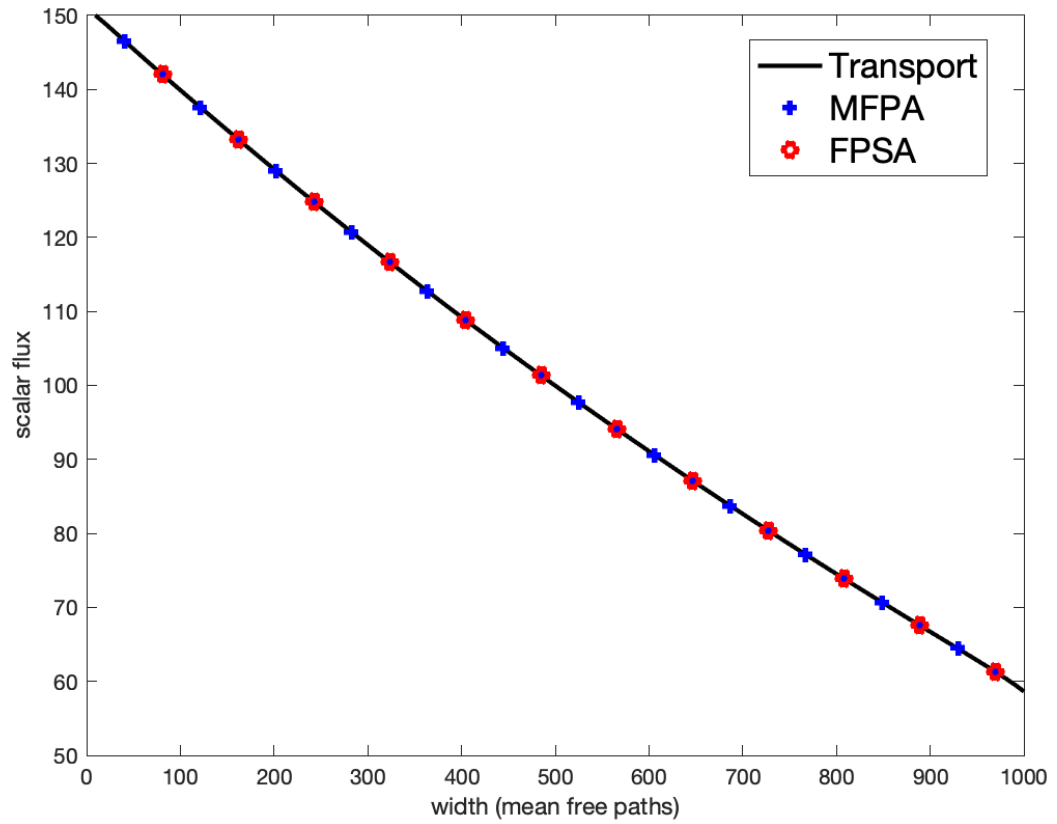


Figure 7.10: Radiative results for  $N = 16$  and  $L = 15$  using SRK with  $\eta = 10^{-5}$

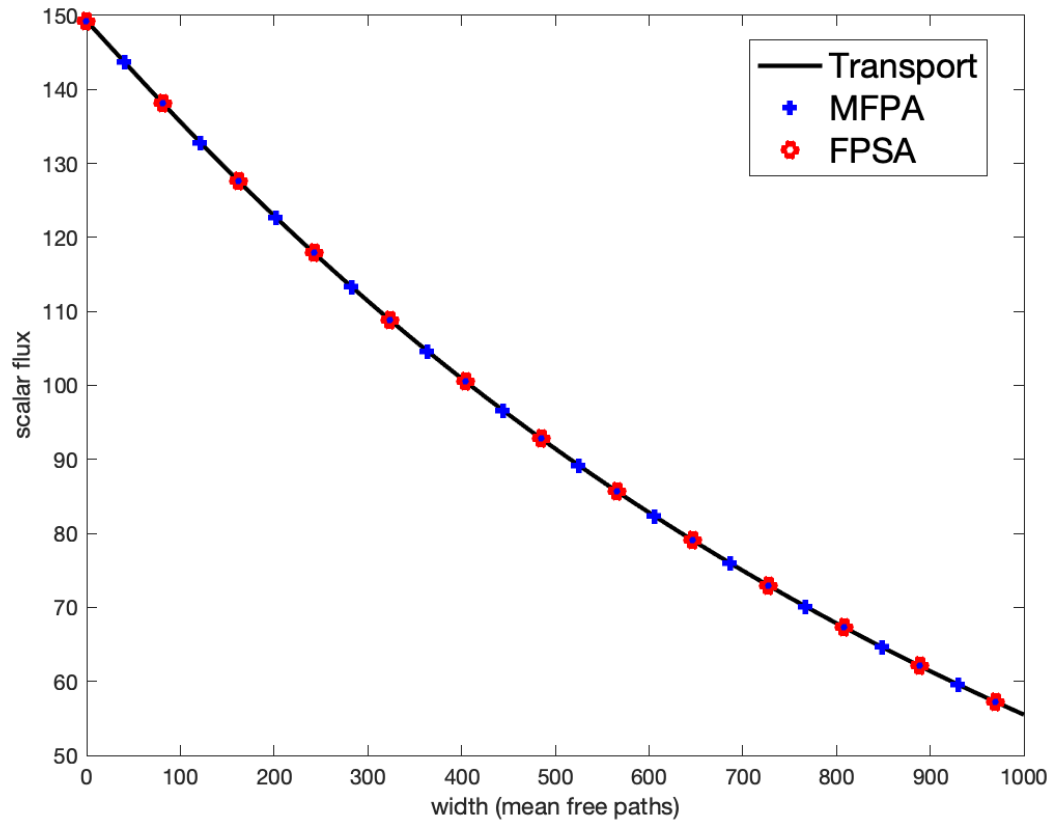


Figure 7.11: Radiative results for  $N = 16$  and  $L = 15$  using SRK with  $\eta = 10^{-6}$

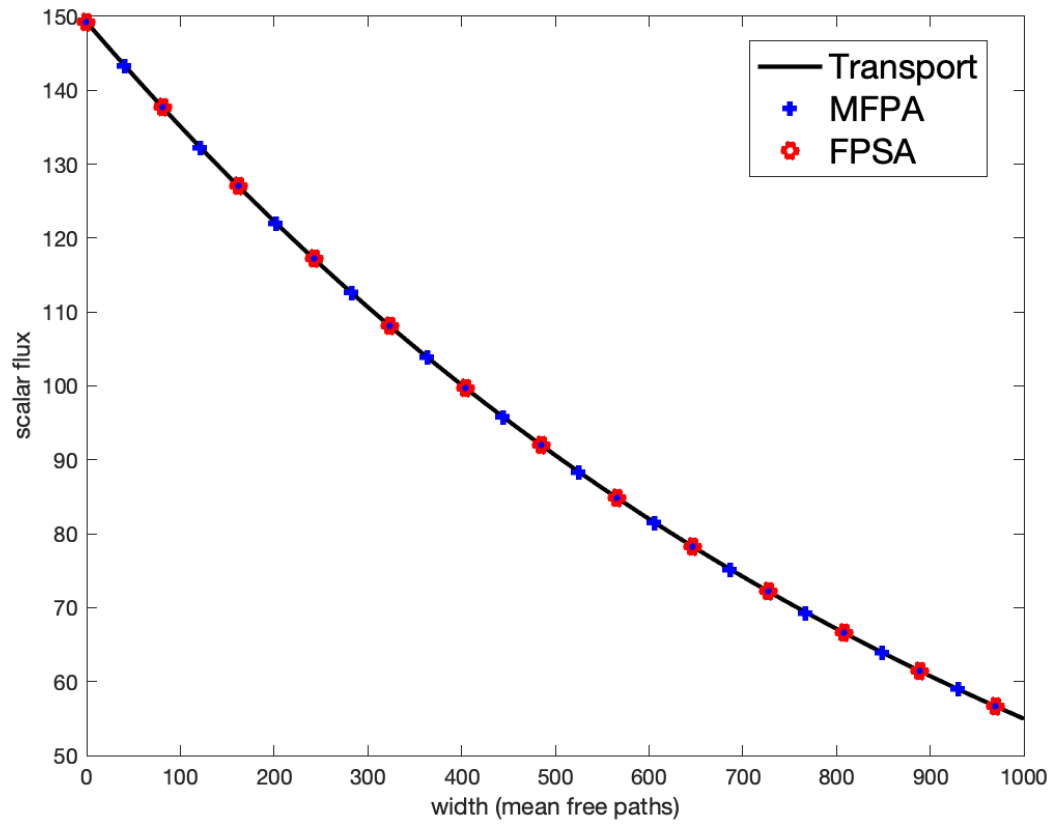


Figure 7.12: Radiative results for  $N = 16$  and  $L = 15$  using SRK with  $\eta = 10^{-7}$

$\eta$	Method	Runtime (s)	Transport sweeps	Thermal sweeps
$10^{-5}$	Transport	8.86	8702	3
	FPSA	0.359	25	3
	MFPA	0.192	17	27
$10^{-6}$	Transport	7.65	7141	3
	FPSA	0.265	19	3
	MFPA	0.139	12	18
$10^{-7}$	Transport	7.84	7168	3
	FPSA	0.168	12	3
	MFPA	0.0817	7	11

Table 7.7: Runtime, Transport and Thermal Sweeps for Radiative Transfer Problem using non accelerated transport, FPSA coupling, and MFPA coupling with SRK

$\Delta$	Error ( $\times 10^{-7}$ )
$10^{-5}$	0.588
$10^{-6}$	0.746
$10^{-7}$	0.231

Table 7.8: Error(Eq. (7.10)) between angular flux moments found from MFPA coupling versus FPSA coupling using SRK



## Chapter 8: Discussion of Future Work

We have introduced the Modified Fokker-Planck Acceleration technique for steady-state, monoenergetic transport in slab geometry. Upon convergence, the modified FP and the transport models are consistent; in other words, the (LO) modified FP equation *preserves the moments* of angular flux of the (HO) transport equation. MFPA using a linear consistency term was shown to be mathematically equivalent with FPSA, but the MFPA setup could allow for more efficient multiphysics coupling.

To validate MFPA, we performed angular-discrete Fourier analysis and compared with FPSA and unaccelerated transport. We found that the results of linear MFPA and FPSA were consistent as expected. For further validation we tested both homogeneous and heterogeneous media with an isotropic internal source with vacuum boundaries, and with no internal source and an incoming beam in the left boundary. For both sets of problems, the SRK, EK, and HGK were used. The results confirmed that MFPA using a linear consistency term and FPSA were equivalent. The runtime and iterations of MFPA and FPSA both vastly outperformed DSA and unaccelerated transport for all cases by orders of magnitude. MFPA, FPSA, and non accelerated transport using GMRES were compared to MFPA using Picard iteration. MFPA using both solvers and FPSA using GMRES notably outperformed non accelerated GMRES. Furthermore, although solver runtimes were similar for MFPA using both solvers and FPSA-GMRES, the setting up times of the preconditioners for the GMRES

approaches were relatively large 1-2 orders of magnitude greater), making them slower overall than MFPA with Picard iteration.

Moreover, MFPA has the feature of preserving the moments of angular flux of the HO equation, which offers the advantage of integrating the LO model into multiphysics models. A test radiative transfer problem was introduced. Linear MFPA coupling, FPSA coupling, and unaccelerated transport coupling were defined and tested. We found that linear MFPA coupling outperformed FPSA coupling and unaccelerated transport coupling in time for problems tested that have a valid FP limit. The amount of transport sweeps was always reduced using linear MFPA, but the amount of thermal sweeps was significantly increased when using kernels that did not have a valid FP limit. When testing the Exponential kernel, linear MFPA coupling was the superior choice because it reduced the amount of transport sweeps while slightly increasing the amount of thermal sweeps. This led to a reduction in convergence time when compared to FPSA coupling. When testing the HGK we saw that the amount of thermal sweeps done by MFPA coupling greatly increased. The HGK does not have a valid FP limit, which led to an increase in the amount of modified FP solves in the thermal loop. We saw that FPSA coupling outperformed MFPA coupling in time due to the greater amount of transport sweeps being done with MFPA. The SRK was tested using three different  $\eta$  parameters to see how MFPA performs as the FP limit is approached. We saw that MFPA coupling far outperformed FPSA coupling as  $\eta$  was closer to 0. For larger  $\eta$  values, MFPA coupling lost performance due to an increase in the amount of thermal sweeps that needed to be done.

Several remaining aspects of the MFPA method are not fully explored. Application of linear MFPA to a realistic multiphysics problem with forward-peaked, high scattering could show its true potential when compared to FPSA coupling. More testing of a variety

of problems will give more validation and understanding of MFPA multiphysics coupling. Further experimentation of MFPA coupling and FPSA coupling needs to be done to understand how the number of transport sweeps versus sweeps of other physics affects time. In this document we saw MFPA coupling outperform FPSA coupling in time for all problems, even when the total number of iterations for MFPA was greater than FPSA for some cases. Introducing test problems that have more expensive multiphysics solves could give a better understanding of the performance between FPSA and MFPA coupling. We expect to see that for realistic problems that have scattering with a valid FP limit, MFPA coupling will be the better choice compared to FPSA due to the overall reduction in iterations.

There has been difficulty developing MFPA into a true HOLO model where the LO equation is solved on a courser angular mesh. The difficulty stems from Gauss-Legendre not being a nested quadrature set. There has been recent interest in solving transport using Clenshaw-Curtis quadrature which has nested quadrature sets [83]. Future development of MFPA as a true HOLO model could take advantage of a nested quadrature set and show more advantages in multiphysics coupling when compared to FPSA.

## Bibliography

- [1] M. L. Adams and E. W. Larsen. “Fast Iterative Methods for Discrete Ordinates Particle Transport Problems”. In: *Progress in Nuclear Energy* 40.1 (2002), pp. 3–159.
- [2] Y. Saad and M. H. Schultz. “GMRES: A Generalized Minimal Residual Algorithm for Solving Nonsymmetric Linear Systems”. In: *SIAM Journal on Scientific and Statistical Computing* 7.3 (1986), pp. 856–869.
- [3] R.E. Alcouffe. “Diffusion Synthetic Acceleration Methods for the Diamond-Differenced Discrete-Ordinates Equations”. In: *Nuclear Science and Engineering* 64 (1977), pp. 344–355.
- [4] R. E. Alcouffe. “A Stable Diffusion Synthetic Acceleration Method for Neutron Transport Iterations”. In: *Transactions of the American Nuclear Society* 23 (1976), p. 203.
- [5] W. F. Miller Jr. “Generalized Rebalance: A Common Framework for Transport Acceleration Methods”. In: *Nuclear Science and Engineering* 65.2 (1978), pp. 226–236.
- [6] J. E. Morel. “A Synthetic Acceleration Method for Discrete Ordinates Calculations with Highly Anisotropic Scattering”. In: *Nuclear Science and Engineering* 82.1 (1982), pp. 34–46.
- [7] E.W. Larsen. “Unconditionally Stable Diffusion-Synthetic Acceleration Methods for the Slab Geometry Discrete Ordinates Equations. Part I: Theory”. In: *Nuclear Science and Engineering* 82 (1982), pp. 47–63.
- [8] D. R. McCoy and E.W. Larsen. “Unconditionally Stable Diffusion-Synthetic Acceleration Methods for the Slab Geometry Discrete Ordinates Equations. Part II: Numerical Results”. In: *Nuclear Science and Engineering* 82 (1982), p. 64.
- [9] M.L. Adams and W. R. Martin. “Diffusion Synthetic Acceleration of Discontinuous Finite Element Transport Iterations”. In: *Nuclear Science and Engineering* 111.2 (1992), pp. 145–167.
- [10] B. Turcksin, J. C. Ragusa, and J. E. Morel. “Angular Multigrid Preconditioner for Krylov-Based Solution Techniques Applied to the  $S_n$  Equations with Highly Forward-Peaked Scattering”. In: *Transport Theory and Statistical Physics* 41 (2012), pp. 1–22.

- [11] E. N. Aristova and V. Ya. Gol'din. "Computation of Anisotropy Scattering of Solar Radiation in Atmosphere (monoenergetic case)". In: *Journal of Quantitative Spectroscopy and Radiative Transfer* 67.2 (2000), pp. 139–157.
- [12] J.E. Morel, E.W. Larsen, and M.K. Matzen. "A synthetic acceleration scheme for radiative diffusion calculations". In: *Journal of Quantitative Spectroscopy and Radiative Transfer* 34.3 (1985), pp. 243–261.
- [13] K. S. Smith. "Nodal method storage reduction by nonlinear iteration". In: *Transactions of the American Nuclear Society* 44 (1983), pp. 265–266.
- [14] A. Zhu, M. Jarrett, Y. Xu, B. Kochunas, E. Larsen, and T. Downar. "An optimally diffusive Coarse Mesh Finite Difference method to accelerate neutron transport calculations". In: *Annals of Nuclear Energy* 95 (2016), pp. 116–124.
- [15] S. Shaner, B. Forget, and K. Smith. "Sensitivity analysis and performance of the Adiabatic, Theta, and Multigrid Amplitude Function kinetics methods in 2D MOC neutron transport". In: 2015.
- [16] A. Zhu, Y. Xu, A. Graham, M. Young, T. Downar, and L. Cao. "Transient methods for pin-resolved whole core transport using the 2D-1D methodology in MPACT". In: 2015.
- [17] J. Cho, K. Kim, C. Lee, H. Joo, Won-Sik Yang, T. Taiwo, and J. Thomas. "Transient capability for a MOC-based whole core transport code DeCART". In: *Transactions of the American Nuclear Society* 92 (2005), pp. 721–722.
- [18] Y. Wang. "Nonlinear diffusion acceleration for the multigroup transport equation discretized with  $S_N$  and continuous FEM with rattlesnake". In: 2013.
- [19] L. R. Cornejo and D. Y. Anistratov. "Nonlinear Diffusion Acceleration Method with Multigrid in Energy for k-Eigenvalue Neutron Transport Problems". In: *Nuclear Science and Engineering* 184.4 (2016), pp. 514–526.
- [20] S. Xiao, K. Ren, and D. Wang. "A Local Adaptive Coarse-Mesh Nonlinear Diffusion Acceleration Scheme for Neutron Transport Calculations". In: *Nuclear Science and Engineering* 189.3 (2018), pp. 272–281.
- [21] S. Schunert, Y. Wang, F. Gleicher, J. Ortensi, B. Baker, V. Laboure, C. Wang, M. DeHart, and R. Martineau. "A flexible nonlinear diffusion acceleration method for the  $S_N$  transport equations discretized with discontinuous finite elements". In: *Journal of Computational Physics* 338 (2017), pp. 107–136.
- [22] D. A. Knoll, H. Park, and K. Smith. "Application of the Jacobian-Free Newton-Krylov Method to Nonlinear Acceleration of Transport Source Iteration in Slab Geometry". In: *Nuclear Science and Engineering* 167.2 (2011), pp. 122–132.
- [23] H. Park, D. A. Knoll, and C. K. Newman. "Nonlinear Acceleration of Transport Criticality Problems". In: *Nuclear Science and Engineering* 172 (2012), pp. 52–65. DOI: 10.13182/NSE11-81.

- [24] B. R. Herman, B. Forget, and K. Smith. “Progress toward Monte Carlo–thermal hydraulic coupling using low-order nonlinear diffusion acceleration methods”. In: *Annals of Nuclear Energy* 84 (2015), pp. 63–72.
- [25] B.R.Herman. “Monte Carlo and Thermal Hydraulic Coupling using Low-Order Nonlinear Diffusion Acceleration”. PhD thesis. Cambridge, MA: Massachusetts Institute of Technology, 2014.
- [26] K. M. Khattab and E. W. Larsen. “Synthetic Acceleration Methods for Linear Transport Problems with Highly Anisotropic Scattering”. In: *Nuclear Science and Engineering* 107.3 (1991), pp. 217–227.
- [27] Y. Zhang, J. Ragusa, and J. E. Morel. “Iterative performance of various formulations of the  $SP_N$  equations”. In: *Journal of Computational Physics* 252 (2013), pp. 558–572.
- [28] J K. Patel, J S. Warsa, and A K. Prinja. “Accelerating the solution of the  $S_N$  equations with highly anisotropic scattering using the Fokker-Planck approximation”. In: *Annals of Nuclear Energy* 147 (2020).
- [29] J. K. Patel. “Fokker-Planck-Based Acceleration for  $S_N$  Equations with Highly Forward-Peaked Scattering in Slab Geometry”. PhD thesis. Albuquerque, NM: The University of New Mexico, 2016.
- [30] D. Keyes, L. McInnes, C. Woodward, W. Gropp, E. Myra, M. Pernice, J. Bell, J. Brown, A. Clo, J. Connors, E. Constantinescu, D. Estep, K. Evans, C. Farhat, A. Hakim, G. Hammond, G. Hansen, J. Hill, T. Isaac, and B. Wohlmuth. “Multiphysics Simulations: Challenges and Opportunities”. In: *International Journal of High Performance Computing Applications* 27 (2013). DOI: 10.1177/1094342012468181.
- [31] L. Chacón, G. Chen, D.A. Knoll, C. Newman, H. Park, W. Taitano, J.A. Willert, and G. Womeldorff. “Multiscale high-order/low-order (HOLO) algorithms and applications”. In: *Journal of Computational Physics* 330 (2017), pp. 21–45. ISSN: 0021-9991. DOI: <https://doi.org/10.1016/j.jcp.2016.10.069>.
- [32] D Ropp and J. Shadid. “Stability of operator splitting methods for systems with indefinite operators: Reaction-diffusion systems”. In: *Journal of Computational Physics* 203 (2009), pp. 449–466.
- [33] J. K. Patel, R. Vasques, and B. D. Ganapol. “Towards a Multiphysics Model for Tumor Response to Combined-Hyperthermia-Radiotherapy Treatment”. In: *Proceedings of International Conference on Mathematics & Computational Methods Applied to Nuclear Science & Engineering*. Portland, OR, Aug. 25-29, 2019.
- [34] P. Leider. “Principles and Practice of Radiation Oncology”. In: *JNCI: Journal of the National Cancer Institute* 90.19 (1998).
- [35] D. Heifetz, D. Post, M. Petracic, J. Weisheit, and G. Bateman. “A Monte-Carlo model of neutral-particle transport in diverted plasmas”. In: *Journal of Computational Physics* 46.2 (1982), pp. 309–327.

- [36] M. D. Kilgore, H.M. Wu, and D.B. Graves. “Neutral transport in high plasma-density reactors”. In: *Journal of Vacuum Science & Technology B: Microelectronics and Nanometer Structures Processing, Measurement, and Phenomena* 12.1 (1994), pp. 494–506.
- [37] D.P. Stotler, B. LaBombard, J.L. Terry, and S.J. Zweben. “Neutral transport simulations of gas puff imaging experiments”. In: *Journal of Nuclear Materials* 313-316 (2003), pp. 1066–1070.
- [38] M. I. Budyko. “The Heat Balance of the Earth’s Surface”. In: *Soviet Geography* 2.4 (1961), pp. 3–13.
- [39] J. E. Hansen and L. D. Travis. “Light scattering in planetary atmospheres”. In: *Space Science Reviews* 16.4 (1974), pp. 527–610.
- [40] L. C. Henyey and J. L. Greenstein. “Diffuse Radiation in the Galaxy”. In: *The Astrophysics Journal* 93 (1941), pp. 70–83.
- [41] H. Park, D.A. Knoll, R.M. Rauenzahn, C.K. Newman, J.D. Densmore, and A.B. Wol-laber. “An Efficient and Time Accurate, Moment-Based Scale-Bridging Algorithm for Thermal Radiative Transfer Problems”. In: *SIAM Journal on Scientific Computing* 35 (2013). DOI: 10.1137/120881075.
- [42] L. Boltzmann. “Weitere Studien über Wärmegleichgewicht unter Gasmolekülen”. In: *Wiener Berichte* 66 (1872), pp. 275–370.
- [43] K.M. Case and P.F. Zweifel. *Linear Transport Theory*. Massachusetts: Addison-Wesley, 1967.
- [44] J.J. Duderstadt and W.R. Martin. *Transport Theory*. New York: Wiley-Interscience, 1979.
- [45] G.C. Pomraning. *Linear Kinetic Theory and Particle Transport in Stochastic Mixtures*. Singapore: World Scientific Press, 1991.
- [46] G. L. Olson, L. H. Auer, and M. L. Hall. “Diffusion,  $P_1$ , and other approximate forms of radiation transport”. In: *Journal of Quantitative Spectroscopy and Radiative Transfer* 64.6 (2000), pp. 619–634.
- [47] M. F. Modest. *Radiative Heat Transfer*. Netherlands: Elsevier Inc., 2013.
- [48] J.J. Kuczek, J.K. Patel, and R. Vasques. “Modified Fokker-Planck Acceleration for Forward-Peaked Transport Problems in Slab Geometry”. In: *Journal of Computational and Theoretical Transport* 50.5 (2021), pp. 430–453. DOI: 10.1080/23324309.2021.1894174.
- [49] R. G. McClarren. “Theoretical Aspects of the Simplified  $P_n$  Equations”. In: *Transport Theory and Statistical Physics* 39.2-4 (2010), pp. 73–109.
- [50] E.W. Larsen and J.B. Keller. “Asymptotic Solution of Neutron Transport Problems for Small Mean Free Paths”. In: *J. Math. Phys.* 15 (1974), p. 75.
- [51] E. Larsen. *Transport Theory Notes*. 2017.

- [52] L. A. Hageman and D. Young. *Applied Iterative Methods*. New York: Academic Press, Inc, 2004.
- [53] C. T. Kelley. *Iterative Methods for Linear and Nonlinear Equations*. Philadelphia: SIAM, 1995.
- [54] P. Wynn. “Acceleration Techniques in Numerical Analysis, with Particular Reference to Problems in One Independent Variable”. In: *Proc. IFIPS* (1962), pp. 149–156.
- [55] D. A. Dixon. “A Computationally Efficient Moment-Preserving Monte Carlo Electron Transport Method with Implementation in GEANT4”. PhD thesis. Albuquerque, NM: The University of New Mexico, 2015.
- [56] J. S. Warsa, T. A. Wareing, and J. E. Morel. “Krylov Iterative Methods and the Degraded Effectiveness of Diffusion Synthetic Acceleration for Multidimensional  $S_N$  Calculations in Problems with Material Discontinuities”. In: *Nuclear Science and Engineering* (2017), pp. 218–248.
- [57] W. Kofink. “Studies of the Spherical Harmonics Method in Neutron Transport Theory”. In: *Il Nuovo Ciment* 9 (1958), pp. 497–541.
- [58] E.M. Gelbard. “Applications of Spherical Harmonics Method to Reactor Problems”. In: *Technical Report WAPD-BT-20, Bettis Atomic Power Laboratory* (1960).
- [59] E.M. Gelbard. “Simplified Spherical Harmonics Equations and Their Use in Shielding Problems”. In: *Technical Report WAPD-T-1182, Bettis Atomic Power Laboratory* (1961).
- [60] E.M. Gelbard. “Applications of Simplified Spherical Harmonics Equations in Spherical Geometry”. In: *Technical Report WAPD-TM-294, Bettis Atomic Power Laboratory* (1962).
- [61] B D Ganapol. *A New 1D-Multigroup-Discrete Ordinates Algorithm for Neutron Transport*. 2005.
- [62] B.J. Matkowsky. “On the Diffusion Approximation to Transport Theory”. In: (1970).
- [63] E.W. Larsen and J.B. Keller. “Diffusion Theory as an Asymptotic Limit of Transport Theory for Nearly Critical Systems with Small Mean Free Paths”. In: *Ann. Nucl. Energy* 7 (1980), p. 249.
- [64] J.J. Duderstadt and L.J. Hamilton. *Nuclear Reactor Analysis*. New York: John Wiley & Sons, 1976.
- [65] E. E. Lewis and W. F. Miller, Jr. “Computational Methods of Neutron Transport”. In: *American Nuclear Society* (1993).
- [66] B. Shizgal. “Spectral Methods in Chemistry and Physics”. In: (2015).
- [67] M. Abramowitz and E. Stegun. *Handbook of Mathematical Functions, With Formulas, Graphs, and Mathematical Tables*, USA: Dover Publications, Inc., 1974.
- [68] H. J. Kopp. “Synthetic Method Solution of the Transport Equation”. In: *Nuclear Science and Engineering* 17 (1963), pp. 65–74.



- [69] B.J. Matkowsky. “The Approximate Arithmetical Solution by Finite Differences of Physical Problems Involving Differential Equations, with an Application to the Stresses in a Masonry Dam”. In: *Philosophical Transactions of the Royal Society* (1910).
- [70] E. Schmidt. “Auflösung der allgemeiner linearen integralgleichung”. In: *Math Ann* 64.161 (1907).
- [71] F. Zhao, X. Cui, and G. Yuan. “Iterative acceleration methods with second-order time accuracy for nonlinear diffusion equations”. In: *Advances in Computational Mathematics* 46 (2020). DOI: 10.1007/s10444-020-09756-4.
- [72] C. T. Kelley. *Solving Nonlinear Equations with Newton’s Method*. North Carolina: SIAM, 2003.
- [73] B. W. Patton and J. P. Holloway. “Application of preconditioned GMRES to the numerical solution of the neutron transport equation”. In: *Annals of Nuclear Engineering* 29 (2002), pp. 109–136.
- [74] J. S. Warsa and A. K. Prinja. “A Moment Preserving  $S_N$  Discretization for the One-Dimensional Fokker-Planck Equation”. In: *Transactions of the American Nuclear Society* 106 (2012), pp. 362–365.
- [75] W. R. Martin. “The Application of the Finite Element Method to the Neutron Transport Equation”. PhD thesis. Ann Arbor, MI: The University of Michigan, 1976.
- [76] J.E. Morel, T.A. Wareing, and K. Smith. “A Linear-Discontinuous Spatial Differencing Scheme for  $S_n$  Radiative Transfer Calculations”. In: *Journal of Computational Physics* 128.2 (1996), pp. 445–462. ISSN: 0021-9991. DOI: <https://doi.org/10.1006/jcph.1996.0223>.
- [77] MATLAB. *version 9.3.0.713579 (R2017b)*. Natick, Massachusetts: The MathWorks Inc., 2017.
- [78] E. Rutherford. “The Scattering of  $\alpha$  and  $\beta$  Rays by Matter and the Structure of the Atom”. In: *Philosophical Magazine* 6 (1911), p. 21.
- [79] G. C. Pomraning. “The Fokker-Planck Operator as an Asymptotic Limit”. In: *Mathematical Models and Methods in Applied Sciences* 2.1 (1992), pp. 21–36.
- [80] E. Rutherford. “On the Solution of a Nonlocal Transport Equation by the WeinerHopf Method”. In: *Annals of Nuclear Energy* 23 (1996), pp. 429–440.
- [81] G. C. Pomraning, A. K. Prinja, and J. W. VanDenburg. “An Asymptotic Model for the Spreading of a Collimated Beam”. In: *Nuclear Science and Engineering* 112.4 (1992), pp. 347–360.
- [82] G. C. Pomraning. “The Screened Rutherford Pencil Beam Problem with Heterogeneities”. In: *Nuclear Science and Engineering* 136:1 (2000), pp. 1–14.
- [83] L. N. Trefethen. “Is Gauss Quadrature Better than Clenshaw-Curtis?” In: *SIAM Review* 50.1 (2008), pp. 67–87.